1978

Blade-surface boundary layer and wake computational models for estimation of axial-flow compressor and fan blade-row fluid turning angles and losses

Elmer Carl Hansen
Iowa State University

7813230

HANSEN, ELMER CARL
BLADE-SURFACE BOUNDARY LAYER AND WAKE COMPUTATIONAL MODELS FOR ESTIMATION OF AXIAL-FLOW COMPRESSOR AND FAN BLADE-ROW FLUID TURNING ANGLES AND LOSSES.

IOWA STATE UNIVERSITY, PH.D., 1978

Blade-surface boundary layer and wake computational models for estimation of axial-flow compressor and fan blade-row fluid turning angles and losses

by

Elmer Carl Hansen

A Dissertation Submitted to the
Graduate Faculty in Partial Fulfillment of
The Requirements for the Degree of
DOCTOR OF PHILOSOPHY

Major: Mechanical Engineering

Approved:

Signature was redacted for privacy.

In Charge of Major Work

Signature was redacted for privacy.

For the Major Department

Signature was redacted for privacy.

For the Graduate College

Iowa State University
Ames, Iowa

1978

TABLE OF CONTENTS

DEDICATION

This work is dedicated to the one who made it possible, the Lord of lords and the King of kings, Jesus Christ.

LIST OF SYMBOLS

a	velocity gradient
$a_1, a_2, a_3, a_4, \alpha$	coefficients
b	stream sheet thickness
c	chord length
C_d	coefficient of drag, as in Herrig et al. (1957)
C_p	pressure coefficient, $\frac{p_i - p}{p_i^o - p_i}$
c_p	molar specific heat at constant pressure
C_w	loss coefficient, as in Herrig et al. (1957)
f	stream function for the boundary layer solution
h	enthalpy
H	form factor, $\frac{\delta^*}{\theta}$
k	isentropic constant or thermal conductivity
ℓ_1, ℓ_2	lengths within the laminar separation bubble
m	meridional distance
M	mach number
p	pressure
r	radius
Re_c, Re_θ	Reynolds number based on chord, based on momentum thickness
s	length along the surface and along the streamline from the trailing edge
t	blade spacing in the tangential direction
T	temperature
Tu	turbulence intensity
TF	turbulence factor

U	velocity
$\overline{U}_{e_r}$	reattachment velocity ratio, U_r/U_{sep}
u,v	velocities in the x and y directions respectively
$\overline{u'v'\rho}$	Reynolds stress
$\overline{v'h'\rho}$	Reynolds heat flux
w	weight flow through the passage
X	length along the chord line
x,y	cartesian coordinates
α	angle of attack, angle between inlet-flow direction and blade chord, or inclination of the streamsheet from the meridional direction, Equation 9
β	flow angle with respect to the meridional direction
$\Delta\beta$	turning between the upstream and downstream boundaries
γ	stagger angle
δ	boundary layer thickness
δ^*	boundary layer displacement thickness
δ_{te}	blade trailing edge thickness
Δ	difference
η	normal to the streamlines
θ	boundary layer momentum thickness or circumferential coordinate
κ	curvature of a streamline
μ	absolute viscosity
ν	kinematic viscosity
ρ	density
σ	solidity, $\frac{c}{t}$

τ	shear stress
ψ	stream function
ω	wheel speed

Subscripts

ave	average
c	centerline of the wake
calc	calculated
ds	downstream
e	edge
eff	effective
i	inlet
I	inviscid
inj	injected
o	outlet
p	pressure surface
r	reattachment
s	suction surface
sep	separation
t	turbulent
te	trailing edge
tr	transition
v	viscous
w	wall value

Superscripts

o	total state
$\overline{\quad}$	time mean, except $\overline{U}_{e_r}$
'	turbulent fluctuation

INTRODUCTION

Current design and performance prediction systems for axial-flow fans and compressors compute fluid velocity distributions upstream, inside and downstream of each blade row. These velocity distributions are obtained using estimated values of loss in total pressure and turning of the fluid for each blade profile and cascade arrangement. In the past and at present loss and turning information have been largely based on accumulated empirical information from experimental research and on data correlations from such research.

Attempts are being made to develop full flow field computational systems which predict the loss and turning for arbitrary blade profiles in cascades with given inlet flow conditions. Such systems, in addition to providing loss and turning information for design and performance prediction system, are also useful for other purposes. When advanced blade profile shapes for high performance turbomachines are under development, full flow field calculations provide an opportunity to locate the problem areas which produce poor performance. Also, insight can be gained into trends in the fluid mechanics of the flow. This insight can then help in the formulation and improvement of correlations which had previously been based on experimental data alone.

Flow through an axial-flow turbomachine has frequently been thought of in terms of flow along S_1, blade-to-blade surfaces and S_2, hub-to-tip surfaces, Figure 1. The assumption of S_1 and S_2 surfaces is not completely correct physically, but is one way to generate a solution

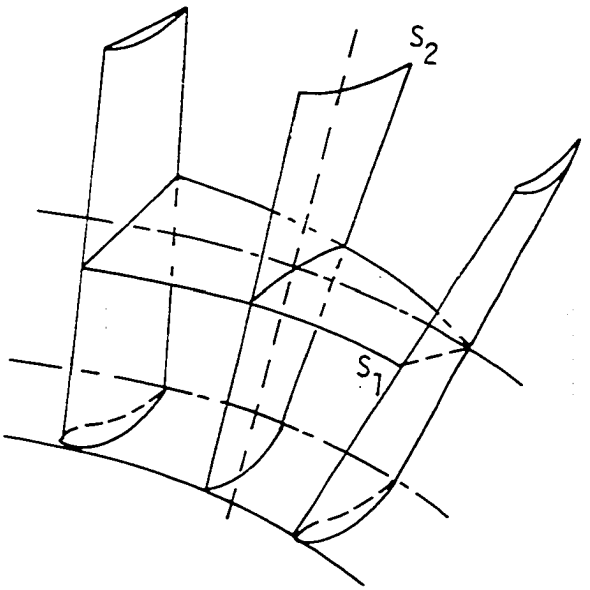

Figure 1. The S_1 and S_2 surface.

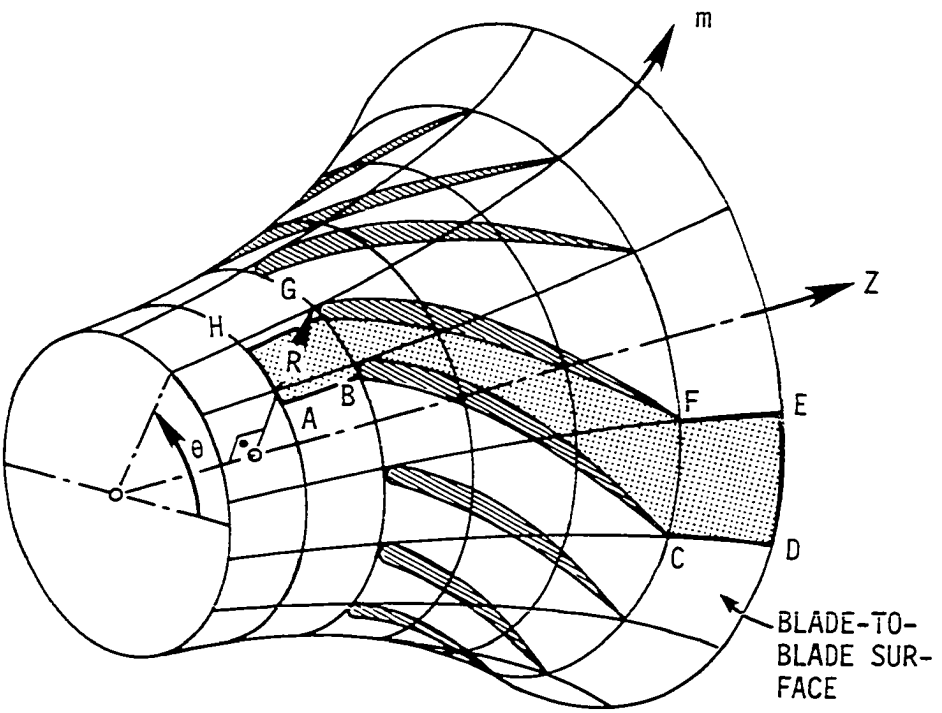

Figure 2. An axially symmetric S_1 surface.

using the present state of the art in computation. It is hoped that in the future fully three-dimensional viscous models will be developed. In the meantime, progress can be made by calculating and understanding the flow field on each of the two types of calculation surfaces. The work to be presented in this dissertation deals only with the flow on an axially symmetric blade-to-blade surface as shown in Figure 2, where there can be a density change, an axial velocity-density product change and a radius change from cascade inlet to outlet. The object of the work reported was to develop a method for computation of the flow field around an arbitrary blade cascade on an axially symmetric blade-to-blade surface, which takes into account the blade surface boundary layers, separation of those boundary layers, and mixing in the wake. The method predicts the overall turning and loss in the context of an inviscid-viscous interaction scheme.

A REVIEW OF VISCOUS CASCADE MODELING

Rationale for Inviscid-Viscous Flow Interaction

The idea of dividing a flow problem into two separate regions, each having its own set of equations which are solved independently and matched at some common boundary, is not new. Prandtl suggested this type of approach by pointing out that in high Reynolds number flow around a body there is a thin viscous "boundary layer" region next to the body and a basically "inviscid flow" around that. The inviscid region is then dominated by pressure and inertial forces while in the viscous region pressure, inertial and viscous forces all play an important role. This simplification made the calculation of flow around an isolated airfoil or an airfoil cascade possible, though the answer could only be approximate. However, as computational facilities have become much larger and faster, the question has arisen as to whether the boundary layer simplification is necessary. Without the use of the boundary layer simplification, a fully viscous solution might be obtained in which the complete set of equations for viscous flow would be solved over the entire flow region.

The advantage of a fully viscous calculation is that if it were done correctly it should give a solution which matches the real flow. The disadvantages of this type of solution, which have greatly hindered its use, are that for high Reynolds number flow, the grid structure for a finite-difference solution is very complex and a large amount of computer time is necessary, as shown by Briley (1974), and that in laminar-

transitional-turbulent flows the distribution of Reynolds stresses may be difficult to model.

On the other hand an inviscid-viscous model has the advantage of being relatively simple, by allowing the use of already existing boundary layer calculation methods and inviscid flow calculation methods. The disadvantages in using the inviscid-viscous model will most likely determine the further usefulness of the inviscid-viscous approach. These are that it is sometimes difficult to match the viscous and inviscid solutions, especially when separation occurs, and that the pressure distribution may not match the real flow when only the displacement effect of the boundary layer on the inviscid flow is modeled.

In this study it was decided to make a careful evaluation of the potential of inviscid-viscous airfoil cascade calculations by selecting current and reliable components for the inviscid and viscous calculations and concentrating on the development of an efficient and physically realistic interaction between the inviscid and viscous computation regions. In the following sections inviscid and viscous calculation methods are discussed to provide a background for the review of previously used inviscid-viscous interaction schemes for isolated airfoils and cascades.

Inviscid Flow Models

The equations of inviscid flow in two dimensions are as follows.

$$u \frac{\partial u}{\partial x} + v \frac{\partial u}{\partial y} = - \frac{1}{\rho} \frac{\partial p}{\partial x} \tag{1}$$

$$u \frac{\partial v}{\partial x} + v \frac{\partial v}{\partial y} = - \frac{1}{\rho} \frac{\partial p}{\partial y} \tag{2}$$

If the inlet flow to a cascade is uniform, and thus irrotational, and the flow is inviscid, Kelvin's theorem states that the flow is everywhere irrotational ($\frac{\partial v}{\partial x} - \frac{\partial u}{\partial y} = 0$).

The condition of irrotationality can be used in place of Equation 1 and 2 as follows. If Equation 1 is operated on by $- \frac{\partial}{\partial y}$ and 2 by $\frac{\partial}{\partial x}$, and both equations are added together, p is eliminated, and Equation 3 is obtained.

$$\frac{\partial u}{\partial x}(\frac{\partial v}{\partial x} - \frac{\partial u}{\partial y}) + u \frac{\partial}{\partial x}(\frac{\partial v}{\partial x} - \frac{\partial u}{\partial y}) + \frac{\partial v}{\partial y}(\frac{\partial v}{\partial x} - \frac{\partial u}{\partial y}) + v \frac{\partial}{\partial y}(\frac{\partial v}{\partial x} - \frac{\partial u}{\partial y}) = 0 \tag{3}$$

Because the relation, $\frac{\partial v}{\partial x} - \frac{\partial u}{\partial y} = 0$, satisfies Equation 3, it also satisfies Equations 1 and 2, $\frac{\partial v}{\partial x} - \frac{\partial u}{\partial y} = 0$ can be used in place of equations 1 and 2. This equation with the continuity equation and the appropriate boundary conditions are used to obtain an inviscid solution.

Methods of solution of the inviscid equations for cascade flow, however, have differed through history, as shown in Figure 3. This figure shows the historical development of each of four methods of

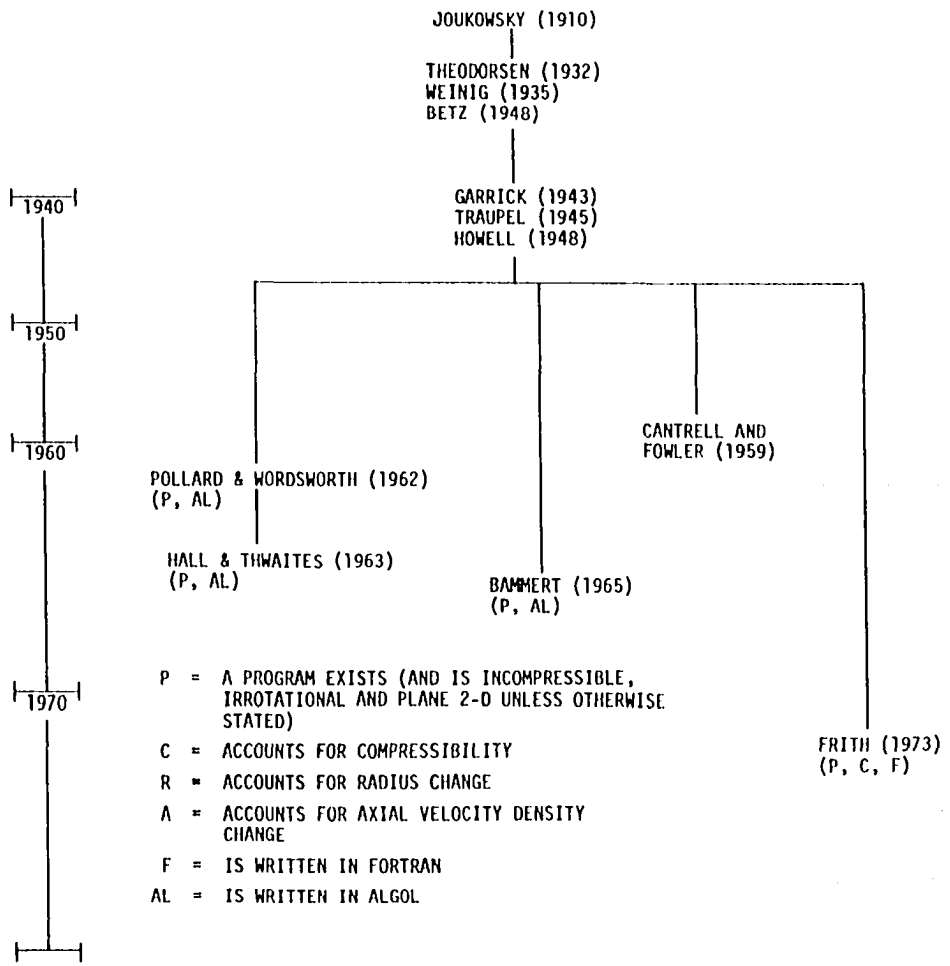

Figure 3a. History of the conformal mapping method

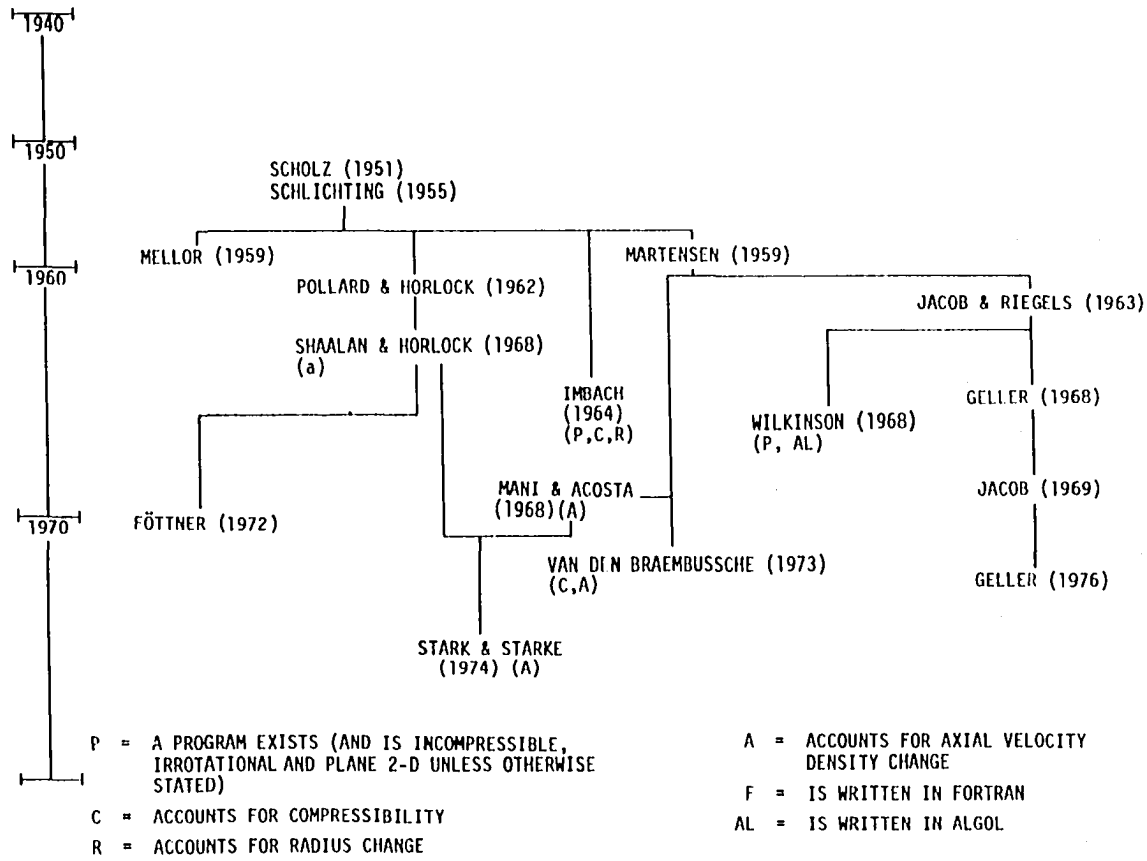

Figure 3b. History of the singularity method

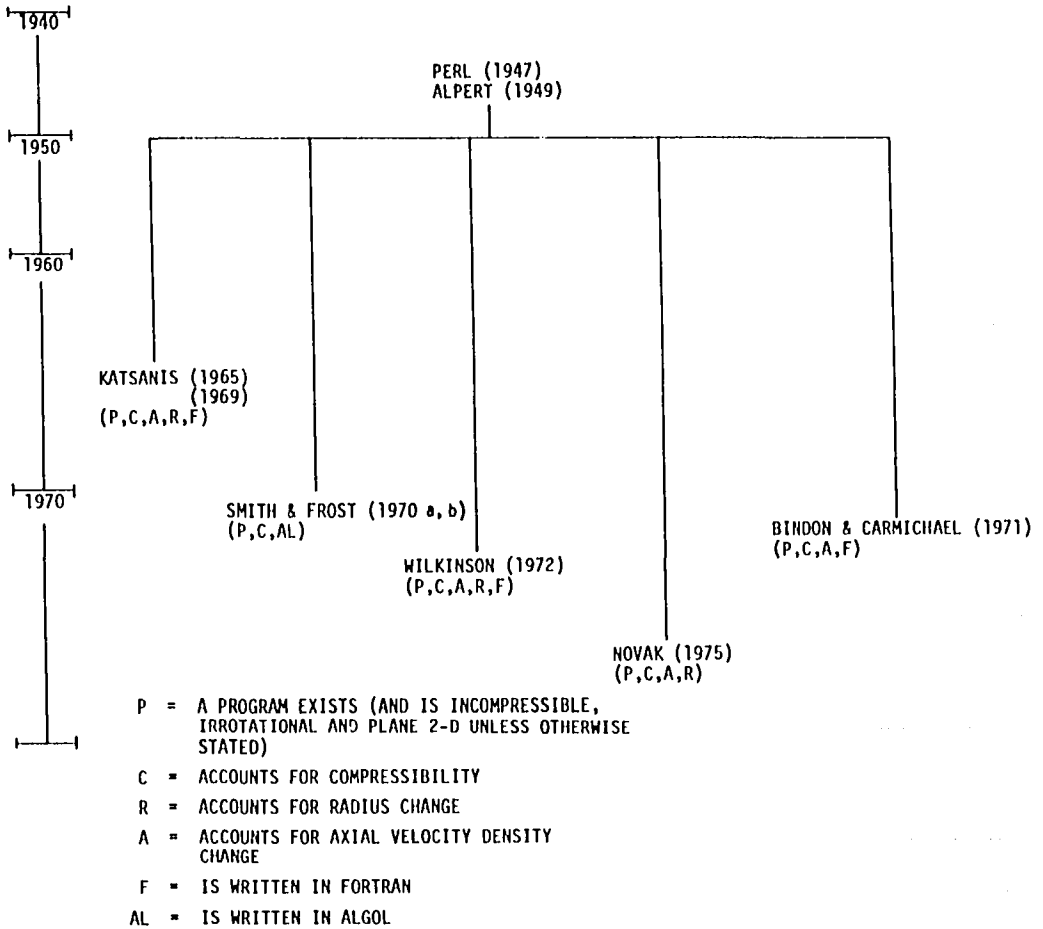

Figure 3c. History of the streamline curvature method

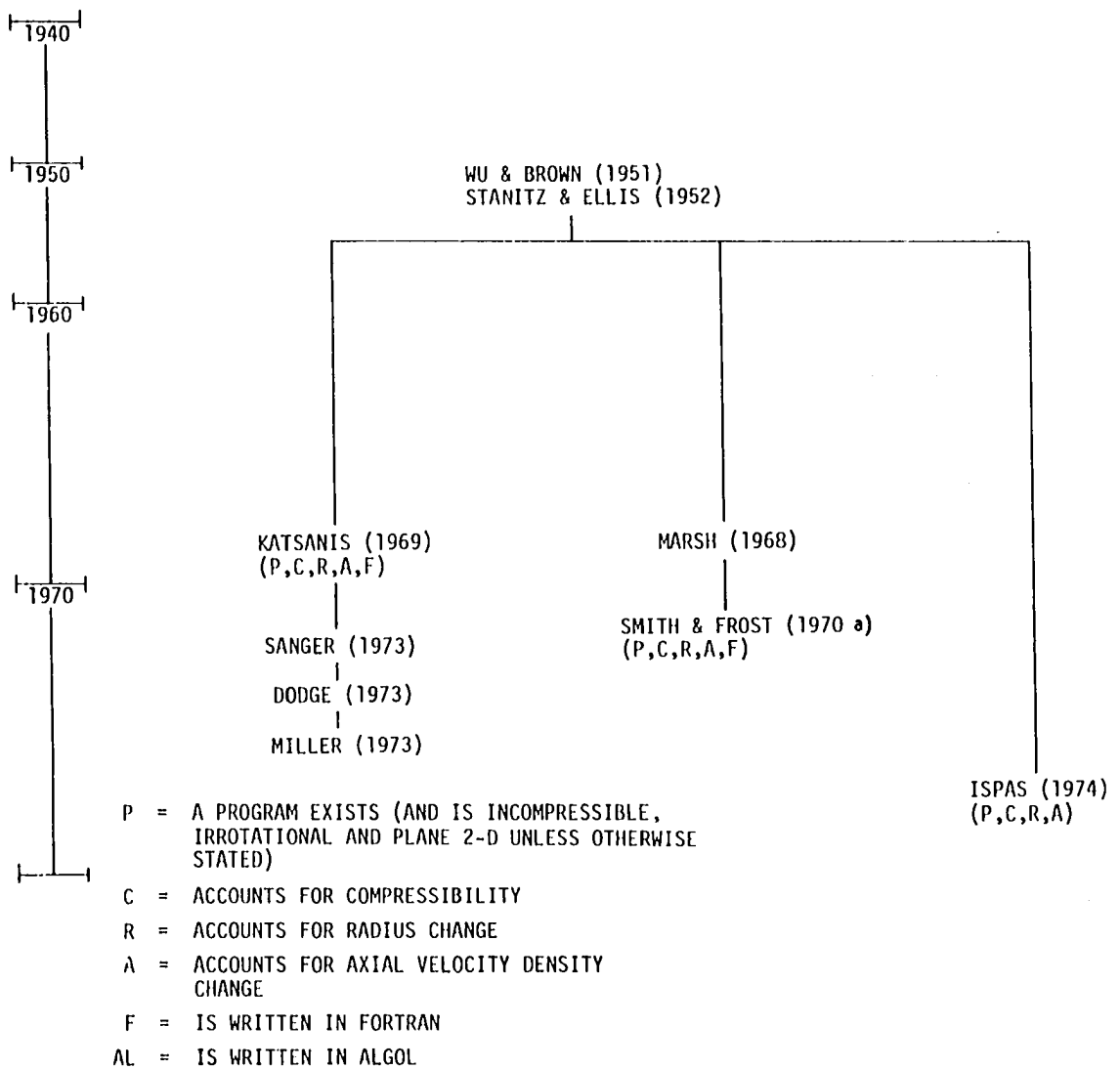

Figure 3d. History of the matrix method

calculating irrotational flow around arrays of airfoils. These methods are the conformal mapping method, the singularity method, the streamline curvature method, and the matrix method. Hansen (1976) described the basic concept behind each method and the history of the development of each method. It was felt that the best type of inviscid method to use to solve for the flow on an axially symmetric blade-to-blade surface is one which is general enough to include the effects of compressibility, and the affects of an axial velocity-density product change and a radius change across a blade row. The streamline curvature method and the matrix method are sufficient in these respects.

There are several problems which arise when an irrotational flow model is used for airfoil or cascade calculations. At the trailing edge the irrotational flow requires a stagnation point, but in the real flow there is no such stagnation point. Therefore, the pressure field as calculated must be modified near the trailing edge to approximate the actual viscous pressure distribution. Also, as shown by Miller and Serovy (1975), given a fixed inlet angle to a cascade with rounded or blunt trailing edges, there are an infinite number of solutions possible unless the outlet angle is somehow fixed. This can be accomplished by setting equal estimated pressures on the suction and pressure surfaces or by fixing the position of the irrotational stagnation streamline at the trailing edge. Dodge (1973), Miller and Serovy (1975), and Ispas (1974) have used irrotational cascade flow models to determine turning in a cascade by applying some specific conditions in the flow field near the trailing edge. Dodge (1973) set

the velocities on the suction and pressure surfaces equal at the first grid (computation) points upstream of the trailing edge. Miller and Serovy (1975) set the velocities equal at the trailing edge after extending the velocities to the trailing edge in several different ways and varied the position of the stagnation point on the trailing edge circle. Ispas (1974) fixed the distribution of the axial velocity-density product in the blade-to-blade direction from the pressure surface trailing edge to the suction surface trailing edge. All these calculations gave turning angles that were within 3 degrees of the experimental angles at low incidence. However, for flows when the experimentally-measured turning begins to decrease with an increase in incidence angle, the inviscid analysis alone shows no such decrease. This points to the fact that the inviscid model alone is not an adequate model, and that it is necessary to include viscous effects in the analysis.

Viscous Flow Models

Because viscous analysis of the flow through a cascade is necessary for the calculation of losses and has been suggested as necessary to obtain the correct outlet angle, the types of viscous regions encountered on a blade in a cascade must be determined so that appropriate calculation models can be used.

A qualitative look at what happens to the boundary layer on a blade as the incidence is varied is shown for a particular blade in Figure 4. This shows that there can be significant regions of laminar, transitional and turbulent flow on a blade and that a laminar separation bubble near

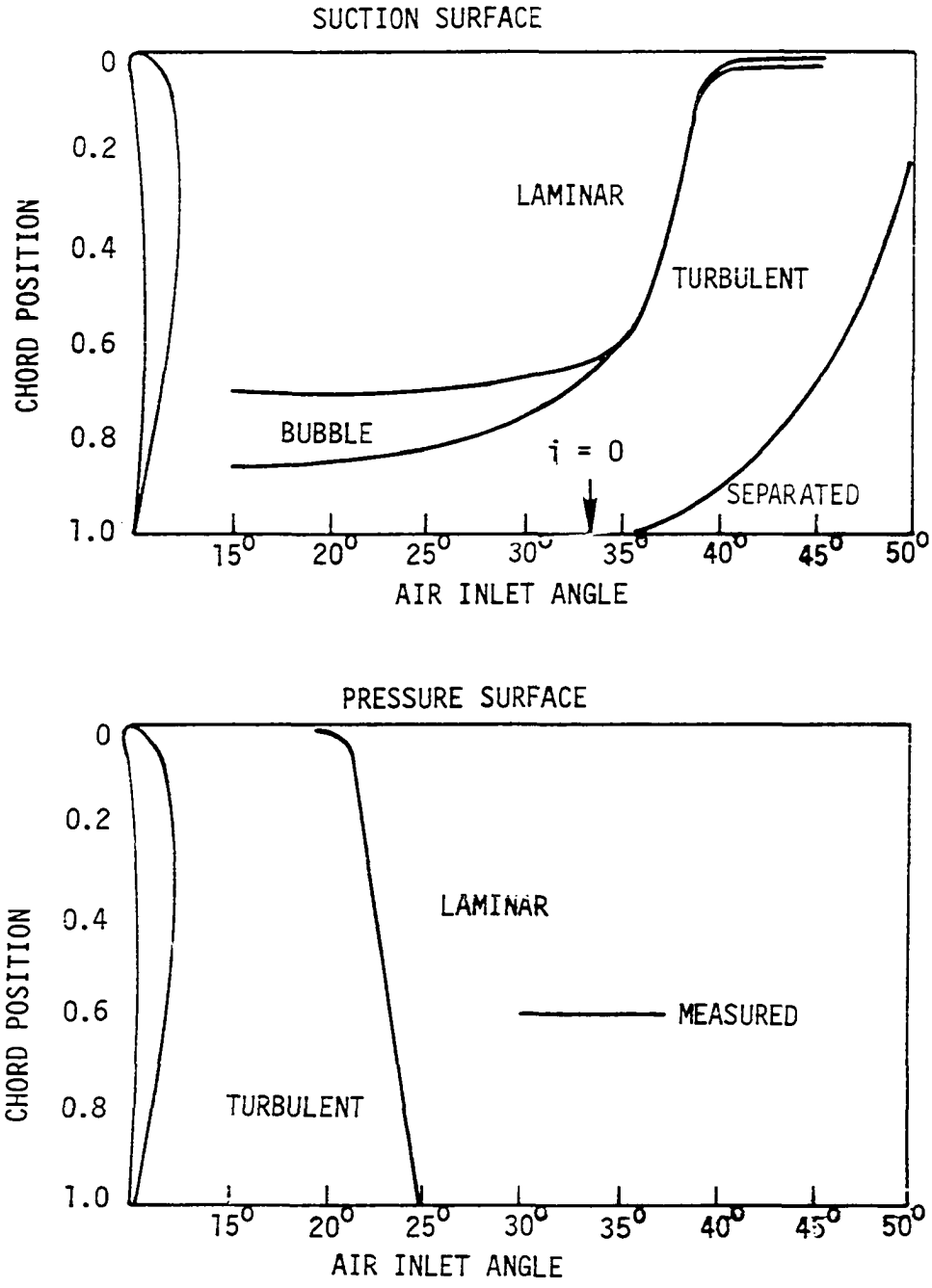

Figure 4. Seyb's (1965) measured boundary layer development. (Profile 10C7 41.8 C50, stagger angle 12.6°, pitch/chord = 0.76, Re_c = 1.5 x 10^5, T_u = 2.6%.) from Horlock (1970).

the leading edge and turbulent separation at the trailing edge may develop as the incidence angle is increased. This suggests that it should be possible for any calculated boundary layer to be initially laminar, with a provision for transition to turbulent flow or laminar separation and reattachment, and to continue as turbulent flow with a provision for modeling a turbulent separated region.

The equations of motion for the flow in a compressible boundary layer are given by White (1974, p. 626)

$$\frac{\partial}{\partial x}(\overline{\rho}\,\overline{u}) + \frac{\partial}{\partial y}(\overline{\rho\, v}) = 0 \tag{4}$$

$$\overline{\rho}\,\overline{u}\,\frac{\partial \overline{u}}{\partial x} + \overline{\rho v}\,\frac{\partial \overline{u}}{\partial y} = \rho_e U_e \frac{dU_e}{dx} + \frac{\partial}{\partial y}\left(\overline{\mu}\frac{\partial \overline{u}}{\partial y} - \overline{\rho u'v'}\right) \tag{5}$$

$$\overline{\rho}\,\overline{u}\,\frac{\partial \overline{h}}{\partial x} + \overline{\rho v}\,\frac{\partial \overline{h}}{\partial y} = \overline{u}\,\frac{\partial \overline{p}}{\partial x} + \frac{\partial}{\partial y}\left(\overline{k}\,\frac{\partial \overline{T}}{\partial y} - \overline{\rho v'h'}\right) + \left(\overline{\mu}\,\frac{\partial \overline{u}}{\partial y} - \overline{\rho u'v'}\right)\frac{d\overline{u}}{dy} \tag{6}$$

$$\overline{p} = \overline{\rho} R \overline{T} \tag{7}$$

$$d\overline{h} = C_p d\overline{T} \tag{8}$$

with appropriate boundary conditions. The assumptions made in arriving at these equations are that the flow is two-dimensional, compressible, steady, and has a high Reynolds number, that the boundary layer is thin with respect to the longitudinal direction and the longitudinal radius of curvature (if the surface is curved), and that the term $\overline{\rho u'v'}$ is

the dominant Reynolds stress term.

If these equations are assumed adequate for the viscous flow, the problem then is to model the Reynolds stress, $\overline{\rho u'v'}$, and the Reynolds heat flux, $\overline{\rho v'h'}$, and to solve the set of equations for u,v,ρ, and T. Various models from the simple eddy viscosity concept to the more complex turbulent energy methods have been proposed. The eddy viscosity formulations have been adequate for the representation of most attached boundary layer flows. There has been recent interest in turbulence energy methods because of the failure of the eddy viscosity model in special cases such as suction or blowing and in other types of viscous flow such as jets and three-dimensional boundary layers. There are also many ways to solve the original equations. Prior to the computer, integral methods were developed, which were integrated forms of the original partial differential equations. The resulting ordinary differential equations were then solved in many different ways. As the computer made calculations easier, integral methods remained and were improved and methods were developed which solved the partial differential equations by representing the partial derivatives as approximate derivatives between calculation grid points. Finally, as stated by Pletcher (1974), differential methods of solving the governing conservation equations have been shown to be an effective way of predicting turbulent flows under a wide range of conditions, including heat transfer and pressure gradients. Mixing length or eddy viscosity models have also been found to be remarkably general, being to a large degree independent of Mach number, heat transfer, and pressure gradient.

Inviscid-Viscous Flow Interaction Models

Attempts have been made to calculate the flow around airfoils and through cascades by a number of authors. The method usually used has been an inviscid-viscous interaction type in which the potential flow field around the true profile shape is first calculated to obtain the surface pressures. These pressures are then used to calculate the boundary layers on the profiles, and the boundary layer displacement thickness is then used to modify the original profile shape. Beyond this initial similarity, the methods differ in the way the profile is thickened, in how the input to the boundary layer flow is obtained from the inviscid flow field, in the closure condition used to obtain the outlet angle, in the way separation is handled, and in the way matched inviscid-viscous solutions are obtained. In the following, methods used to calculate viscous flow around single airfoils will be discussed. Then methods used to calculate viscous flow through cascades will be described.

Bavitz (1975), Callaghan and Beatty (1972), Morgan (1975), and Stevens et al. (1971) include the viscous displacement effect by adding the displacement thickness to an original isolated airfoil geometry to obtain a new geometry, while Dvorak and Woodward (1975), Jacob (1969) and Klineberg and Steger (1972) inject irrotational fluid along the profile surfaces in the inviscid calculation. When adding the displacement thickness to the original airfoil geometry a problem arises which is seldom found when fluid is injected along the surface. If the boundary layer displacement thickness is not smooth (i.e., if there are second

derivatives with alternating signs along the surface), the new geometry produces a surface velocity distribution with unwanted peaks. This situation is helped by smoothing the displacement thickness distribution prior to adding it to the airfoil geometry. A brief description of the rest of each author's method follows. A summary of the inviscid-viscous iterative calculation procedures for isolated airfoils is given in Table 1.

Bavitz (1975) used the closure condition of continuous velocities at the trailing edge. He modified the surface pressures near the trailing edge by taking the maximum pressure surface C_p on the rear portion of the blade and holding it constant from that point to the trailing edge. The most downstream point at which the calculated surface pressure is used on the suction surface is determined empirically. The pressure distribution from that point to the trailing edge is determined by fitting a second order polynomial to the surface pressures at that point, the point before it, and the pressure at the trailing edge on the suction surface (which is equal to the pressure on the pressure surface at the trailing edge). The displacement thickness in the separated regions is determined by the points 8 and 10 percent chord before separation and an empirical relation based on the pressure coefficients. Interaction between the viscous flow and inviscid flow is produced by applying fully each new boundary layer thickness until the solution converges. Also the potential flow mesh is changed from a coarse, to a medium, to a fine mesh as the solution converges with an iteration limit on the coarse mesh of 6 iterations, the medium, 4, and the fine, 3.

Table 1. Summary of inviscid-viscous iterative calculation procedures for isolated airfoils

Inviscid-Viscous Airfoil Analysis	Inviscid Flow Calculation Method	Viscous Region Calculation	
		Boundary Layer	Separated Flow Region
Jacob (1969)	Jacob (1969)	Rotta (see Jacob (1969)) Integral	Injection to produce a constant pressure downstream
Stevens et al. (1971)	Stevens et al. (1971)	Nash (1967) Integral	The calculations were desensitized so that separation did not occur
Callaghan & Beatty (1972)	Douglas Neumann Method Hess & Smith (1966)	Cebeci & Smith (1968) Differential	Empirical model
Klineberg & Steger (1972)	Steger & Lomax (1971)	Klineberg & Steger (1972) Integral	Specify the displacement thickness and calculate the pressure
Bavitz (1975)	Garabedian & Korn (1971)	Bradshaw & Ferriss (1971) Integration by method of characteristics	Extrapolation of the displacement thickness
Dvorak & Woodward (1975)	Dvorak & Woodward (1975)	Cumpsty & Head (1967) Integral	The source strength at the trailing edge was limited
Morgan (1975)	Oellers (1971)	Modified Truckenbrodt (1952) Integral	-

Interaction Method		Type of Isolated Airfoil Tested
Displacement Thickness Effect Included By:	New Displacement Thickness Level	
Injection beginning at separation	-	Single element
Modifying the original profile shape	$\frac{2}{3}\delta^*_{new} + \frac{1}{3}\delta^*_{old}$	Multielement
Modifying the original profile shape	Full displacement thickness	Multielement
Matching velocities at the boundary between the inviscid and viscous flows		Transonic symmetrical single element
Modifying the original profile shape	Full displacement thickness	Transonic single element
Injection	$\frac{1}{2}\delta^*_{new} + \frac{1}{2}\delta^*_{old}$	Multielement
Modifying the airfoil thickness and camber	$\frac{2}{3}\delta^*_{new} + \frac{1}{3}\delta^*_{old}$	Multielement

Callaghan and Beatty (1972) used the Douglas-Neumann potential flow method to calculate surface pressures which are not modified in the trailing edge region. Separation is accounted for by a semiempirical model. The interaction is produced by adding the entire displacement thickness to the original blade geometry for two to three iterations.

Morgan (1975) accounted for the effect of the displacement thickness by adding it to the airfoil geometry in terms of thickness and camber. The closure condition of equal velocities on the pressure and suction surfaces becomes the condition of vortex singularities of equal strength and opposite sign on the suction and pressure surfaces at the trailing edge in this particular potential flow program. To insure proper convergence in four to five iterations the new displacement thickness to be applied to the original blade geometry is equal to 1/3 of the old displacement thickness plus 2/3 of the displacement thickness just calculated from the viscous program.

Stevens et al. (1971) used the closure condition of vortex singularities of equal strength and opposite sign on the suction and pressure surfaces at the trailing edge and modified the surface pressure distribution of up to 32 points along the surface by discarding the last 2 points, curve fitting the 5 previous points and then obtaining surface pressures to the trailing edge. To insure proper convergence in several iterations the new displacement thickness is equal to 1/3 of the old displacement thickness and 2/3 of the newly calculated displacement thickness.

Dvorak and Woodward (1975) obtained closure condition equivalent to equal

pressures at the trailing edge by requiring no flow normal to the airfoil surface at the trailing edge and obtained surface pressures at the trailing edge by linearly extending the pressures from the last two points before the trailing edge. Convergence in two to five iterations was insured by adding a displacement thickness equal to the sum of 1/2 the old plus 1/2 the newly calculated displacement thickness.

Jacob (1969) used the surface pressures from a potential flow solution to calculate the boundary layer and its separation point. Then three pressures, the pressure at the suction surface separation point, the suction surface pressure at the trailing edge at the displacement thickness boundary and the pressure at the separation point on the pressure surface, are set equal by changing the circulation and adding a source distribution of appropriate strength beginning at the separation points, so as to produce a constant pressure downstream of the separation points.

Klineberg and Steger (1972) were particularly interested in separation and therefore used a symmetrical airfoil at zero angle of attack so that the circulation was zero. The displacement thickness was applied to the inviscid flow and velocities were matched at the inviscid-viscous boundary. The boundary layer including a separated region was calculated by an integral relation. In the separated region the streamline angles of the outer inviscid flow were known and with these the boundary layer equations were integrated to obtain the pressure distribution. Convergence for the case run was obtained in 12 iterations.

The methods used to calculate the flow through airfoil cascades are very much similar to those just described for single airfoils.

Again it is found that some authors change the original blade geometry to account for the displacement thickness (Speidel (1954), Föttner (1972) and Sanger (1973)), while others (Föttner (1968), and Geller (1972)) use injection along the blade surface. A summary of the inviscid-viscous iterative calculation procedures for airfoil cascades is given in Table 2.

Speidel (1954) obtained a potential flow solution through a cascade by modeling the blade thickness with a source distribution and the camber line with distributed vortices. The boundary layer was calculated by the method of Truckenbrodt (1952) and any separated region was modeled by Speidel's own method. The camber line and the turning of the cascade are modified by the difference in the suction and pressure surface displacement thicknesses and the potential flow though the cascade was again calculated. Finally, the loss and turning were calculated.

Sanger (1973) used the criteria of equal pressures on the suction and pressure surfaces to obtain an initial inviscid solution. Then using the surface pressures, boundary layers were calculated and the displacement thicknesses were added to the original blade profile. The inviscid calculation was then carried out around the thickened profile with the outlet angle determined from the average of the thickened profile surface angles on the suction and pressure surfaces where the profile joins the trailing edge circle. The thickened profile beyond separation was obtained by continuing from the separation point to the trailing edge in a smooth extrapolated curve. The additional loss

Table 2. Summary of inviscid-viscous iterative calculation procedures for airfoil cascades

Inviscid-Viscous Cascade Analysis	Inviscid Flow Calculation Method	Viscous Region Method		Interaction Method		Cascade Type and Blade Type Tested
		Boundary Layer	Separated Flow Region	Displacement Thickness Effect Included By	New Displacement Thickness Level	
Speidel (1954)	Speidel (1954)	Truckenbrodt (1952) Integral	θ Calculated at the trailing edge Speidel (1954)	Modifying the Camber line shape only	-	2-D Decelerating NACA 0010 0015 0020
Föttner (1968)	Schlichting (1955)	Scholz (1960) Truckenbrodt (1952) Integral	None described	Injection	Full displacement thickness	2-D Decelerating NACA 65-(12 A_{10})06
Föttner (1972)	Shaalan & Horlock (1968)	Scholz (1960) Truckenbrodt (1952) Integral	H=constant, correlation for θ change	Modifying the original profile shape	Full displacement thickness	2-D Decelerating NACA 65-0010 with a circular Camber line
Geller (1972)	Martensen (1959)	Walz (1966) method II Integral	Injection to produce a constant downstream pressure	Injection beginning at separation	-	2-D Decelerating NACA 65-($4A_2I_{8b}$)10 65-($8A_2I_{8b}$)10 65-($12A_2I_{8b}$)10 Accelerating, Camber angle = 110°
Sanger (1973)	Katsanis (1969)	McNally (1970) Integral	Manual extrapolation	Modifying the original profile shape	Full displacement thickness	Compressor stator double circular arc

because of separation is accounted for by the method of Speidel (1954).

Föttner (1968) set the trailing edge pressures equal to obtain the first inviscid surface pressure solution which produced the first boundary layer solution. The displacement thickness was then added to the profile as a source distribution, producing a finite trailing edge thickness. The potential flow around this profile is again calculated and the values of surface pressure used to obtain second boundary layer solution. This procedure then continued to convergence.

Geller (1972) applied a method similar to the airfoil method of Jacob (1969) to cascades. Initially the boundary layer separation point locations on the suction and pressure surfaces were estimated. The potential flow was then calculated with the addition of an after-separation source distribution of sufficient strength to produce a constant pressure from the separation point to the trailing edge. The trailing edge pressures (on the suction and pressure surfaces) were then required to be equal and thus formed a closure condition which fixed the outlet angle. The surface pressures from the first potential solution then served as input for the boundary layer calculation which gave a better estimate of the separation points. With these better estimates of the separation points, the cycle was again repeated and a final solution was then obtained.

PRESENT BLADE-TO-BLADE COMPUTATION METHOD

The present model for the calculation of the viscous flow through a blade cascade using an inviscid-viscous interaction technique consists of a computer program for the calculation of the inviscid flow through the blade cascade, a computer program for the calculation of the viscous region near the blades, and a computer program to interact the previous two in such a way that matched viscous and inviscid solutions are obtained.

Inviscid Flow

The computer program for the calculation of the inviscid flow was selected because of its generality. It includes compressible effects and changes in the axial velocity-density product. This program written by Katsanis and McNally (1969) solves

$$\frac{1}{r^2}\frac{\partial^2\psi}{\partial\theta^2}+\frac{\partial^2\psi}{\partial m^2}-\frac{1}{r^2}\frac{1}{\rho}\frac{\partial\rho}{\partial\theta}\frac{\partial\psi}{\partial\theta}+\left[\frac{\sin\alpha}{r}-\frac{1}{b\rho}\frac{\partial(b\rho)}{\partial m}\right]\frac{\partial\psi}{\partial m}=\frac{2b\rho\omega}{w}\sin\alpha \qquad (9)$$

which is the equation for irrotational, compressible flow, written in terms of a stream function, for an axially symmetric surface, Figure 2. This program, TSONIC, uses a rectangular grid, Figure 5, to obtain the points at which Equation 9 is solved. The position of the upstream and downstream boundaries and the size of the rectangular mesh were determined according to suggestions given by Miller (1973) and their particular values will be discussed in the fourth section. The boundary conditions for the

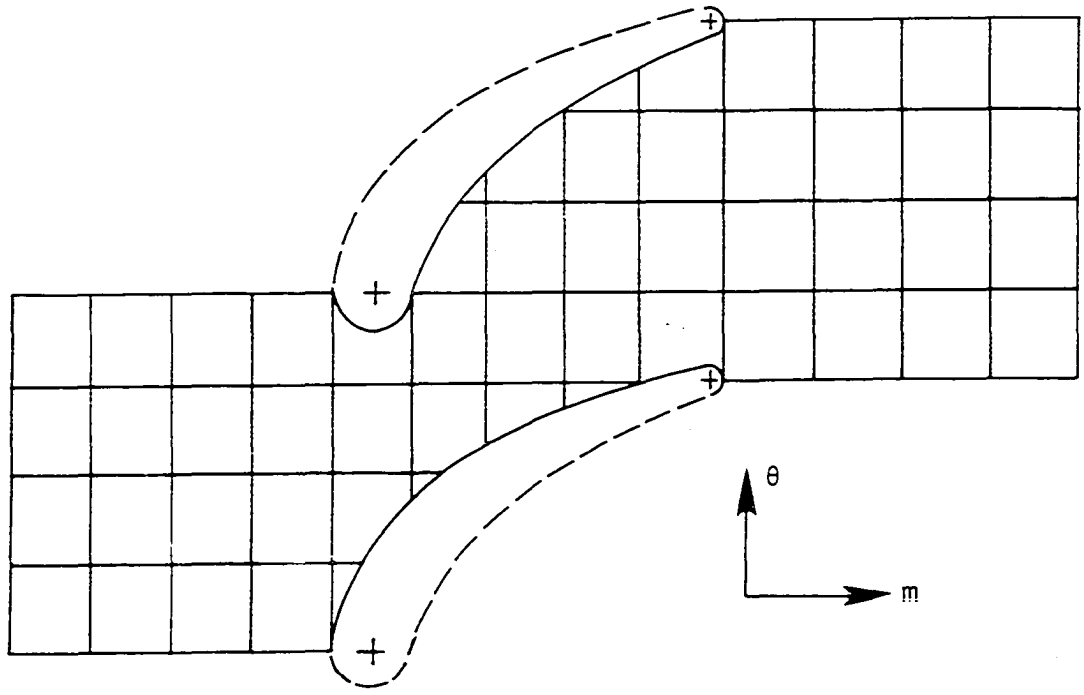

Figure 5. Grid system used by Katsanis and McNally (1969).

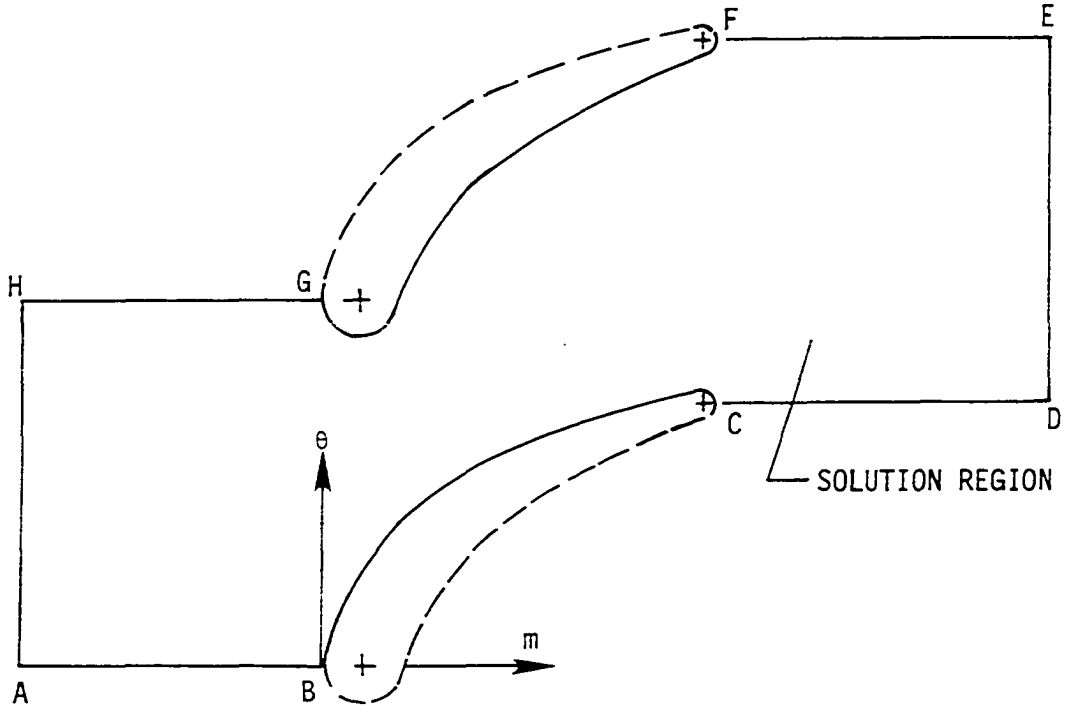

Figure 6. Two dimensional solution region.

solution region, Figure 6, are as follows. There is a fixed flow rate, w, through the passage. The inlet flow angle along AH and the outlet flow angle along DE are known. AB, HG and CD, FE are periodic such that the solutions along AB and HG are the same and along CD and FE are the same. Initially both blade surfaces, BC and GF, have constant, though different, stream function values along the surfaces.

When one wishes to include the displacement effect of a boundary layer on the inviscid flow around the blades, it is found that this displacement effect can be modeled by injecting fluid (in the inviscid calculation) from the blade surface along the blade as suggested by Lighthill (1958). This is done by varying the value of the stream-function boundary conditions along the blade. The streamfunction is normalized by w, the total weight flow through the passage, so that initially along BC, ψ=0 and along GF, ψ=1. When fluid is injected, beginning at the first vertical mesh line downstream of the leading edge, these boundary conditions are changed to account for the extra fluid. The extra amount of fluid is $\Delta\psi = \frac{u\rho b\delta^*}{w}$, where u,$\rho$,b, and δ^* are respectively the fluid velocity, the density, the streamsheet thickness and the displacement thickness at the point along the surface where ψ is being calculated. Then along BC, $\psi = -\frac{u\rho b\delta^*}{w}$, and along GF, $\psi = 1 + \frac{u\rho b\delta^*}{w}$. There is also injection at the trailing edge to account for the finite thickness of the trailing edge, Appendix A. The extra mass was added to the fluid stream by injection continuing downstream and is accounted for along the periodic boundaries and at the downstream boundary.

Viscous Flow

The boundary layer program used in the present model is a version of the Albers and Gregg (1974) program which was recoded by Albers and Gregg to more efficiently use computer storage space with no change in the fluid mechanics. It was then modified in the present method to calculate through laminar and turbulent separation and to link with the interaction program. The Albers and Gregg program was selected because it includes laminar, transitional, and turbulent boundary layer calculations which, as suggested previously, all may be required. Because the Albers and Gregg method is a differential as opposed to an integral boundary layer method, it provides an opportunity to calculate some regions of separation. Figure 7 compares the calculated boundary layer with cascade results of Peterson (1958) where his surface pressure data is used as input to the boundary layer program, with an initial boundary layer thickness obtained from a method which is described in the following paragraph. The calculation and the experimental data match fairly well, particularly at the transition point where there is a definite change in slope.

Initial boundary layer

Although it is possible to start the boundary layer calculation within the program from the stagnation point, because of the difficulty of correctly placing on adequate number of points in the steep velocity gradient near a stagnation point, the method of Schlichting (1968, p. 87), was used to provide an initial boundary layer thickness. For flow near

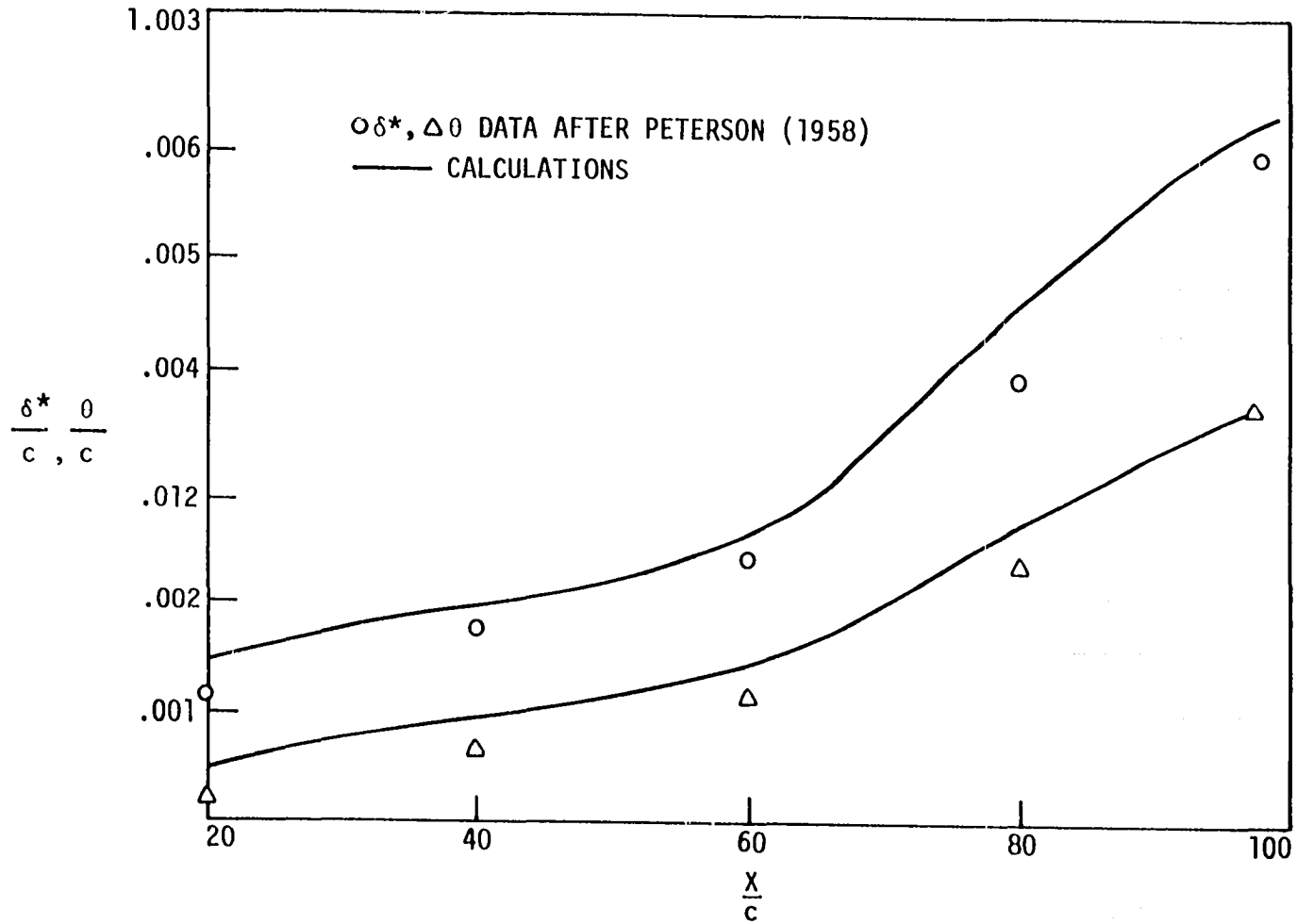

Figure 7. Calculation using Albers and Gregg (1974) program with experimental pressure input compared with the experimental data of Peterson (1958). 65-410 cascade, $m_1 = 0.1$, $Re_c = 245{,}000$, $\gamma = 45^o$, $\sigma = 0.78$, $c = 124$ mm.

the stagnation point of a flat plate placed normal to the free stream Schlichting derived $\delta=2.4\sqrt{\nu/a}$ and a distribution of $\frac{u}{U_e}$ as a function of $\sqrt{a/\nu}\,y$ where a is obtained from U = ax. When this method of calculation is applied to the leading edge of an airfoil, the stagnation point location and a velocity and its location somewhat downstream of the stagnation point must be known to obtain the average velocity gradient, $a = \frac{dU_e}{ds}$. A problem arises here in the inviscid calculation in that the mesh is not fine enough to locate the stagnation point. As shown in Figure 8, the stagnation point is then estimated and the distances to the first points where the velocities are known are estimated using the inlet angle and leading edge radius to obtain the arc length as shown. This information gives an estimate of the velocity gradient, a, which in turn gives an estimate of the initial boundary layer size at that location. It is possible to use other programs to obtain a more detailed solution near the leading edge, but this involves a considerable increase in computational effort. The boundary layer thickness and velocity distribution are then calculated in the interaction program and used as input to the boundary layer program.

Calculation step sizes

In the Albers and Gregg (1974) program, the input velocities are specified at calculation stations along the profile surface length s. In regions of steep velocity gradients or rapid boundary layer growth it is important to closely space the steps. The sizes of the steps for the present model were chosen as $\Delta s = 4\delta^*$ for the first ten steps from the

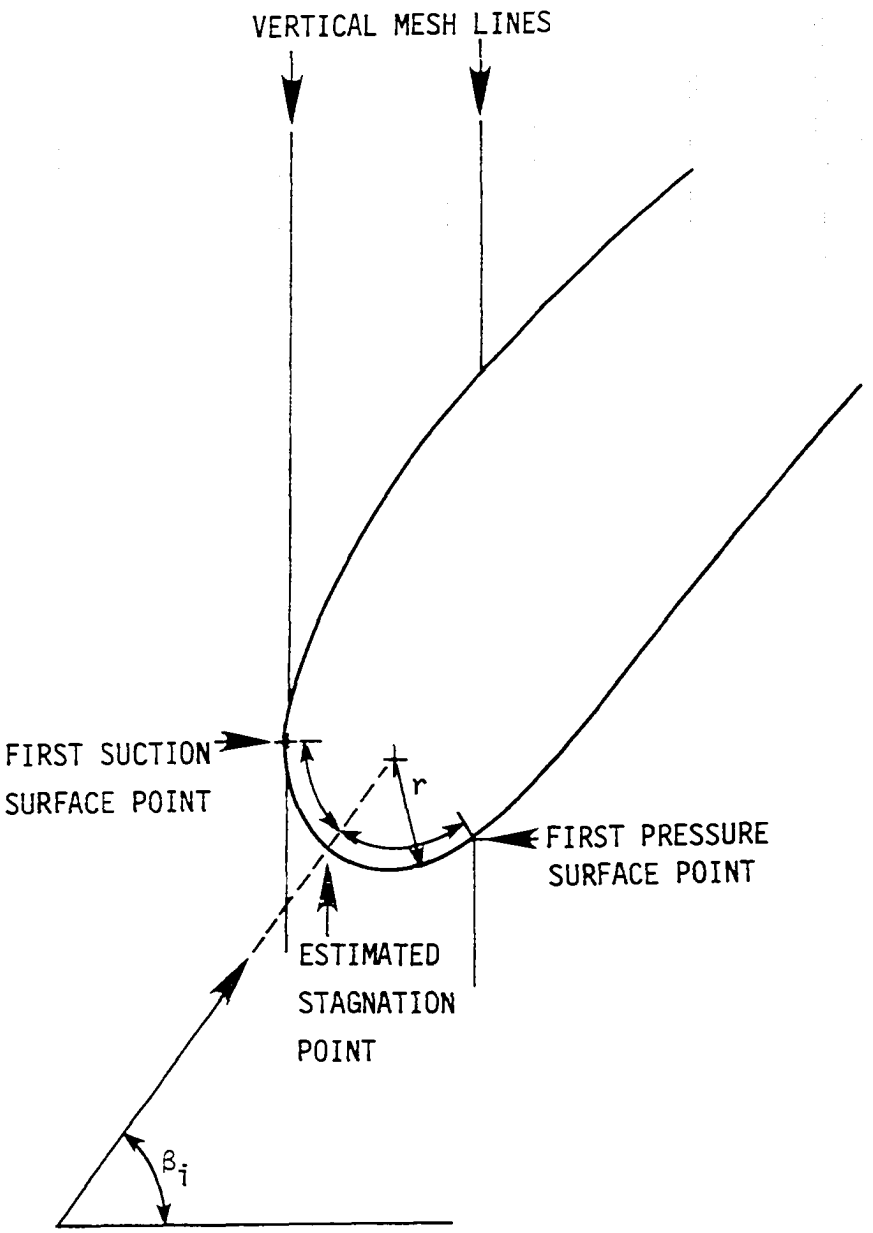

Figure 8. Estimation of the stagnation point location

leading edge on the suction and pressure surfaces (where the pressure gradient is very steep), as $\Delta s = 18\delta^*$ from the tenth step to a point just downstream of half of the length s of the blade, and as $\Delta s = c/60$ to the trailing-edge end of the blade surface.

Transition

Transition was calculated using the model already built into the Albers and Gregg program. The transition region, begins when $\frac{\delta^* U_e}{\nu}$ becomes greater than the critical Reynolds number and ends when it becomes greater than the fully turbulent Reynolds number, where both the critical and the fully turbulent Reynolds numbers are obtained from empirical relations within the program. Within the transition region the effective viscosity ν_{eff} is varied from ν at the beginning to $\nu+\nu_t$ at the end of transition. ν_t is obtained from a two-layer algebraic model described by Herring and Mellor (1972).

Laminar separation

The change from laminar to turbulent flow can also occur when there is a laminar separated flow region. The laminar separation model in the Albers and Gregg program was not considered adequate and was replaced as follows. Horton (1967) suggested a method for prediction of reattachment and boundary layer growth across the separated region. Roberts (1975) used Horton's method, compared it with experimental data, and modified some constants to obtain a method which matches his own experimental data. Robert's (1975) method is used for the calculation of regions of laminar separation as follows. At the separation point, s_{sep}, the Reynolds number based on the momentum thickness, $Re_{\theta_{sep}} = \frac{U\theta_{sep}}{\nu}$

is known. Then knowing $Re_{\theta_{sep}}$ and the inlet Taylor's turbulence factor, (TF), ℓ_1 (See Figure 9) can be calculated as,

$$\ell_1 = \theta_{sep}(2.5 \times 10^4)\log_{10}(\coth(TF \times 10))/Re_{\theta_{sep}} \tag{10}$$

ℓ_1 is the region after separation where the boundary layer thickness grows rapidly and the velocity is assumed to remain constant. In a separated boundary layer, where the pressure gradient is zero, the momentum thickness remains constant so that,

$$\theta_{sep} = \theta_{tr}. \tag{11}$$

From the transition point to the reattachment point, the velocity is modeled as a linear distribution (Figure 9) and

$$\ell_2 = \theta_{sep} \cdot \frac{B_1(1-\bar{U}_{e_r})}{(\bar{U}_{e_r})^4 - C_1} \tag{12}$$

where

$$B_1 = \frac{1}{\frac{C_{dm}}{4H_{em}} - \Lambda_R} \qquad C_1 = \left(\frac{C_{dm}}{4H_{em}}\right) \cdot B_1$$

and the momentum thickness at reattachment is

$$\theta_r = \frac{\theta_{sep}}{\bar{U}_{e_r}^3} + \frac{\theta_s C_{dm}}{4H_{em}} \frac{(1-\bar{U}_{e_r}^4)\ell_2/\theta_{sep}}{\bar{U}_{e_r}^3(1-\bar{U}_{e_r})} \tag{13}$$

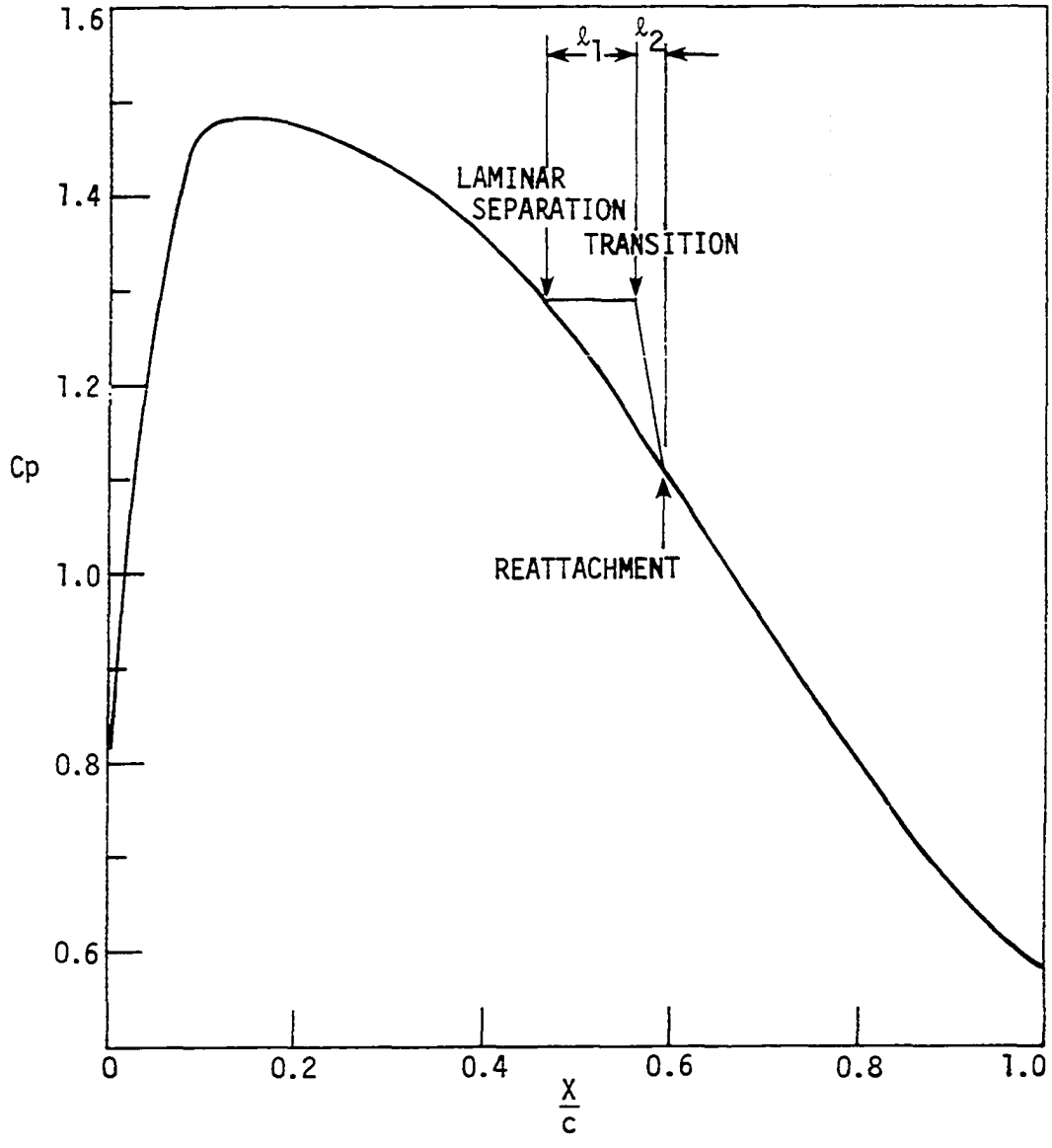

Figure 9. Suction surface pressure distribution on a 65-(12)10 blade cascade corresponding to the calculation point Re_c = 220,000 in Figure 34 showing the idealized perturbation of the pressure because of laminar separation.

where

$$C_{dm} \simeq 0.035, \quad H_{em} \simeq 1.5, \quad \Lambda_R = -0.0059.$$

However, it can be seen that if in Equation 12 $(\bar{U}_{e_r}{}^4 - C_1)$ approaches 0, by $\bar{U}_{e_r}$ decreasing, ℓ_2 approaches infinity. In some cases ℓ_2 can produce a reattachment point beyond the trailing edge of the blade. This describes a failure of the reattachment process called bursting by Roberts (1975). In these cases the laminar separation produces such a large effect on the inviscid flow that the inviscid velocity distribution can not be simply modified as in Figure 9.

The present calculations use Roberts (1975) model for laminar separated regions modified as follows to include the bursting case. Equations 11, 12, 13 and 14 are repeated below with the appropriate constants inserted. The equations are otherwise unchanged except as noted below.

$$\ell_1 = \theta_{sep} \, (2.5 \times 10^4) \log_{10}(\coth(T_u x 20)) / Re_{\theta_{sep}} \tag{14}$$

$$\theta_{sep} = \theta_{tr} \tag{15}$$

$$\ell_2 = \theta_{sep} \times 85.227 \times (1.-\bar{U}_{e_r}) / (\bar{U}_{e_r}{}^4 - .497) \tag{16}$$

$$\theta_p = \theta_{sep} \, (1 + .005833 \times (1.-\bar{U}_{e_r}{}^4) \times \ell_2/\theta_{sep}/\bar{U}_{e_r}{}^3/(1-\bar{U}_{e_r})) \tag{17}$$

Equation 14 is slightly different from Equation 11 in that TF was replaced by 2(Tu) according to Roberts' (1973) Figure 84.

When separation occurs, s_{sep}, $R_{\theta_{sep}}$, Tu, and θ_{sep} are known. ℓ_1 is found from Equation 14 which gives the first estimate of the reattachment as $s_{sep} + \ell_1 = s_r$. Then the velocity is found at s_r and Equation 16 is used to find ℓ_2. Next, $s_{sep} + \ell_1 + \ell_2 = s_r$ gives a new estimate for the reattachment position, the reattachment velocity, and ℓ_2. Iteration continues until ℓ_2 is converged upon. However, as noted previously, as $\bar{U}_{e_r}^{4}$ approaches 0.497 in Equation 16, ℓ_2 grows without bounds and the calculated s_r extends beyond the trailing edge of the blade, which indicates bursting. In the present computations, ℓ_2 is limited in size to 0.7 (ℓ_1) based on Roberts (1973), Figure 19c. Also, $\bar{U}_{e_r}$ is required to be greater than 0.841 to keep the value of ℓ_2 positive. Then knowing $\bar{U}_{e_r}$, ℓ_2, and θ_s, Equation 17 gives θ_r. The velocity distribution, $\frac{u}{U_e} = \frac{y}{\delta}$, whic is quite similar to profiles given by Horton (1967), is used with θ_r and $\delta_r^* = 3.0\ (\theta_r)$ to begin the turbulent calculation of the rest of the boundary layer, beginning at the reattachment point.

Turbulent separation

In the present model the Albers and Gregg program is extended to calculate separated boundary layers in a way similar to the method of Carter and Wornom (1975). In the Carter and Wornom procedure the displacement thickness is prescribed, but in the Albers and Gregg program used here the edge velocity is prescribed. Carter and Wornom (1975) first followed Reyhner and Flügge-Lotz (1968) by neglecting the streamwise convection term in the boundary layer equations when there is backflow (i.e., in $\rho u \frac{\partial u}{\partial s} + \rho v \frac{\partial u}{\partial y} = \rho_e u \frac{du}{ds} + \frac{\partial \tau}{\partial y}$, when $\rho u < 0$, $\rho u = 0$). They also suggested that

there was a lack of diagonal dominance in the tridiagonal system of equations to be solved within the boundary layer program. In the Albers and Gregg (1974) program the equation

$$-a_{3j}f'_{j+1} + a_{2j}f'_j - a_{1j}f'_{j-1} = a_{4j} \tag{18a}$$

is solved at each forward marching step by evaluating the a's with the best estimate of the f solution, then solving for the new f's and updating the a's until an f solution is converged upon. However, when a_{2j} is not dominant, the f solution diverges instead of converging. Comparing Equation 18a with that of Carter and Wornom (1975), the modified equation to prevent divergence becomes

$$-a_{3j}f'_{j+1} + (a_{2j}+\alpha)f'_j - a_{1j}f'_{j-1} = a_{4j} + \alpha f'_{jp}, \tag{18b}$$

where f'_{jp} is the value of f' at j from the previous iteration on f. Notice that the original and the modified equations are the same at convergence when $f'_j = f'_{jp}$. An example result of this modification is shown in Figure 10. The calculation does not diverge even though δ^* is increasing at a very large rate. The magnitude of the reverse flow $(\frac{u}{U_e})$ at the last 3 s steps is about 20% of the freestream value.

There are cases where, because of the large backflow regions, the calculation does diverge. In these cases a different calculation method was used to give a solution from the point of divergence to the trailing edge. At the last acceptable s step before divergence the displacement and momentum thicknesses are used to start the new calculation which is derived from the Von Karman integral boundary layer equation, $U^2 \frac{d\theta}{ds} + (2+H)\theta U \frac{dU}{ds} = \frac{\tau_w}{\rho}$. In the separated region we assume $\frac{\tau_w}{\rho} = 0$ and

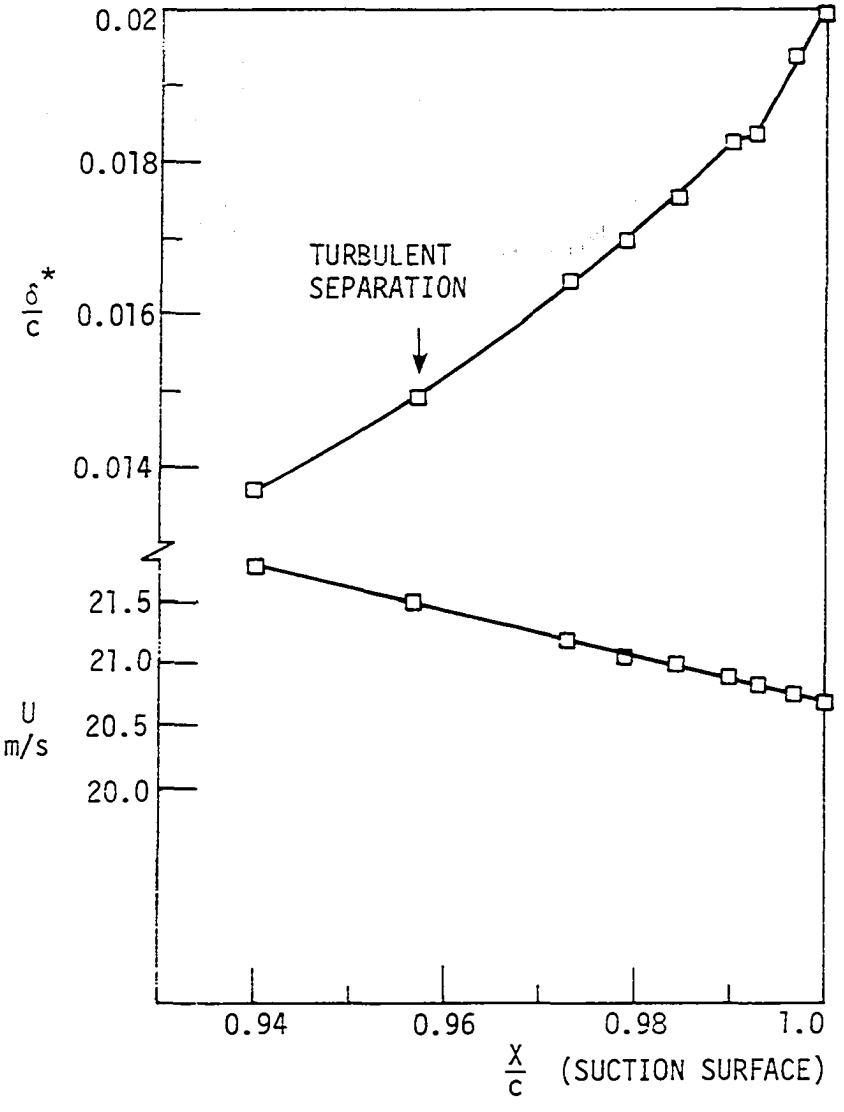

Figure 10. Calculated boundary layer growth in a separated region using the Albers and Gregg (1974) program and the Carter and Wornom (1975) modification near the trailing edge of the 65-410 blade cascade corresponding to an intermediate calculation for the point $\alpha = 12.4^{o}$ in Figure 23.

H is known. However, H is not known, but is known to increase in a separated zone. Therefore, H at the trailing edge, in an increasing pressure gradient is approximated by H at the last acceptable point plus 1.0. The H's at points between the last calculated acceptable point and the trailing edge point are obtained by linear interpolation. H in a decreasing pressure gradient is held constant after separation. Setting $\tau_w/\rho=0$ the Von Karman integral equation becomes $\frac{d\theta}{ds}=\frac{(2+H)\theta}{U}\frac{dU}{ds}$. This equation is solved for θ and δ^*, knowing H and u as functions of s as shown in Appendix B. Figure 11 shows how δ^* and θ were extended in one particular case.

Inviscid-Viscous Flow Interaction

The present method of interacting the inviscid flow solution and the viscous (boundary layer) flow solution is similar to that of Brune et al. (1974). It is different from the previous methods of interacting inviscid and viscous flows which obtain an inviscid solution and a corresponding viscous solution, apply the first trial boundary layer displacement thickness to the blade surface to obtain new inviscid and viscous solutions and continue until a convergent result is reached. To insure convergence, the latter methods often require artificial damping obtained by using a reduced displacement thickness, $\delta^* = q\delta_{old} + (1-q)\delta_{new}$, where q is less than 1. Figure 12 shows the difference between these two methods. The two lines on the figure are the inviscid line, which shows how a typical local surface velocity changes with a change in displacement thickness in the inviscid solution, and the

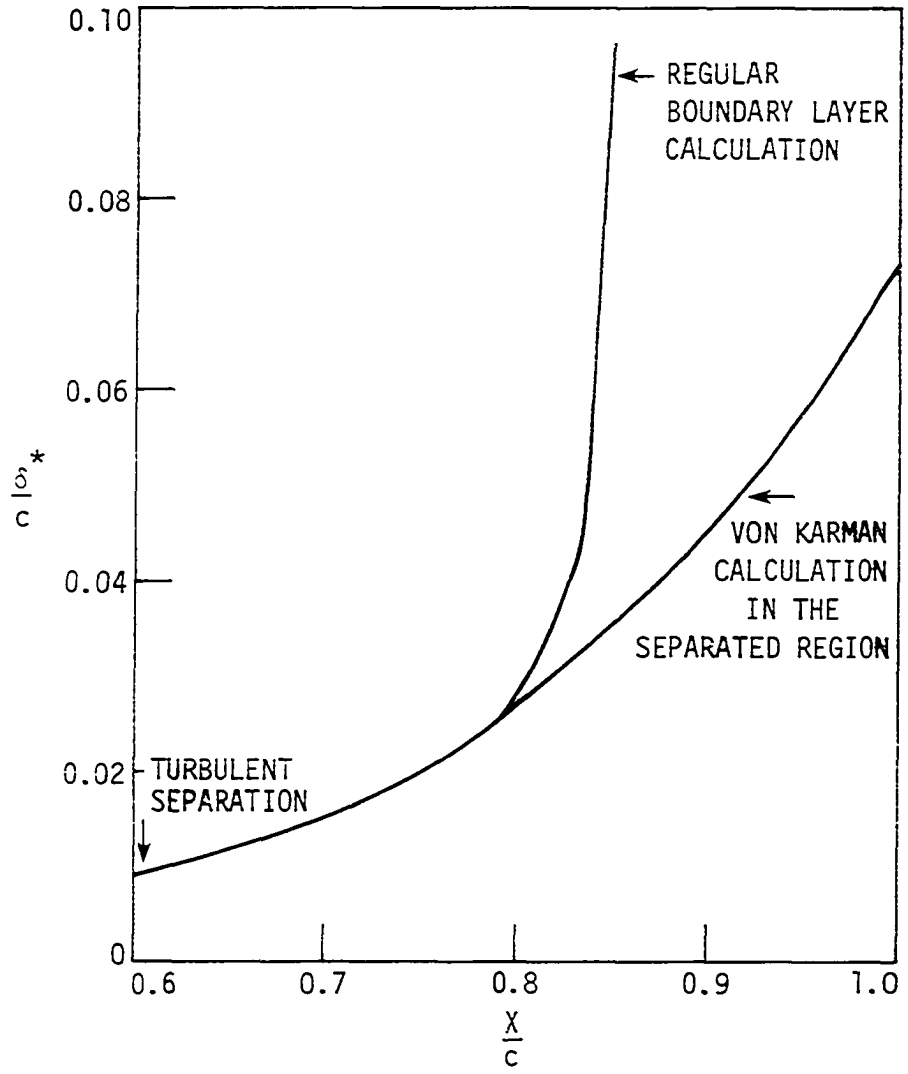

Figure 11. Continued calculation in the separated region after the failure of the normal boundary layer calculation scheme on the suction surface of a 65-(12)10 blade corresponding to the calculation point $\alpha = 20.7^{o}$ in Figure 28.

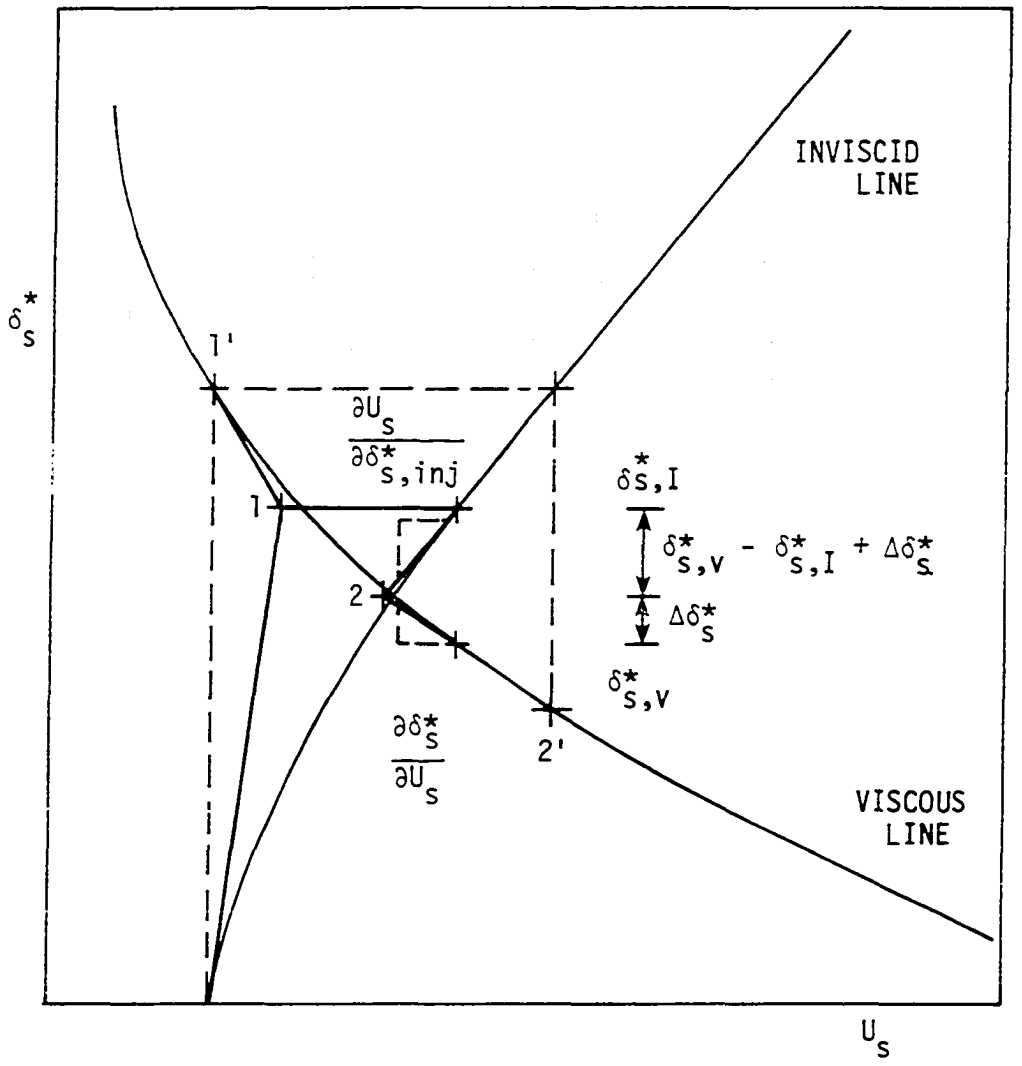

Figure 12. Interaction between the suction surface viscous velocity and boundary layer displacement thickness at the trailing edge.

viscous line, which shows how the displacement thickness changes with a change in velocity in the viscous solution. The full boundary layer added method is shown by the primed numbers and the dashed line, while the present method is shown by the unprimed numbers and solid lines. The first produces very slow convergence and may at times be divergent while the second, which shows the idea behind the method of Brune et al. (1974), converges more rapidly. Because Brune et al. used the simple test case of a flat plate in laminar flow, they were able to obtain the necessary slopes to construct a diagram similar to Figure 12 at all the calculation points along the plate. The present test cases are considerably more complex and the governing equations do not lend themselves to the simple formulations of Brune et al. It was then decided that in the present interaction one diagram similar to Figure 12 corresponding to the trailing edge point would be used. This assumes that if the injected and calculated displacement thicknesses were then matched at the trailing edge, the injected and calculated displacement thicknesses along the entire blade will match.

In the present model, Figure 12 is supplemented by Figure 13a, which is used to determine the outlet angle, $\beta_{o,I}$, by setting the suction and pressure viscous surface velocities equal. Combining Figure 12 and Figure 13a, one obtains Figure 13b, which shows how the injected and the calculated boundary layers are set equal (the intersection of the viscous and inviscid lines) and how the suction and pressure surface velocities are set equal (by changing $\beta_{o,I}$ until U_s is equal to U_p).

Figure 14 shows an overall flow chart for the computer program of the

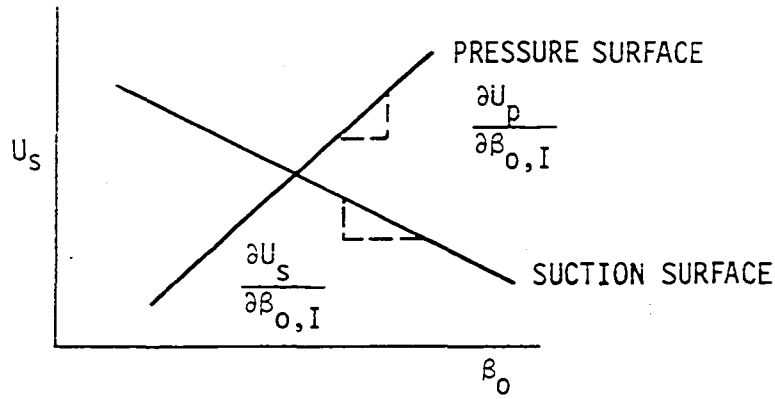

a) Relationship between the viscous velocities and the outlet angle at the trailing edge.

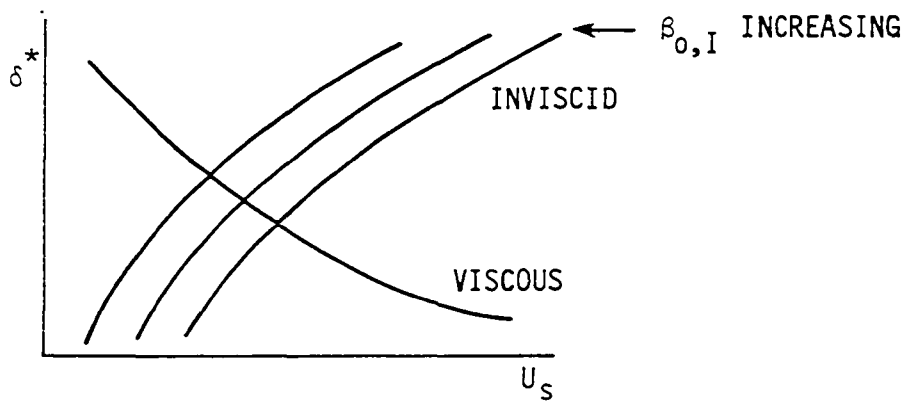

b) Interaction between the suction surface viscous velocity and boundary layer and the outlet angle.

Figure 13. Development of the interaction between the suction surface viscous velocity and boundary layer displacement thickness and the outlet angle at the trailing edge.

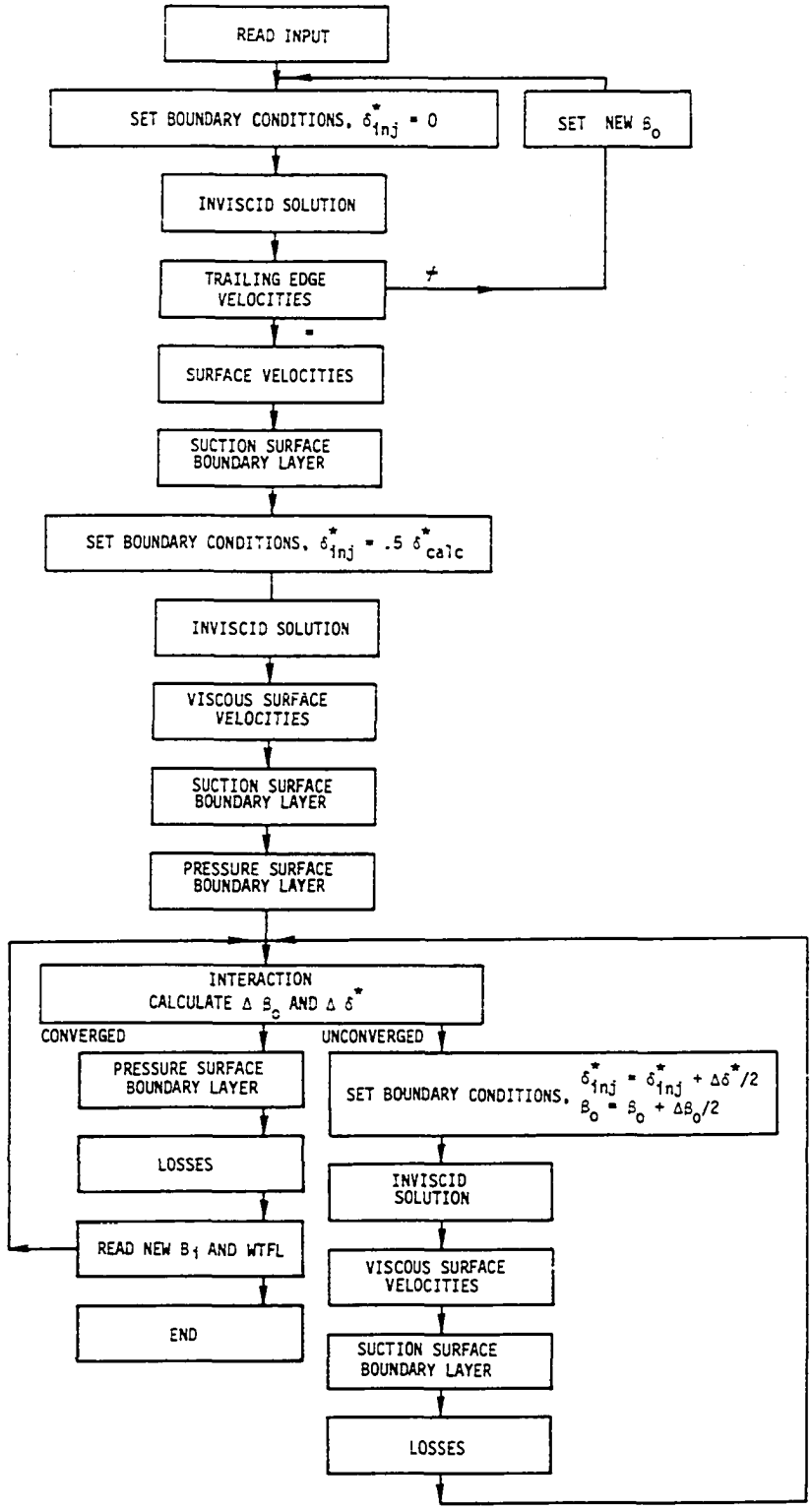

Figure 14. Flow chart of the computer program used in the present model.

present model. The general method will first be discussed as a whole, then the specifics of the method and the equations of the interaction will be discussed.

First, the input which describes the test case is read in. Then the inviscid flow over a bare blade with the guessed outlet angle is calculated and the first estimate of the outlet angle is obtained by varying the outlet angle until the pressures on the suction and pressure surface are approximately equal at the trailing edge. Next, the suction surface velocities are used as input for the boundary layer calculation. Then one-half of the suction surface boundary layer displacement thickness is injected along the suction surface in the inviscid solution and the suction surface and pressure surface velocities are obtained followed by the boundary layers. At this point the interaction loop is entered and changes in the injected suction surface displacement thickness and the outlet angle are calculated. The new displacement thickness distribution is then injected along the suction surface and the most recent pressure surface displacement thickness is injected along the pressure surface to obtain the inviscid solution and the surface pressures. This cycle, injection, calculation of the inviscid flow, calculation of the suction surface boundary layer, and injection of a better estimate of the suction surface displacement thickness proceeds until convergence or eight iterations. Then the pressure surface boundary layer is calculated using the most recent pressure surface velocity distribution. Finally, if additional cases with the same geometry are to be run they are read in and the solution from the previous case is used as the starting solution for

the new case. This discussion has given an overall view of the interaction. Next, individual components of the interaction calculation will be described.

Trailing edge closure condition

As mentioned previously, some criterion is needed to determine the outlet angle. Experimental data has proven to be very helpful in resolving this problem. Preston and Sweeting (1943) show in Figure 15 the distribution of pressure along a line normal to the chord at the trailing edge of a Joukowski airfoil for various incidence angles. In all cases there is a definite pressure rise through the viscous layer on the suction surface and the magnitude of the pressure rise is as high as 0.05 of the free stream dynamic pressure. Oliver (1976), in Figure 16, shows the normalized velocity measurements behind a stationary C4 blade in a compressor. The freestream velocities on the two sides of the blade differ by about 10%. This also shows that there is a pressure change across the viscous layer. On the basis of these data, it appears that the static pressure through the viscous layer at the trailing edge is continuous and that the pressures at the edge of the boundary layers on the pressure and suction surfaces are not in general equal. The condition of equal viscous pressures at the trailing edge on the suction and pressure surfaces will be used to determine the outlet angle.

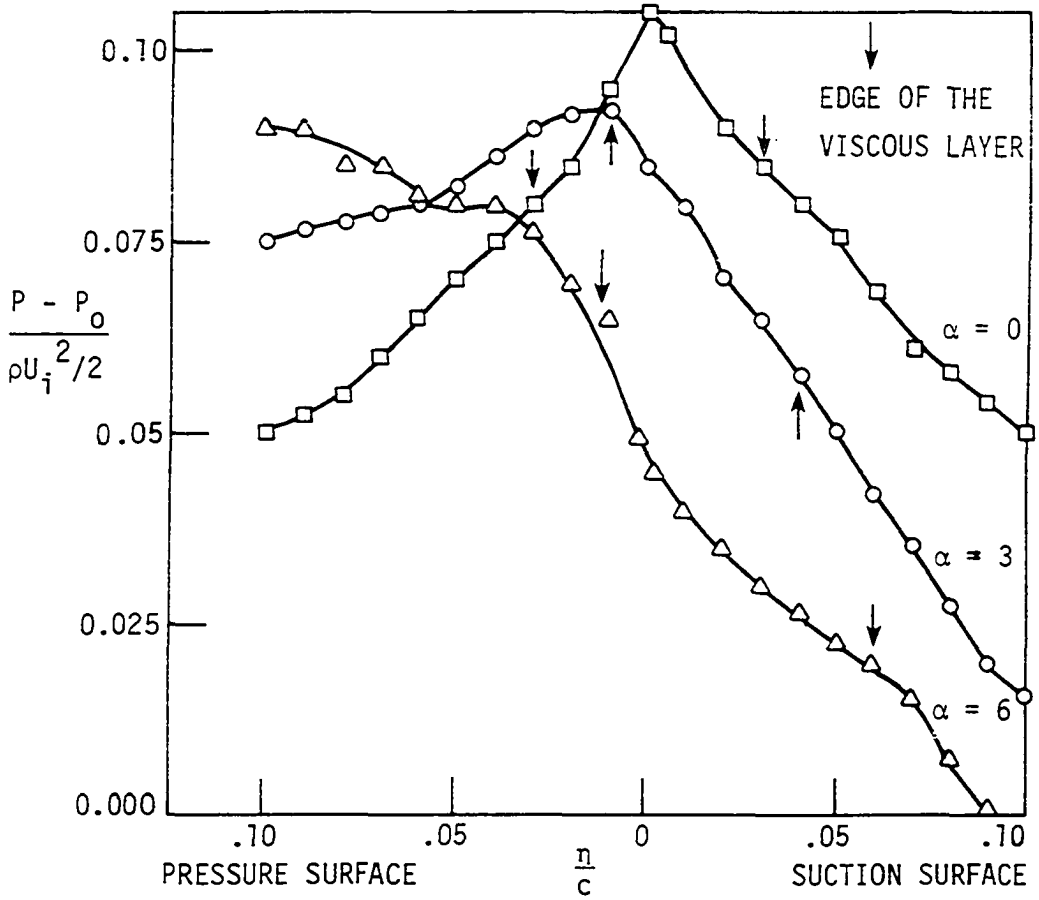

Figure 15. Pressure distributions normal to the flow at the trailing edge of a simple Joukowski airfoil for several incidence angles from Preston and Sweeting (1943).

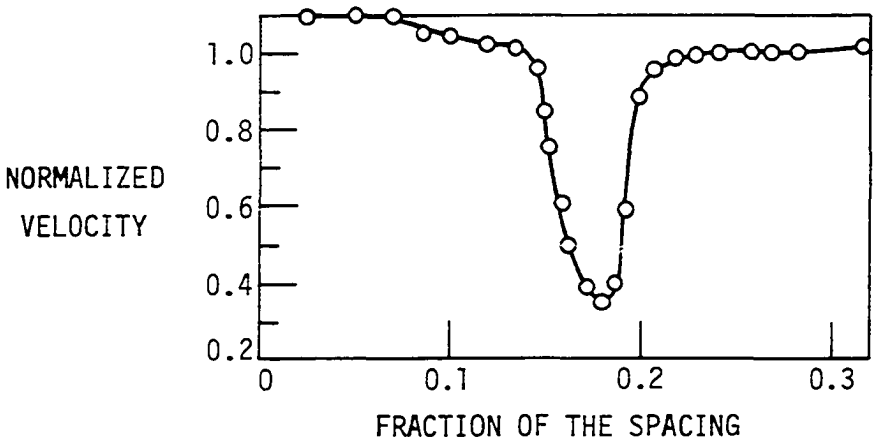

Figure 16. Velocity distribution 0.04 chord downstream of a C4 blade in the inlet guide vane of a compressor in the circumferential direction after Oliver (1976) where $Re_c = 10^5$, $\sigma = 1.0$.

Viscous surface pressures

The previously seen pressure gradient across the viscous layer normal to the streamlines indicates that the streamlines in the viscous layer are curved. Spence (1954) recognized this and calculated an estimate of the pressure change through the viscous region using the streamline curvature of the inviscid flow field and the viscous velocity distribution of the boundary layer solution. Then knowing the pressure change through the boundary layers, the pressures at the edge of the suction surface and pressure surface boundary layers can be set to differ by that calculated pressure change. Wattendorf (1935) showed that $\frac{dp}{dr} = \frac{\rho u^2}{r}$ could be used to calculate the pressure along the normal to streamlines if u and r are known. Goldstein (1938) suggested that over a curved surface the boundary layer equations in two dimensions are

$$\frac{\partial u}{\partial s} + \frac{\partial u}{\partial y} = 0 \tag{19}$$

$$u \frac{\partial u}{\partial s} + v \frac{\partial u}{\partial y} = - \frac{1}{\rho} \frac{\partial p}{\partial s} + \nu \frac{\partial^2 u}{\partial y^2} \tag{20}$$

$$-\kappa u^2 = - \frac{1}{\rho} \frac{\partial p}{\partial y} \tag{21}$$

These are the normal boundary layer equations (turbulent flow can also be considered by adding the Reynolds stress term to the laminar shear term as in Equation 5) except that Equation 19 is new. Equation 21 is the same as the equation used by Wattendorf (1935) in his curved channel experiments and Spence (1954) in his analytical calculations. Therefore

in the present computations, the change in pressure from the edge of the boundary layer to the surface (along the blade on both suction and pressure surfaces) was calculated using Equation 21. The values of u^2 and ρ are known from the boundary layer solution. However κ, the curvature of the streamlines, is obtained in a manner similar to Spence (1954), from the streamline curvature of the inviscid flow. However, in the present computations, the curvature of the inviscid streamlines at the edge of the boundary layer is considered to be the curvature of the streamlines in the boundary layer and is considered to be constant through the boundary layer. Therefore the surface pressure is obtained by finding the static pressure and the streamline curvature at the edge of the boundary layer, then integrating Equation 21 from the edge to the surface knowing the velocity distribution in the boundary layer, and finally converting that pressure into an equivalent velocity (knowing the total pressure and assuming isentropic flow), U, which is called the viscous surface velocity and was used as input to the boundary layer program. This method of obtaining surface pressures was used not only for the trailing edge point, but also for all points on the rear one-half of the blade surface.

Figure 17 shows part of a blade in the inviscid computational mesh. The surface pressures are calculated at the points where the blade surface and the vertical mesh lines intersect, for example, at point A, Figure 17. Initially a line is extended normal to the surface at A a distance of δ to B where $\delta = \delta^*(H+1)/(H-1)$ is used to obtain δ from δ^*

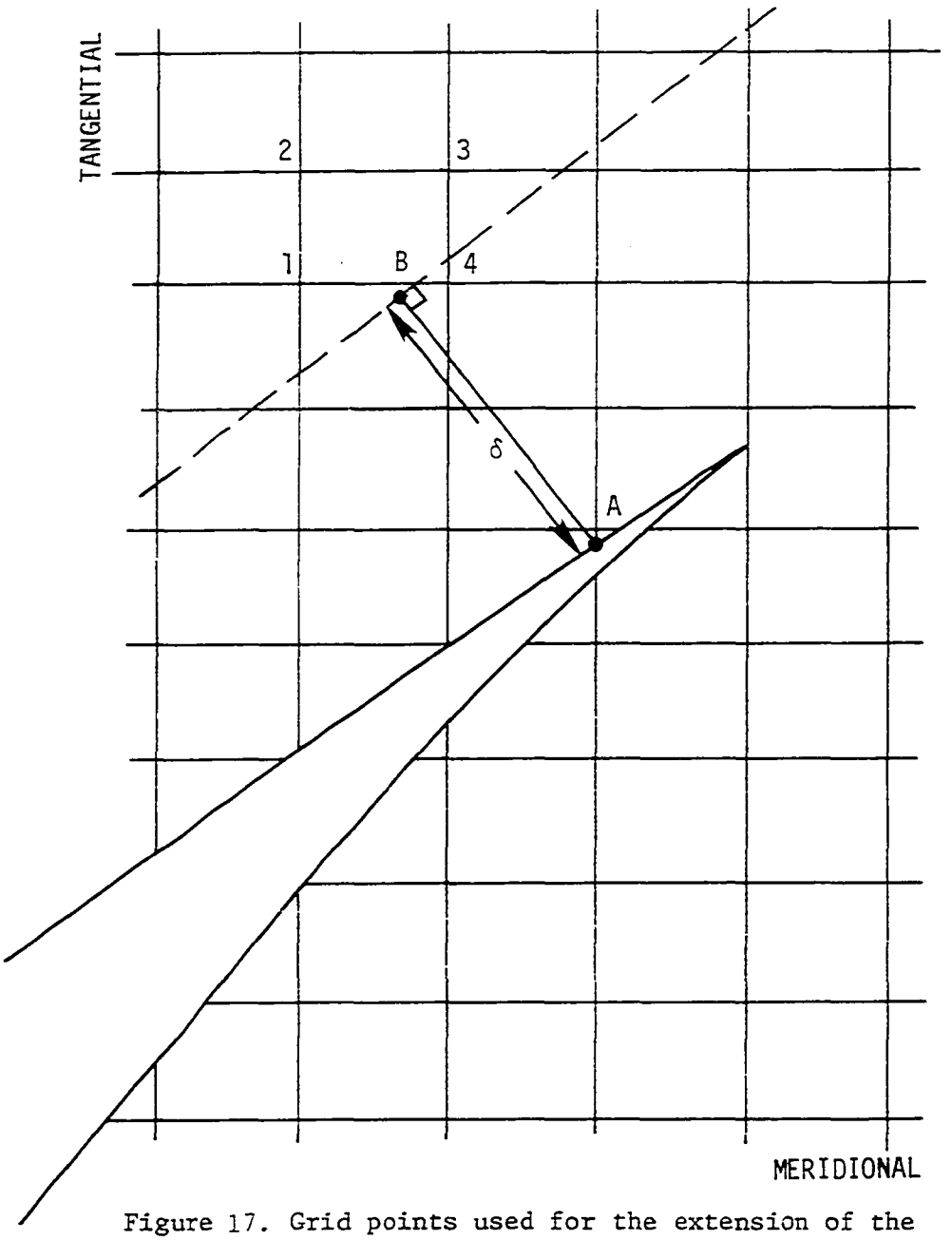

Figure 17. Grid points used for the extension of the pressure to the surface.

and H (Appendix C). Then keeping δ fixed the direction of the streamline at B is obtained from the inviscid solution, a new angle for the line AB is obtained, normal to that streamline, and the position of B is changed until AB is normal to the streamline at B. When the point B is known, the velocities at the four mesh points immediately beyond B, away from the blade, are linearly extrapolated to obtain the velocity (also the pressure) at point B (Appendix C). Then the streamline curvature is obtained using velocity derivatives in the direction normal to the streamlines (Appendix C). Finally, Equation 19 is integrated across the boundary layer to obtain the difference in pressure across the boundary layer and the surface pressure is used to obtain a viscous surface velocity (Appendix C). Therefore knowing the inviscid solution and the boundary layer solution (δ^* and H), the surface pressures and viscous surface velocities can be obtained for use in the boundary layer calculation and the matching of the pressures on the surface at the trailing edge to fix the outlet angle.

Outlet angle iteration

While investigating the method of setting the trailing edge surface pressures equal to obtain an outlet angle, Figure 18 was obtained. The figure is the result of increasing the inviscid outlet angle $\beta_{o,I}$ (the downstream boundary condition) and then decreasing it (as shown by the arrows). $U_s - U_p$ is the difference between the viscous suction surface trailing edge velocity and the viscous pressure surface trailing edge velocity. Figure 18 shows that if $\beta_{o,I}$ is continuously increased (or

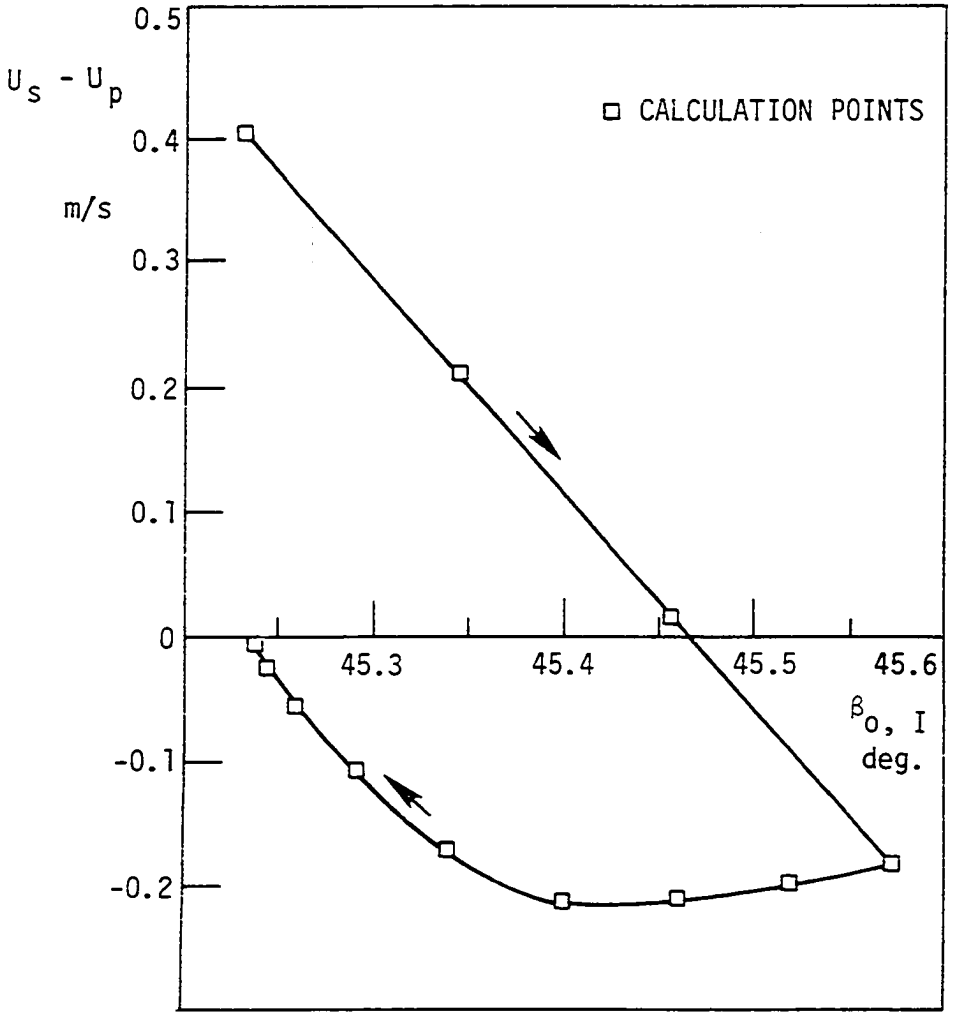

Figure 18. Hysteresis in the velocities at the trailing edge as the outlet angle is increased then decreased in the inviscid solution for the 65-410 blade cascade with no surface injection. $\gamma = 45^{o}$, $\sigma = 0.78$, $M_1 = 0.1$, $\alpha = 9.3^{o}$, $c = 124$ mm.

decreased) and the most recent ρ's and ψ's are used as a starting point for the next $\beta_{o,I}$ solution, the relationship of $U_s - U_p$ to $\beta_{o,I}$ is basically linear and when the increment of $\beta_{o,I}$ changes direction (point A), a hysteresis loop appears. This is probably caused by incomplete matching of the stream function solution with the exact answer, though it did converge within the specified tolerances. The offset of the two lines is about 0.23 degrees and may cause problems when trying to exactly converge on a solution for the outlet angle.

Simultaneous displacement thickness and outlet angle iterations

The equations used to obtain a matched solution of the trailing edge values of the injected displacement thickness and of the displacement thickness which was calculated from the boundary layer computations and equal pressures at the trailing edge are shown as follows.

$$\Delta\delta_s^* = \frac{\partial\delta_s^*}{\partial U_s}\Delta U_s \tag{22}$$

$$\Delta u_s = \frac{\partial U_s}{\partial\beta_{o,I}}\Delta\beta_{o,I} + \frac{\partial U_s}{\partial\delta_s^*}(\delta_{s,v}^* - \delta_{s,I}^* + \Delta\delta_s^*) \tag{23}$$

$$\Delta u_p = \frac{\partial U_p}{\partial\beta_{o,I}}\Delta\beta_{o,I} + \frac{\partial U_p}{\partial\delta_s^*}(\delta_{s,v}^* - \delta_{s,I}^* + \Delta\delta_s^*) \tag{24}$$

$$U_p + \Delta U_p = U_s + \Delta U_s \tag{25}$$

This system of four equations has four unknowns, $\Delta\delta_s^*$, ΔU_s, ΔU_p, and $\Delta\beta_{o,I}$. The variables $\delta_{s,v}^*$, $\delta_{s,I}^*$, U_p, and U_s are readily obtained at the trailing edge from the latest inviscid and viscous calculations as shown in Figure 12. $\delta_{s,v}^*$ is the value of the suction surface displacement thickness at

the trailing edge calculated from the boundary layer equations. $\delta^*_{s,I}$ is the value of the suction surface displacement thickness at the trailing edge used to calculate the injection on the blade. $\delta^*_{s,v} - \delta^*_{s,I} + \Delta\delta^*_s$ is the change in the injected displacement thickness and $\Delta\beta_{o,I}$ is the change in the inviscid outlet angle. U_p and U_s are the pressure and suction surface viscous velocities.

The derivatives, $\frac{\partial U_s}{\partial \beta_{o,I}}$ and $\frac{\partial U_p}{\partial \beta_{o,I}}$, shown in Figure 13a, are calculated within the subroutine which solves for the initial estimate of $\beta_{o,I}$ by setting U_s and U_p equal. The input value of $\beta_{o,I}$[1] is incremented by 0.1146 degrees (0.002 radians) four times in the direction of $U_s - U_p = 0$, as shown in Figure 19, points 1-5. Then using the average slope from 3-4-5 and the value of $U_s - U_p$ at 5 the $\beta_{o,I}$ for $U_s - U_p = 0$ is estimated, 6. At the same time that $\beta_{o,I}$ is being converged upon, $\frac{\partial U_s}{\partial \beta_{o,I}}$ and $\frac{\partial U_p}{\partial \beta_{o,I}}$ are calculated as an average using points 3-5 and are finally normalized by dividing by the corresponding suction or pressure surface velocity so that this slope can be used at any outlet velocity level.

After the outlet angle is initially set and the surface pressure calculated, the suction surface boundary layer is calculated and 1/2 of the boundary layer displacement thickness is injected. The change in the suction surface trailing edge viscous velocity produced by this injection

[1] The input value of $\beta_{o,I}$ needs to be a reasonable value but may still be 5 to 7 degrees away from the initial calculated value of $\beta_{o,I}$. If the input $\beta_{o,I}$ is in error more than 5 degrees, it is suggested that the initial $\beta_{o,I}$ calculation should be carried out (which is presently being described), and that initial calculated value of $\beta_{o,I}$ be used as the input value to insure a good estimate of $\frac{\partial U_s}{\partial \beta_{o,I}}$ and $\frac{\partial U_p}{\partial \beta_{o,I}}$.

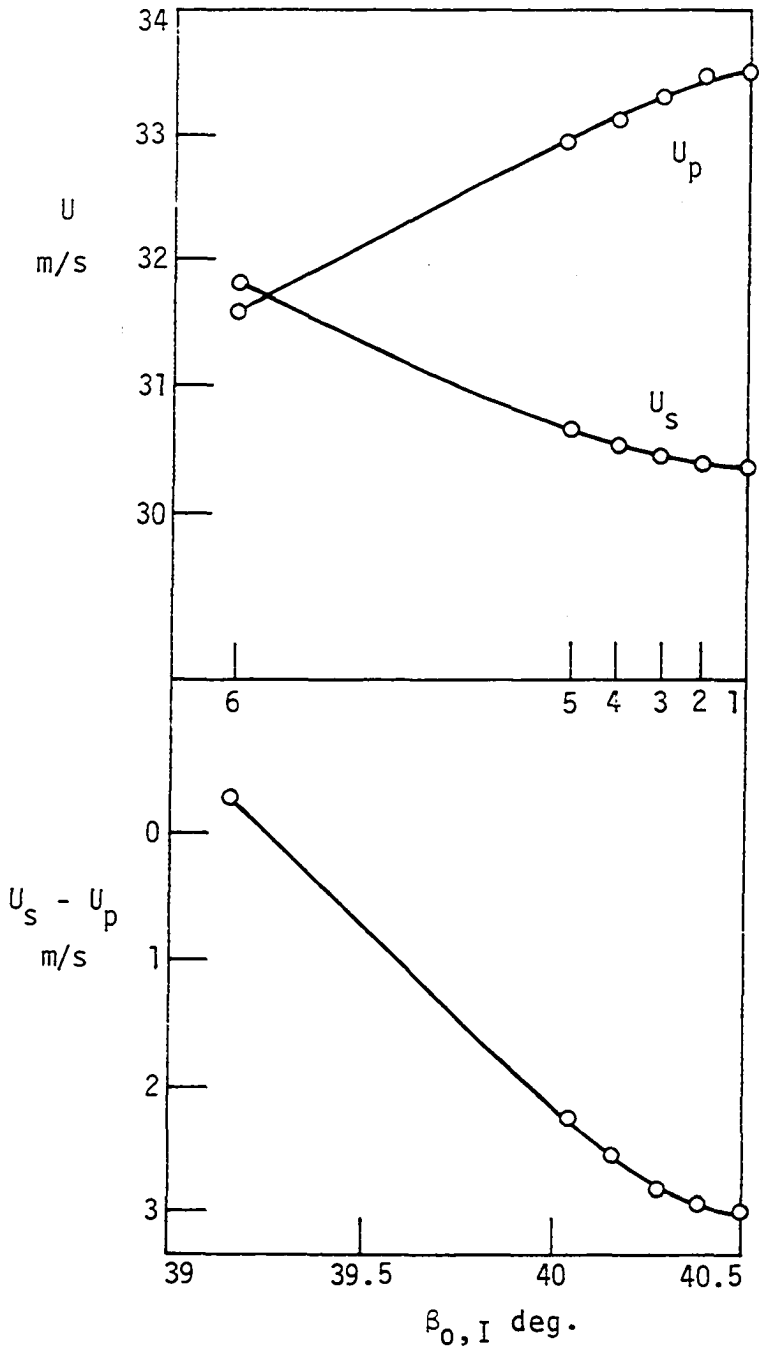

Figure 19. Iterations during the initial calculation of $\beta_{o,I}$ for the 65-(12)10 blade cascade calculation in Figure 30 as U_s-U_p is set nearly equal to zero.

is used to calculate $\frac{\partial U_s}{\partial \delta^*_s}$ (Figure 12), which is also normalized by U_s. The term $\frac{\partial U_p}{\partial \delta^*_s}$ in Equation 24 was considered to be unimportant and was set equal to zero.

Finally, $\frac{\partial \delta^*_s}{\partial U_s}$ (Figure 12), the ratio of the change of the displacement thickness with a change in input velocity is calculated knowing $U_s(s)$ and $\delta^*_s(s)$, the boundary layer input and output. Normally as shown in Figure 20, the boundary layer calculation proceeds from points A to B, obtaining δ^* and θ from an input U_s. However, suppose one were to proceed from A to C, in a case where U_s remains constant, $\frac{dU_s}{ds} = 0$, and the boundary layer is near separation, $\tau_w \simeq 0$. The Von Karman integral equation, $\frac{d\theta}{ds} + (2\theta+\delta^*)\frac{1}{U}\frac{dU}{ds} = \frac{\tau_w}{\rho U^2}$, becomes $\frac{d\theta}{ds} = 0$, so that $\theta_A = \theta_C$. If H_A is assumed equal to H_C, $\frac{\delta^*_A}{\partial \delta^*} = \delta^*_C$. Now, δ^*_C, U_C and δ^*_B, U_B would be known so that the derivative $\frac{\partial \delta^*_s}{\partial U_s}$ could be calculated as $\frac{\partial \delta^*_s}{\partial U_s} = \frac{\delta^*_B - \delta^*_C}{U_B - U_C}$. Because values at A are equal to those at C, they can be substituted to obtain $\frac{\partial \delta^*_s}{\partial U_s} = \frac{\delta^*_B - \delta^*_A}{U_B - U_A}$, which should be adequate if the distance from A to B is small compared to the entire chord length. In some cases where $\frac{dU_s}{ds}$ is small, $\frac{\partial \delta^*_s}{\partial U_s}$ may be positive. This is not acceptable or realistic as seen in Figure 12. If the viscous and inviscid lines do not have slopes of different sign (i.e., a negative slope for the viscous line and a positive slope for the inviscid line) then the intersection of these lines will not be realistic. When $\frac{\partial \delta^*_s}{\partial U_s}$ is positive, Equation 22 is not used. $\Delta\delta^*_s$ is calculated as one-half the difference between the latest calculated and latest injected displacement thickness, and the remaining set of equations are solved for $\Delta\beta_{o,I}$ knowing this $\Delta\delta^*_s$.

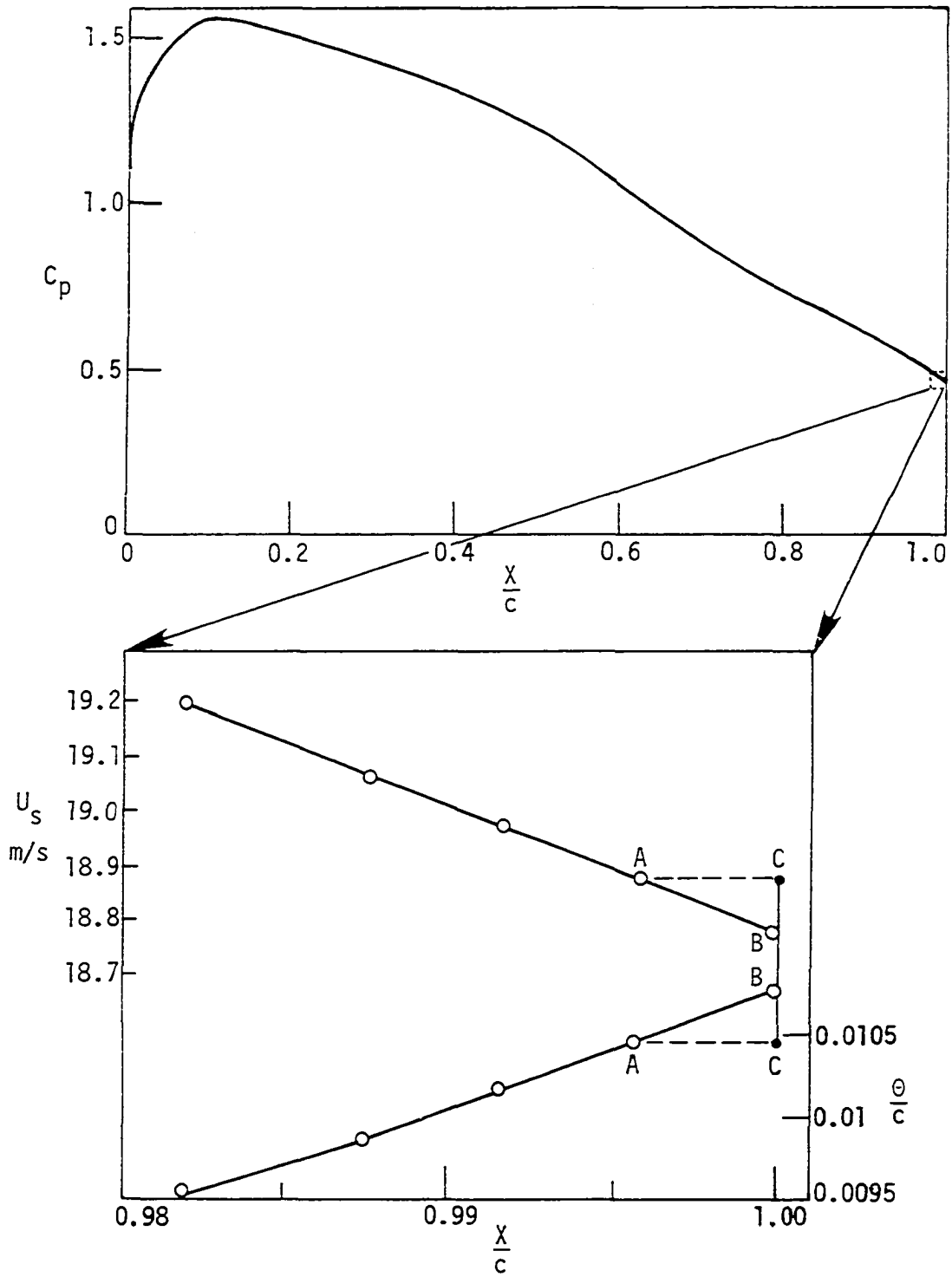

Figure 20. Modified velocity and boundary layer diagrams used to calculate $\partial\delta_s^*/\partial U$ from an intermediate calculation for the 65-(12)10 blade cascade calculation corresponding to the point $\alpha = 14.2^\circ$ in Figure 28.

The result of the interaction calculation is a value for $\Delta\delta^*$ and $\Delta\beta_{0,I}$. The new injection and outlet angle are calculated from the previous values by adding one-half of this predicted change, thus introducing some damping. The new injected displacement thickness distribution is calculated as

$$\delta^* = (0.6\ \delta^*_{(1)}\ \frac{\delta^*_{(2)te}}{\delta^*_{(1)te}} + 0.4\ \delta^*_{(2)})(1 + (\frac{\delta^*_{(3)te}}{\delta^*_{(2)te}} - 1)(\frac{x}{x_{te}})^2) \quad . \qquad (26)$$

$\delta^*_{(1)}$ is the previous injected displacement thickness distribution and $\delta^*_{(2)}$ is the newly calculated displacement thickness distribution. $\delta^*_{(1)te}$ and $\delta^*_{(2)te}$ are the respective trailing edge values and $\delta^*_{(3)te}$ is the new trailing edge displacement thickness injection level just calculated from $\Delta\delta^*_s$. The first term of this formulation stabilizes the distribution of δ^* by making the new variation correspond to a weighted average of 0.4 the most recent δ^* from the boundary layer calculation and 0.6 the most recently injected δ^*. The second term allows the displacement thickness to vary considerably in the trailing edge region without affecting the boundary layer near the leading edge of the blade which does remain fairly constant from iteration to iteration.

Calculation of losses

Downstream of the trailing edge it is desirable to know the total pressure loss and the downstream flow angle. Knowing the boundary layer parameters at the trailing edge on the suction and pressure surface and the downstream outlet angle in the inviscid calculation and using the methods of Lieblein and Roudebush (1956) for incompressible flow and

Stewart (1955) for compressible flow one can calculate the total pressure loss coefficient and the outlet angle for complete mixing. To obtain the experimentally measured loss parameter C_w, where $C_w = 2\theta_s \cos^2\beta_i/\cos^3\beta_o/c$, θ must be known as a function of s downstream of the trailing edge. For wake flow, $\tau_w = 0$ and the Von Karman integral equation becomes $\frac{d\theta}{ds} + (2+H)\frac{\theta}{U}\frac{dU}{ds} = 0$. Then using a correlation for the variation of H in the streamwise direction and the conservation of mass, θ can be obtained as a function of s and C_w calculated (Appendix D).

SELECTION OF EXPERIMENTAL CASCADE DATA FOR TEST CASE COMPUTATION

In the past 30 years a large number of airfoil cascade tests have been run. Because many were to obtain data on a particular phenomenon, the measurements were taken only in the areas of interest and the rest of the flow field was not investigated. This means that there are data on many specific phenomena, but there is a lack of data describing the entire flow field. Criteria for the acceptability of cascade data for this research will then be presented and useful data will be selected on this basis. Mention will also be made of flow field quantities which, if measured, would greatly benefit cascade flow computation in the future.

The necessary measured parameters in cascade flow are of two types, independent and dependent. Acceptable cascade data for the present work includes measurements of the following dependent and independent quantities. The independent quantities include the inlet mach number, inlet Reynolds number, inlet air angle, inlet turbulence, the fluid, the geometry of the blade-to-blade passage and the value of the local-to-inlet axial velocity density ratio through the cascade. The necessary dependent or measured quantities include a turning or outlet angle, a measure of total pressure loss, and the pressure distribution on the blade surfaces. In addition there are certain quantities, not usually measured, which would be of great value in cascade flow computation development. These are as follows. The values of the boundary layer

displacement and momentum thicknesses along the blade surface are essential. Regions along the blade of particular interest are the leading edge (so that good starting conditions can be used for the boundary layer calculation), the regions of transition or laminar separation (so that these may be modeled accurately), the regions of turbulent separation, the region near the trailing edge, and the wake. The area of the trailing edge is important because the pressure distribution in this region determines the outlet flow angle and measurements of static pressure and velocity (flow magnitude and direction) in this region would be of much help in modeling the trailing edge flow which is at present a large obstacle to accurate cascade modeling.

Although the present model is able to calculate cases with axial velocity density ratios other than one[1], it was felt that two-dimensional test cases would be best because they would probably point to the sources of flaws in the modeling and because the majority of the data for which the axial velocity-density product was controlled were two-dimensional. The acceptable data from which test cases were selected are given in Table 3. From Table 3 three blade sections, 65-410, 65-(12)10, and 65-($12A_2I_{8b}$) were chosen. The 65-410 blade section was selected because in addition to the data of Herrig et al. (1957), data from Peterson (1958) provided boundary layer information at three angles of

[1]The Katsanis and McNally (1969) program includes the useful feature of being able to vary the axial velocity-density product and the axially symmetric stream surface radius as functions of the meridional distance through the cascade.

Table 3. Two-dimensional cascade data

Reference	$Re_c \times 10^{-5}$	M_1	Blade Type
Briggs (1952) NACA TN 2649	3-10.4	.12-.89	65-(12)10
Dunavant, Emery, Walch, and Westphal (1955) NACA RM L55I08	5.5	.3-.8	65-($12A_{10}$)10 65-($12A_2I_{8b}$)10
Erwin, Savage and Emery (1956) NACA TN 3817	4.4	.156	65-($4A_2I_{8b}$)10 65-($8A_2I_{8b}$)10 65-($12A_2I_{8b}$)10 65-($18A_2I_{8b}$)10
	3.46	.156	65-($12A_6I_{4b}$)10 65-($12A_6I_4$)10
	1.5-5.3	-.1	65-($12A_2I_{8b}$)10
Emery and Dunavant (1957) NACA RM L57H05	-	.3-.7	65-($12A_{10}$)10 65-($15A_{10}$)10 65-($18A_{10}$)10 65-($21A_{10}$)10 DCA
Felix and Emery (1957) NACA TN 3937	2.3	-.1	65-($12A_{10}$)10 10C4/30C50
Herrig, Emery, and Erwin (1957) NACA TN 3916	2.45	-.1	65-010 65-410 65-810 65-(12)10 65-(15)10 65-(18)10 65-(21)10 65-(24)10 65-(27)10
	1.6-4.8	-.1	65-(12)10
Speidel and Scholz (1957) VDI-Forsch. 464	5.0	.12	0010 8410

$\frac{c}{s}$	β_i	AVDR	Parameters Measured			
			$\Delta\beta$	Loss	C_p	Boundary Layer
1.0	45	1	Y	Y	Y	N
1.0 1.5	45 60	1	Y	Y	Y	N
1.0 1.5	30 45 60	1	Y	Y	Y	N
1.0 1.5	45 60	1	Y	Y	Y	N
1.0	60	1	Y	Y	N	N
1.5 1.25	25 35 45	1	Y	Y	Y	N
1.0	30 45 60	1	Y	Y	Y	N
.5 .75 1.0 1.25 1.50	30 45 60 70	1	Y	Y	Y	N
1.0 1.5	45,60	1	Y	Y	N	N
2.0 1.33 1.0 .8	$\pm$30 $\pm$60 90	1	Y	Y	Y	N

Table 3 (Continued)

Reference	$Re_c \times 10^{-5}$	M_1	Blade Type
Dunavant and Emery (1958) NACA RM L58A02	5.-1.7	.3-1.0	65-($8A_{10}$)10 65-($4A_{10}$)06 65-($8A_{10}$)06
Milsch (1971) Germany	4.3	.11	65-610 65-(12)10 65-(12)06 65-(18)10

$\frac{c}{s}$	β_i	AVDR	Parameters Measured			
			$\Delta\beta$	Loss	C_p	Boundary Layer
.6	Constant					
.8	γ	1	Y	Y	Y	N
1.0	γ=40,50					
.75						
1.0	50	1	Y	Y	Y	N
1.25						

attack on both sides of the blade. The 65(12)10 blade was chosen because low speed and Reynolds number data were available from Herrig et al. (1957), boundary layer data were available from Milsch (1971), and high speed data were available from Dunavant et al. (1955). Finally, the 65-($12A_2I_{8b}$)10 blade was chosen because low speed and Reynolds number data were available from Erwin et al. (1956) and high speed data were available from Dunavant et al. (1955).

The cascade data previously mentioned, Herrig et al. (1957), Erwin et al. (1956) and Dunavant et al. (1955), were taken at a constant inlet angle and the angle of attack was changed by varying the stagger angle. This means that the inlet flow was held constant and the geometry of the blade passage was changed. This type of situation is very hard to simulate with the inviscid program used in the present model because blade coordinates for each new geometry must be calculated and then adjusted so as to have a smooth curvature distribution along each blade surface. Since an inordinate amount of time would be spent merely generating geometries, it was most expedient to select a stagger angle which fell in the center of the stagger angles of the experimental data and set the blade at that angle thus fixing the geometry. Then the inlet angle in the calculations would vary as the stagger varied in the experiments so that the two could be compared by angle of attack. Though there will be differences between data taken at constant stagger angle and constant inlet angle, when compared by the incidence angle, this type of comparison should be acceptable for small perturbations about a point where the stagger angle, the inlet angle, and the angle

of attack are the same. The blades selected are the 65-410, the 65-(12)10, and the 65-(12A,I_{8b})10 as shown in Figure 21. These blades were each used in one cascade configuration as follows: 65-410, γ = 45.0 degrees, σ = 0.78; 65-(12)10, γ = 45.7 degrees, σ = 1.0; and 65-($12A_2I_{8b}$)10, γ = 45.3 degrees, σ = 1.0. The calculation regions and mesh sizes for each cascade are given in Figure 22.

65-410 BLADE; γ = 45 degrees, σ = 0.78 CASCADE

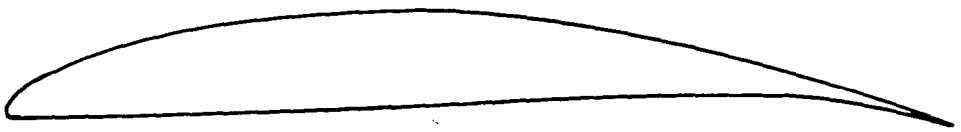

65-(12)10 BLADE; γ = 45.7 degrees, σ = 1.0 CASCADE

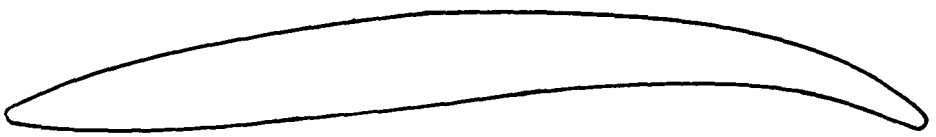

65-($12A_2I_{8b}$) 10 BLADE; γ = 45.3 degrees, σ = 1.0 CASCADE

Figure 21. The three cascades used to test the present model

65-410 CASCADE

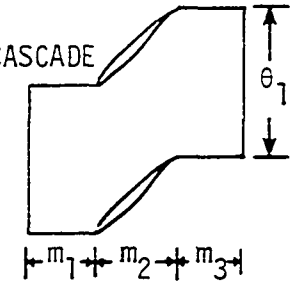

θ_1 = 35 MESH LINES
θ_1 = 0.1588 m
θ_1 = 0.5209 ft
σ = 0.78

m_1 = 20	m_2 = 25	m_3 = 20	mesh lines
m_1 = 0.07038	m_2 = 0.08797	m_3 = 0.07038	m
m_1 = 0.2309	m_2 = 0.2886	m_3 = 0.2309	ft
m_1 = 0.568	m_2 = 0.710	m_3 = 0.568	percent chord

65-(12)10 CASCADE

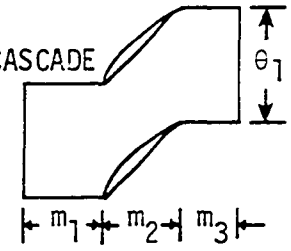

θ_1 = 35 MESH LINES
θ_1 = 0.127 m
θ_1 = 0.4066 ft
σ = 1.0

m_1 = 25	m_2 = 25	m_3 = 18	mesh lines
m_1 = 0.08739	m_2 = 0.08739	m_3 = 0.0629	m
m_1 = 0.2867	m_2 = 0.2867	m_3 = 0.2064	ft
m_1 = 0.705	m_2 = 0.705	m_3 = 0.508	percent chord

65-(12A_2I_{8b})10 CASCADE

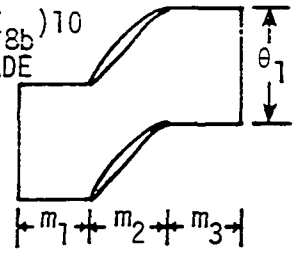

θ_1 = 25 MESH LINES
θ_1 = 0.124 m
θ_1 = 0.4066
σ = 1.0

m_1 = 30	m_2 = 25	m_3 = 25	mesh lines
m_1 = 0.1044	m_2 = 0.08702	m_3 = 0.08702	m
m_1 = 0.3426	m_2 = 0.2855	m_3 = 0.2855	ft
m_1 = 0.843	m_2 = 0.702	m_3 = 0.702	percent chord

Figure 22. The calculation regions and mesh sizes used in the TSONIC program for the three cascades tested.

DISCUSSION OF RESULTS

After determining the blade sections and their particular test conditions, calculations were made using an Univac 1100/42 computer with input as specified in Table 4. Because of the long run times for the program (one to two hours), many intermediate values were printed at each iteration to permit evaluation of the internal consistency of the program. The results of the calculations for each blade section and flow condition may be compared with the available experimental data to determine which parts of the model are producing real physical effects and which are not properly modeling the flow. General weaknesses of and possible corrections for viscous-inviscid interaction schemes and general insights into the inviscid-viscous interaction phenomenon will also be discussed.

65-410 Blade Cascade

The turning, loss and suction surface transition and separation points plotted against the inlet angle for the 65-410 blade cascade are shown in Figure 23. The two calculations (1 and 2) shown differ only by the s step size used on the last one-half of the blade. Calculation 2 uses the same step size in the boundary layer as all other calculations in this work, while calculation 1 uses a larger step size. Notice that up to $\alpha = 18°$ the two calculations show very good repeatability. The calculated turning, $\Delta\beta$, has a slope which is quite similar to the experimental data and levels off at the same place the experimental data does. This decrease in turning also occurs near the point where laminar separation and bursting occur in the model. However, the levels of turning between the experimental data and the

Table 4. Independent cascade variables for each test case

Test Case	Inlet Mach Number M_i	Inlet Reynolds Number Re_c	Angle of Attack $\alpha°$	Inlet Turbulence Intensity Tu	Axial Velocity Density Ratio
65-410 Cascade					
Low Speed	0.1	245,000	9.3°, 12.4° 15.0°, 16.0° 17.0°, 18.0° 19.0°	0.005	1.0
65-(12)10 Cascade					
Low Speed	0.15	430,000	12.5°	0.0005	1.0
	0.1	245,000	14.2°, 17.7° 19.2°, 20.7° 21.7°	0.005	1.0
Reynolds Number	<0.1	150,000 220,000 350,000	12.0°	0.005	1.0
High Speed	0.3, 0.5 0.7	8.7×10^5 2.0×10^6	14.3°	0.005	1.0
65-($12A_2I_{8b}$)10 Cascade					
Low Speed	0.1	440,000	10.6°, 12.5° 14.7°, 16.7° 18.7°	0.005	1.0
Reynolds Number	<0.1	450,000 350,000 275,000 200,000	9.6°	0.005	1.0
High Speed	0.3, 0.5, 0.7	9.0×10^5- 2.2×10^6	11°	0.005	1.0

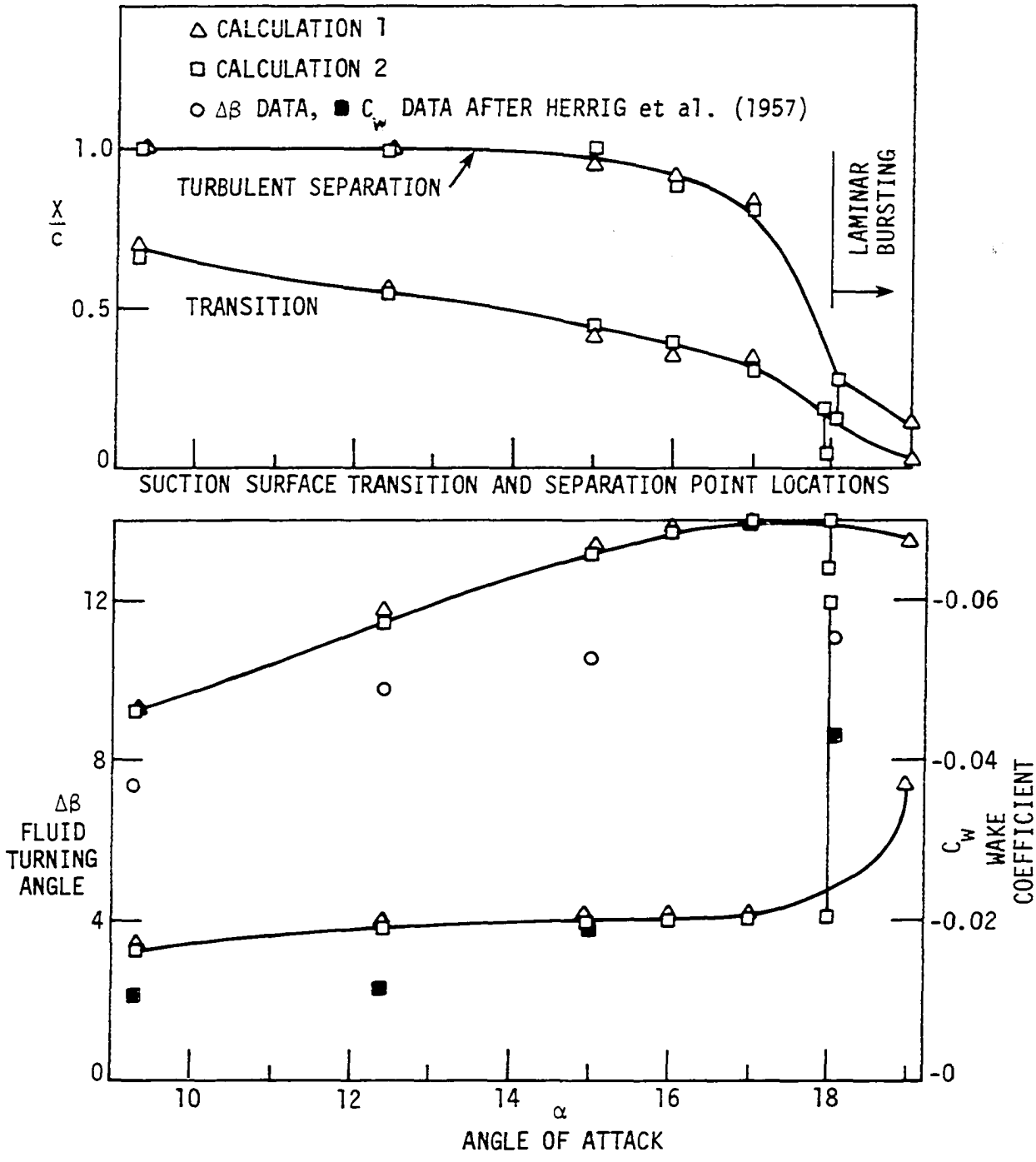

Figure 23. Calculated turning and loss compared with experimental data and calculated transition and separation points for a 65-410 blade. M_i = .1, Re_c = 245,000, γ = 45°, σ = .78, c = 124 mm.

calculation differ by about two degrees. The calculated loss coefficient is too high at low angles of attack and not high enough at high angles of attack. Although at high angles of attack the calculated and experimental loss coefficients do not match, they both show the same trend of a rapid increase with a small change in angle of attack, which occurs after the point of laminar separation and bursting. The points of transition and turbulent separation also shown drop dramatically near the point of laminar separation and bursting. This is to be expected, because as the inlet angle is increased, the pressure gradient on the suction surface gets steeper and the transition point moves forward until the gradient is so steep that laminar separation occurs. The computation time for the seven incidence cases run consecutively was 2.03 hours.

Figure 24 shows the convergence of the calculations for the 65-410 blade. All of the calculations were done so that the converged solution from the previous inlet conditions is used as the starting point of the calculation of the next inlet conditions. $U_s - U_p$ is the difference in the viscous surface velocities on the suction and pressure surfaces and indicates the degree to which the trailing edge pressures are equal. $\delta^*_{inj} - \delta^*_{calc}$ is the difference in the injected suction surface trailing edge displacement thickness and suction surface trailing edge displacement calculated from the boundary layer equations and indicates the degree to which the two displacement thicknesses are equal. Finally, $\beta_{o,I}$ is the angle at the downstream boundary of the inviscid calculation. All the calculations converged except for $\alpha = 18°$, which did not converge in 8 iterations. Observe in the $\alpha = 18°$ calculation the large oscillations in

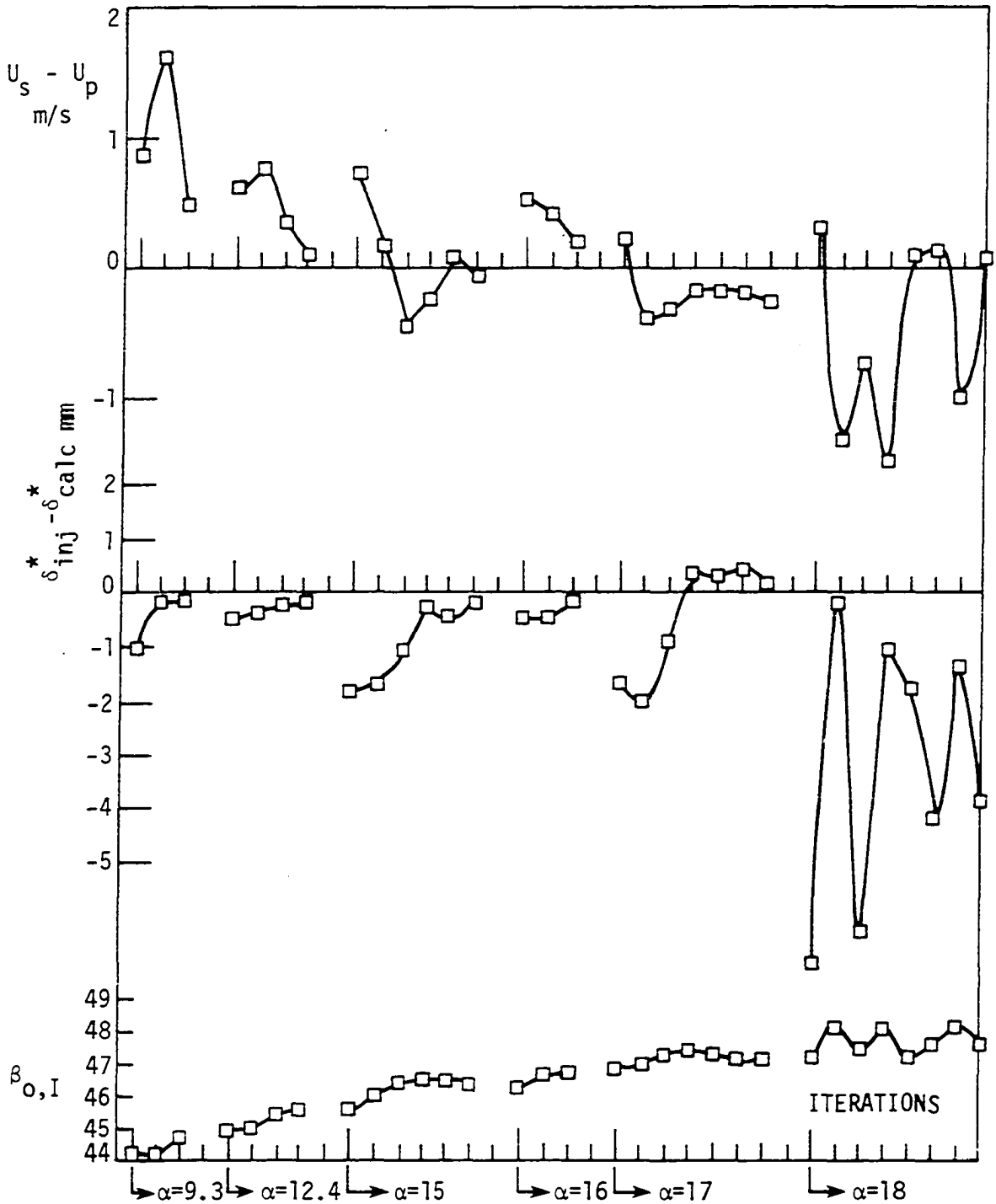

Figure 24. Convergence of the calculation for the 65-410 blade cascade.

$\delta^*_{inj}-\delta^*_{calc}$ which are caused by the boundary layer flow alternating between transition, laminar separation and laminar bursting.

The next three figures show the surface pressures and the displacement and momentum thickness on the suction and pressure surfaces for three different angles of attack. When $\alpha = 9.3°$, as shown in Figure 25, the surface pressures match well with the experimental data, the pressure surface boundary layer also shows fair agreement with experimental data, but the suction surface boundary layer shows substantial disagreement with the experimental data. The starting boundary layer could have been too thick, since δ^* and θ don't match the data at X/c = 0.2 or the velocity gradient near the trailing edge (greater than X/c = 0.8) on the suction surface could have been steeper than the actual gradient. Figure 26 shows that for $\alpha = 12.4°$ the surface pressures match well with experiment and that separation is beginning on the suction surface. Although convergence could not be obtained at $\alpha = 18°$, because the boundary layer calculation alternated between transition and laminar separation from iteration to iteration, it was obtained at $\alpha = 19°$, because laminar separation near the leading edge was calculated at each iteration. The calculation at $\alpha = 19°$ was compared with the data of Herrig et al. (1957) at $\alpha = 18.1°$ and Peterson (1958) at $\alpha = 20°$ in Figure 27. Though the suction surface pressure peak seems to match, the surface pressure near the trailing edge are quite different from the experimental data. The suction surface boundary layer seems to match fairly well though the momentum thickness is a little low and the displacement thickness is high. It is also seen that the flow underwent

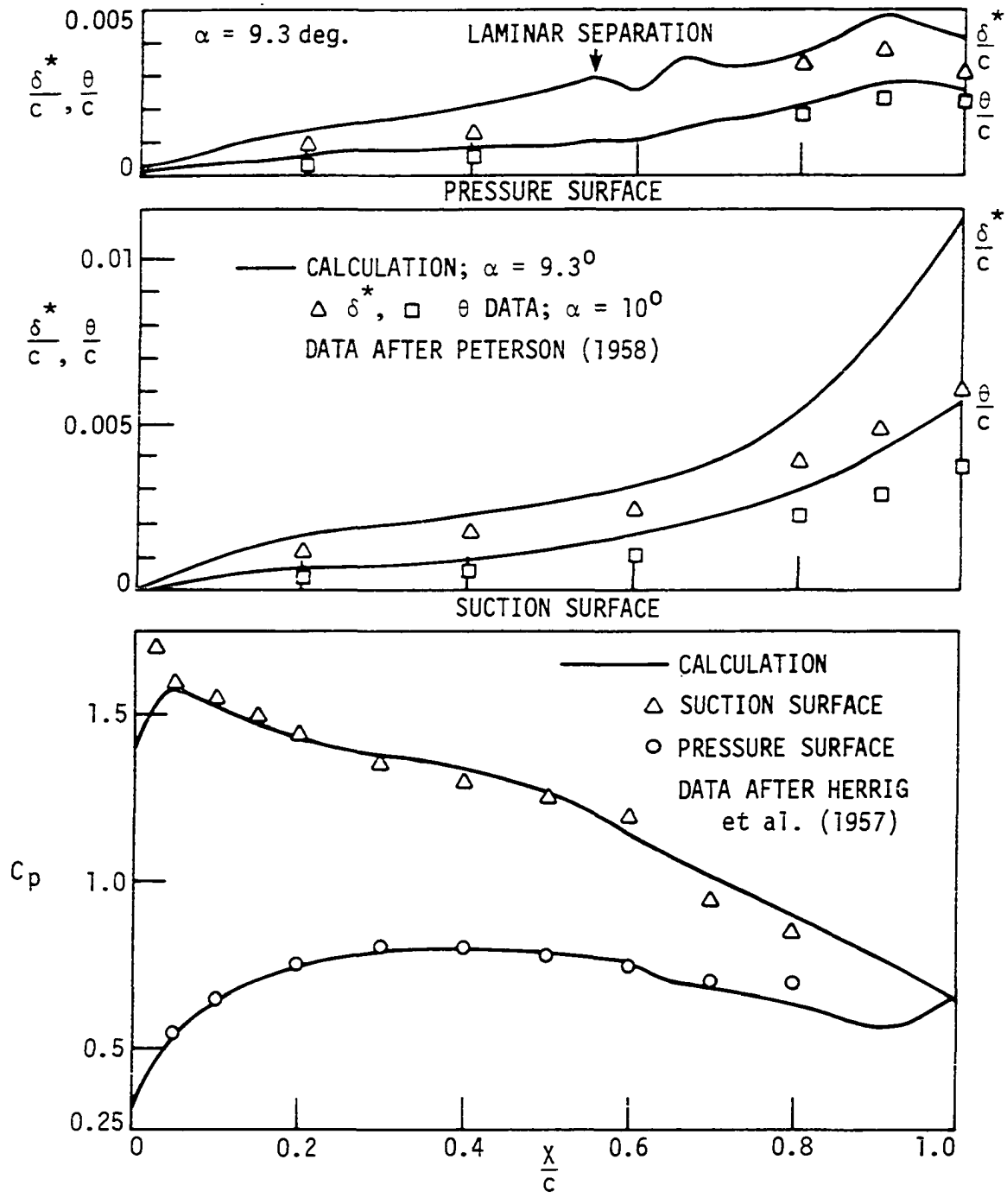

Figure 25. Calculated surface pressure compared with experimental data and calculated suction and pressure surface boundary layers. 65-410 blade, M_i = .1, Re_c = 245,000, γ = 45°, σ = .78, c = 124 mm.

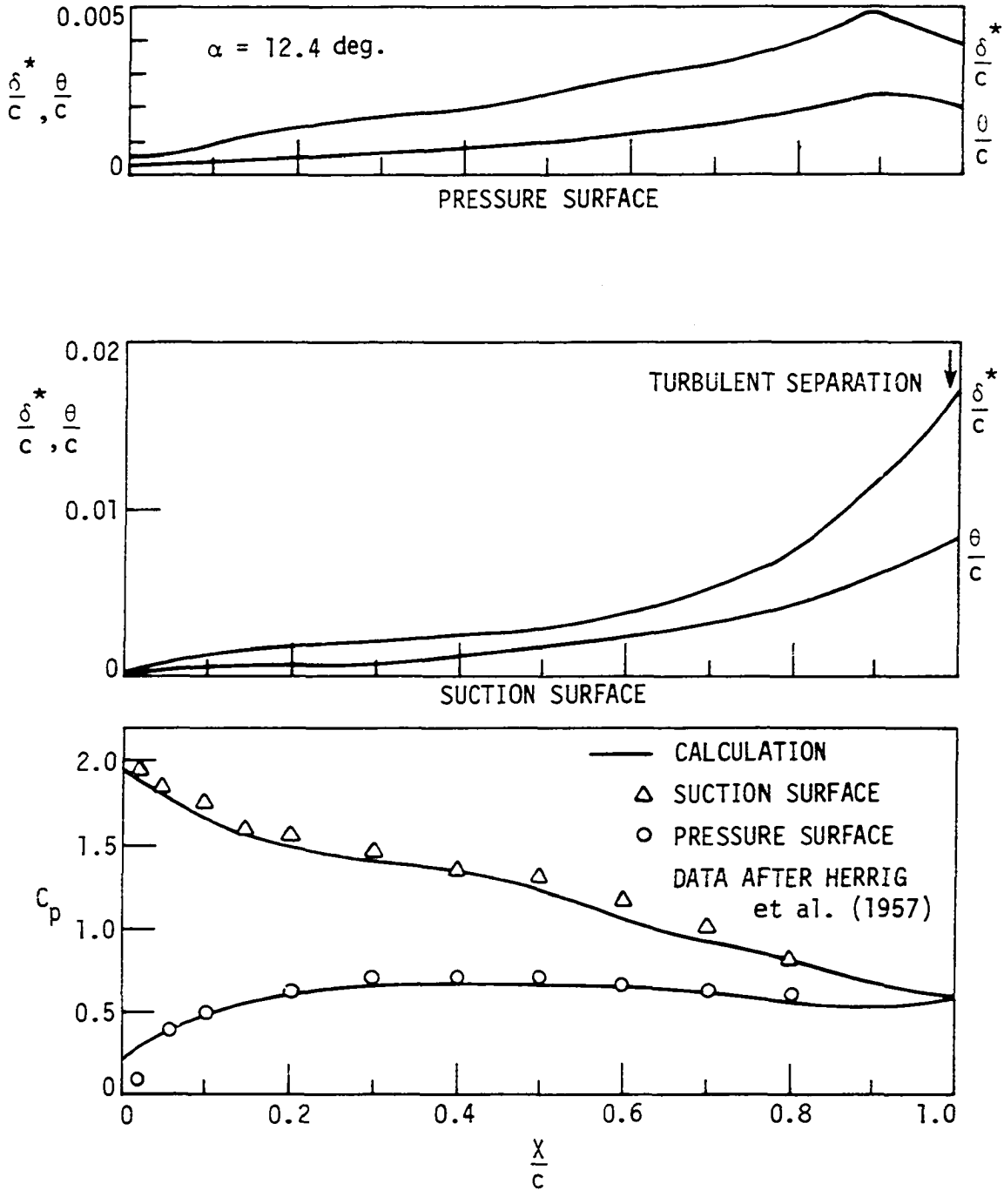

Figure 26. Calculated surface pressure compared with experimental data and calculated suction and pressure surface boundary layers. 65-410 blade, M_i = .1, Re_c = 245,000, γ = 45°, σ = .78, c = 124 mm.

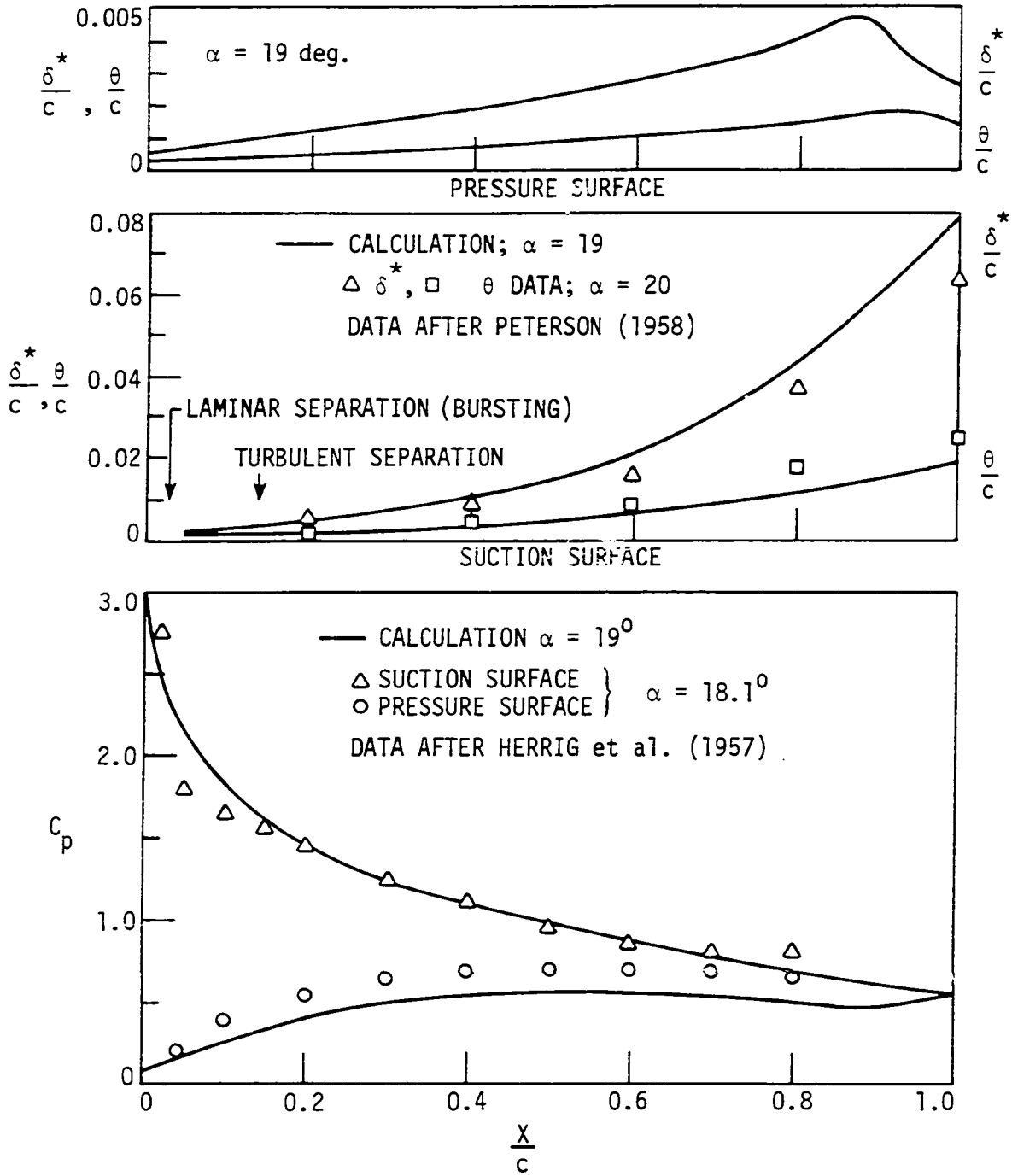

Figure 27. Calculated surface pressure compared with experimental data and calculated suction and pressure surface boundary layers. 65-410 blade, M_i = 0.1, Re_c = 245,000, $\gamma = 45^o$, σ = .78, c = 124 mm.

laminar separation and continued as a turbulent separated boundary layer, which means that the flow over most of the blade is separated.

65-(12)10 Blade Cascade

The turning, loss, and suction surface transition and separation points plotted against the inlet angle for the 65-(12)10 blade cascade are shown in Figure 28. The calculated turning, $\Delta\beta$, has a slope which is similar to the data, but the level of turning is not the same and at high angles of attack the turning does not decrease. The loss C_w seems to be at about the right level, but there is no rapid increase in C_w. The transition point moves forward with increasing incidence as expected and the separation point does so also. There is no laminar separation on the suction surface in any of the calculations and this may be the reason there is no sudden increase in the displacement thickness with the corresponding increase in C_w and decrease in $\Delta\beta$. The computation time for six incidence cases run consecutively was 3.28 hours.

The convergence of the calculations for the 65-(12)10 blade are shown in Figure 29. The calculations at the incidence angles, α = 12.5°, 17.7°, and 20.7° converged while those at α = 14.2°, 19.7°, and 21.7° used all eight iterations but all were in the process of converging and appeared to be close to convergence. There seems to be a general trend of increasing $\beta_{o,I}$ with increasing α. The values of incidence α = 12.5°, 14.2°, and 17.7° shows this as does Figure 24. However, at α = 19.7°, $\beta_{o,I}$ decreases. This is probably caused by an increase in the boundary layer thickness which causes the interpolation scheme to use

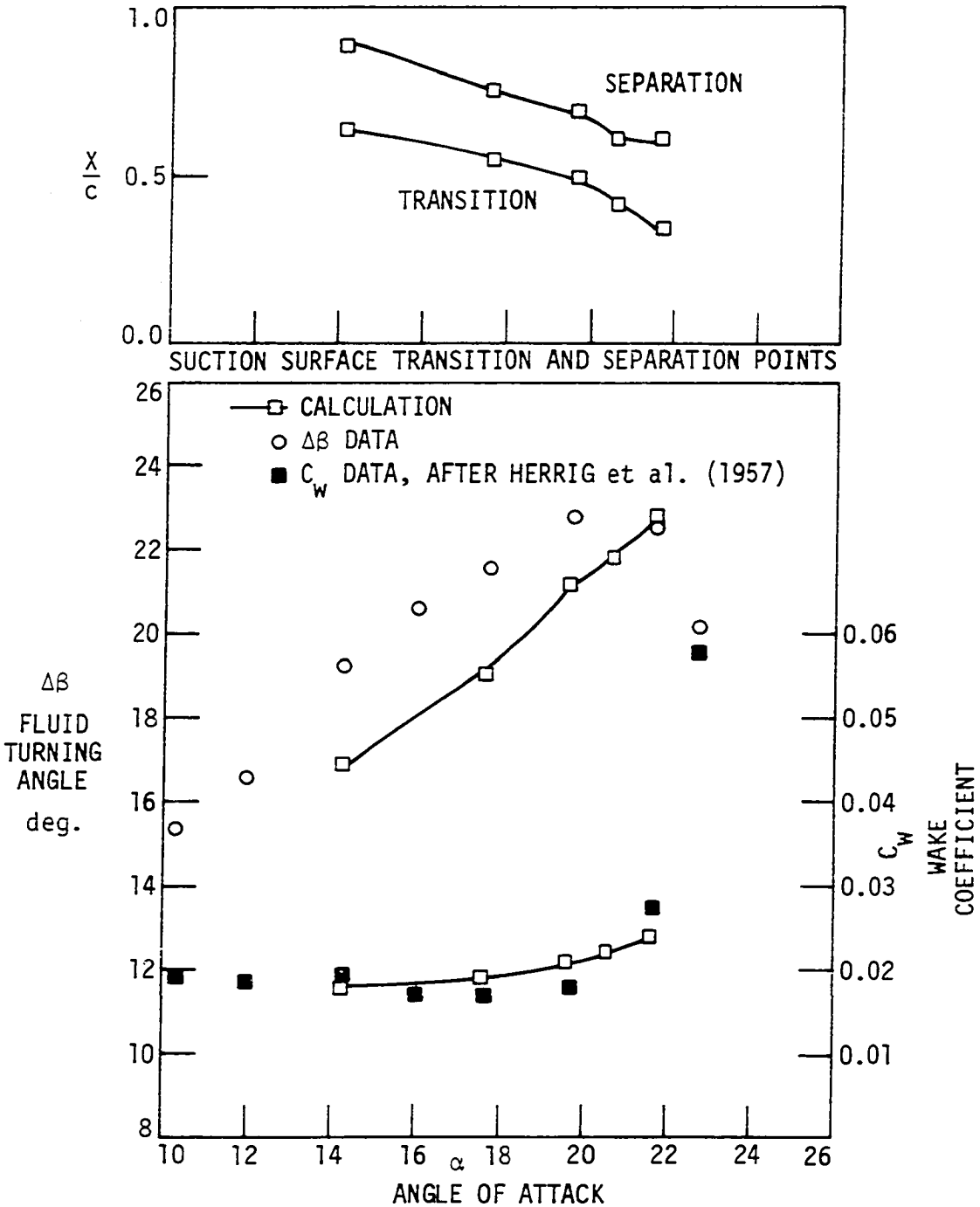

Figure 28. Calculated turning and loss compared with experimental data and calculated transition and separation points for a 65-(12)10 blade. M_1 = .1, Re_c = 245,000, σ = 1.0, γ = 45.7°, c = 124 mm.

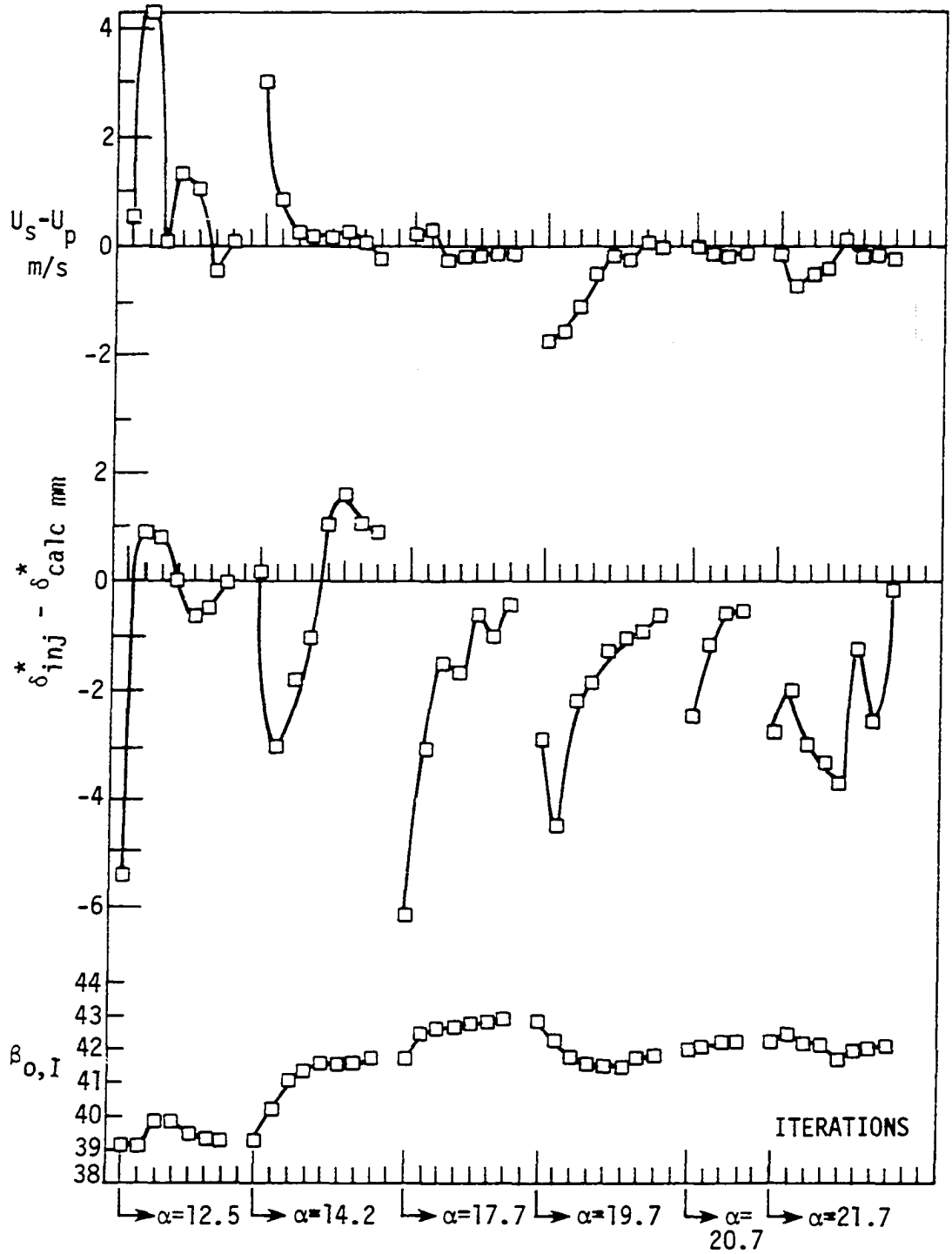

Figure 29. Convergence of the calculation for the 65-(12)10 blade cascade.

a different set of four points to obtain the surface pressures. This might produce such a jump, because there may be large variations in velocity from point to point in this region. This is not desirable because it produces an increase in turning when a decrease should be obtained. Surface pressure data are available at three different angles of attack, 14.2°, 17.7° and 21.7° from Herrig et al. (1957) and surface pressure and boundary layer data are available at $\alpha = 12.5°$ from Milsch (1971). The data of Milsch (1971) are taken at a slightly higher Mach number and contains information about the surface pressure and momentum thickness on both sides of the blade. Figure 30 shows the comparison of the calculation with the data after Milsch (1971). The surface pressures seem to be shifted, the calculation being lower than the experimental data, though the shapes seem to be about right. The calculated suction surface momentum thickness probably grows much more rapidly than the data because of the increased diffusion on the suction surface of the calculation over the experimental data. But the pressure surface momentum thickness seems to match quite well.

Figure 31 shows that for $\alpha = 14.2°$ the surface pressures match quite well with the data. At $\alpha = 17.7°$, Figure 32 shows that the experimental and calculated surface pressures match fairly well. However, at the trailing edge the calculation diffuses the flow too much. Also, the pressure surface boundary layer and surface pressure has a hump as a result of the laminar separation on that surface. At $\alpha = 21.7°$, Figure 33 shows that although over the leading edge portion of the blade the surface pressures match, at the trailing edge there is too much

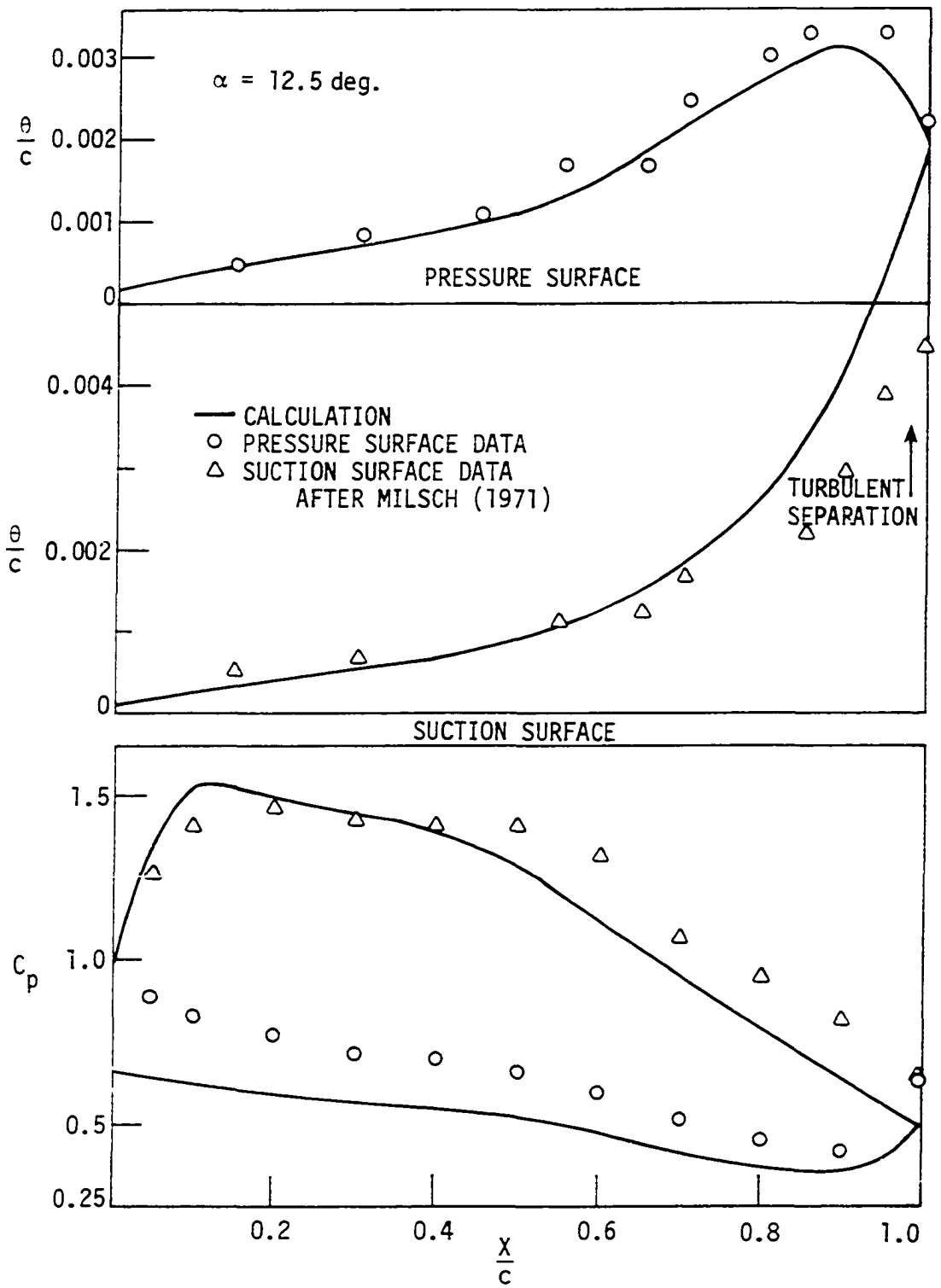

Figure 30. Calculated surface pressures and boundary layers compared with experimental data. 65-(12)10 blade, M_i = .15, Re_c = 430,000, σ = 1.0, γ = 45.7°, **c** = 124 mm.

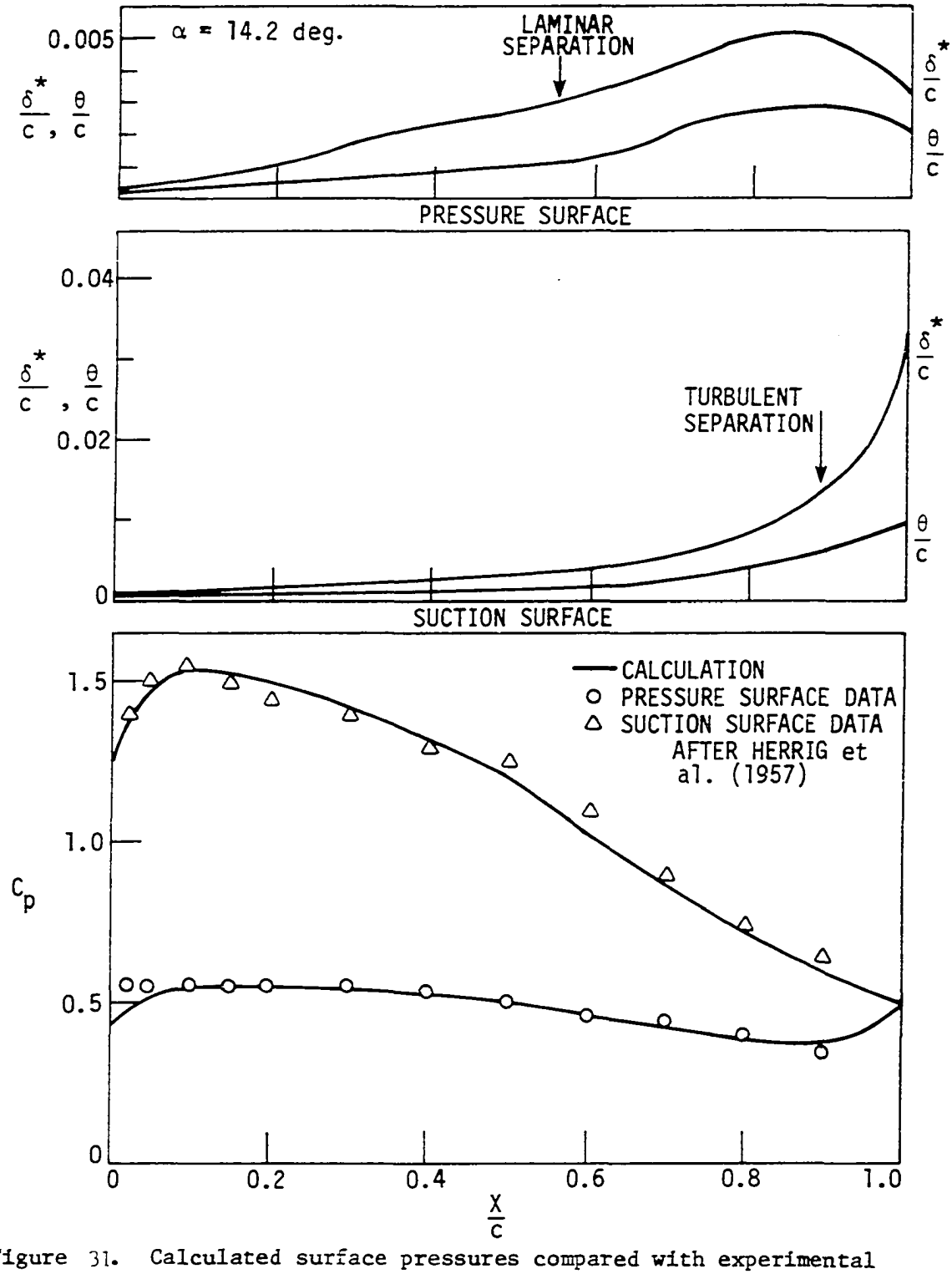

Figure 31. Calculated surface pressures compared with experimental data and calculated suction and pressure surface boundary layers. 65-(12)10 blade, M_i = .1, Re_c = 245,000, σ = 1.0, $\gamma = 45.7^{\circ}$, c = 124 mm.

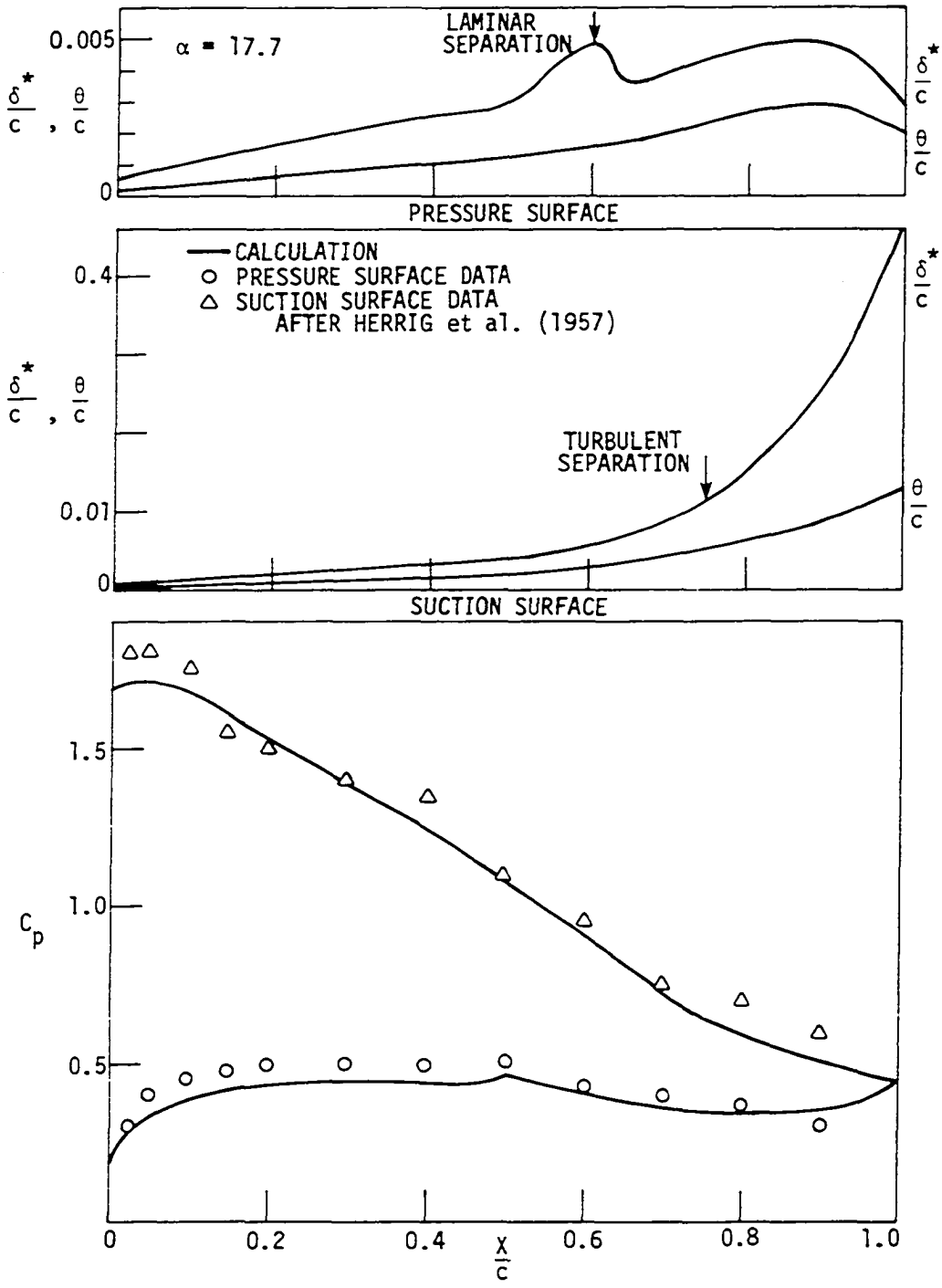

Figure 32. Calculated surface pressures compared with experimental data and calculated suction and pressure surface boundary layers. 65-(12)10 blade, M_i = .1, Re_c = 245,000, σ = 1.0, γ = 45.7°, c = 124 mm.

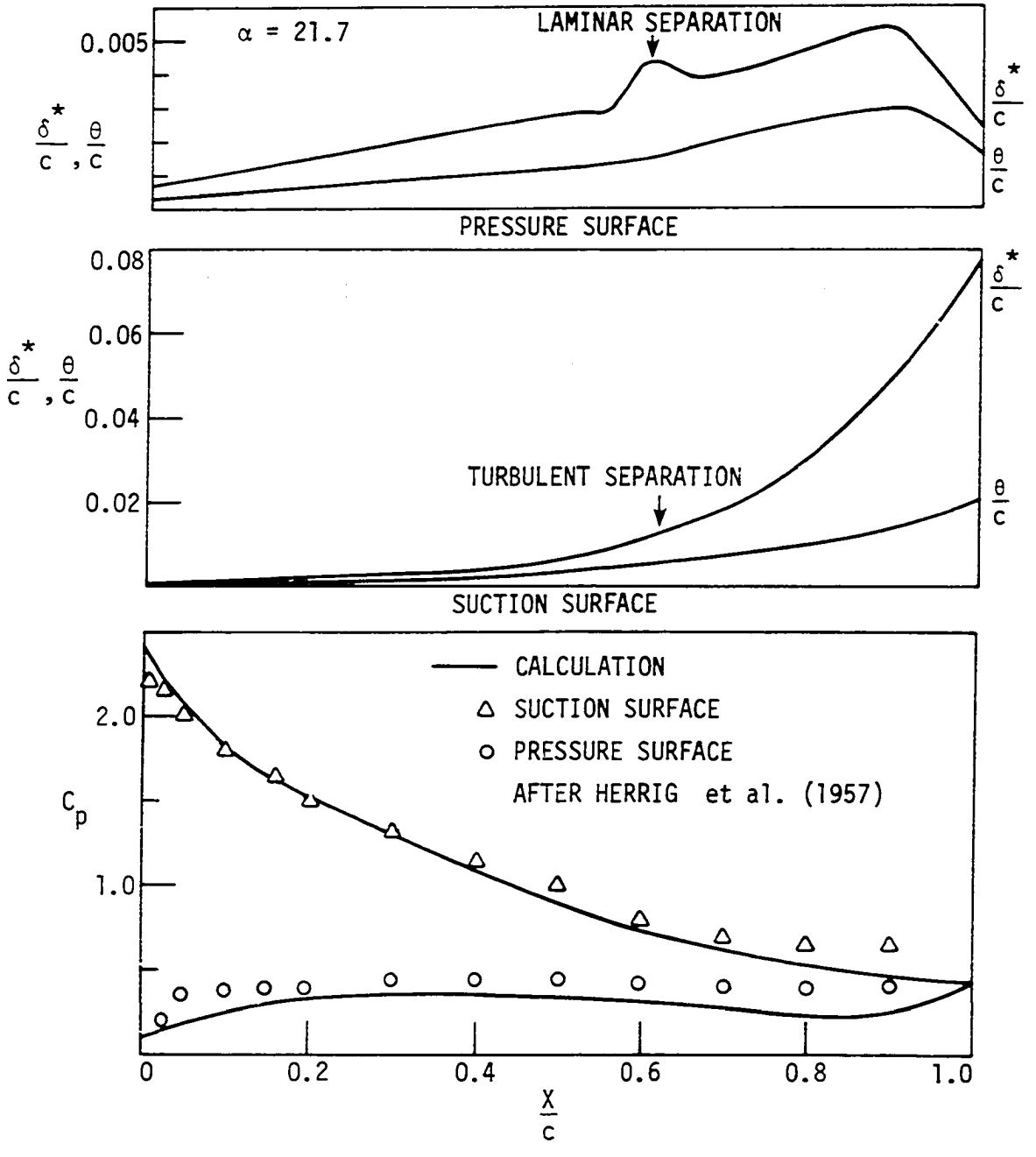

Figure 33. Calculated surface pressures compared with experimental data and calculated suction and pressure surface boundary layers. 65-(12)10 blade, M_i = .1, Re_c = 245,000, σ = 1.0, γ = 45.7°, c = 124 mm.

diffusion and again there is laminar separation on the pressure surface. Observe also, the movement of the turbulent separation point toward the leading edge in these last three figures.

In addition to these angles of attack, one higher angle, $\alpha = 22.7°$, was run for several iterations. Though it did not converge, it yielded some useful information. With an increased incidence angle the velocity peak from $\alpha = 21.7°$ to $\alpha = 22.7°$ remained almost the same and there was no laminar separation predicted. This suggests that it is important to correctly model the peak velocity on the suction surface to determine if there is any laminar separation.

The turning and loss for varying Reynolds numbers for the 65-(12)10 blade is given in Figure 34. The data were taken at Tu = 0.01 by Herrig et al. (1957), but when calculations were made at that value, the first point (Re_c = 350,000) did not quite converge and the last point (Re_c = 150,000) was not converging because the laminar separated region was oscillating between transition-reattachment and bursting. When the calculation was made at Tu = 0.005, the values for the turning and loss obtained are those in Figure 34. When the calculations were performed for Tu = 0.005, at Re_c = 350,000 the boundary layer underwent normal transition, at Re_c = 220,000 it separated and reattached and at Re_c = 150,000 bursting occurred. The trend of decreasing $\Delta\beta$ and increasing C_d with decreasing Re_c is shown correctly, though overestimated. The computation time for the four Reynolds number cases was 1.32 hours.

Figures 35 and 36 show the high speed test for the 65-(12)10 blade. The points of transition and separation shown in Figure 35 both move

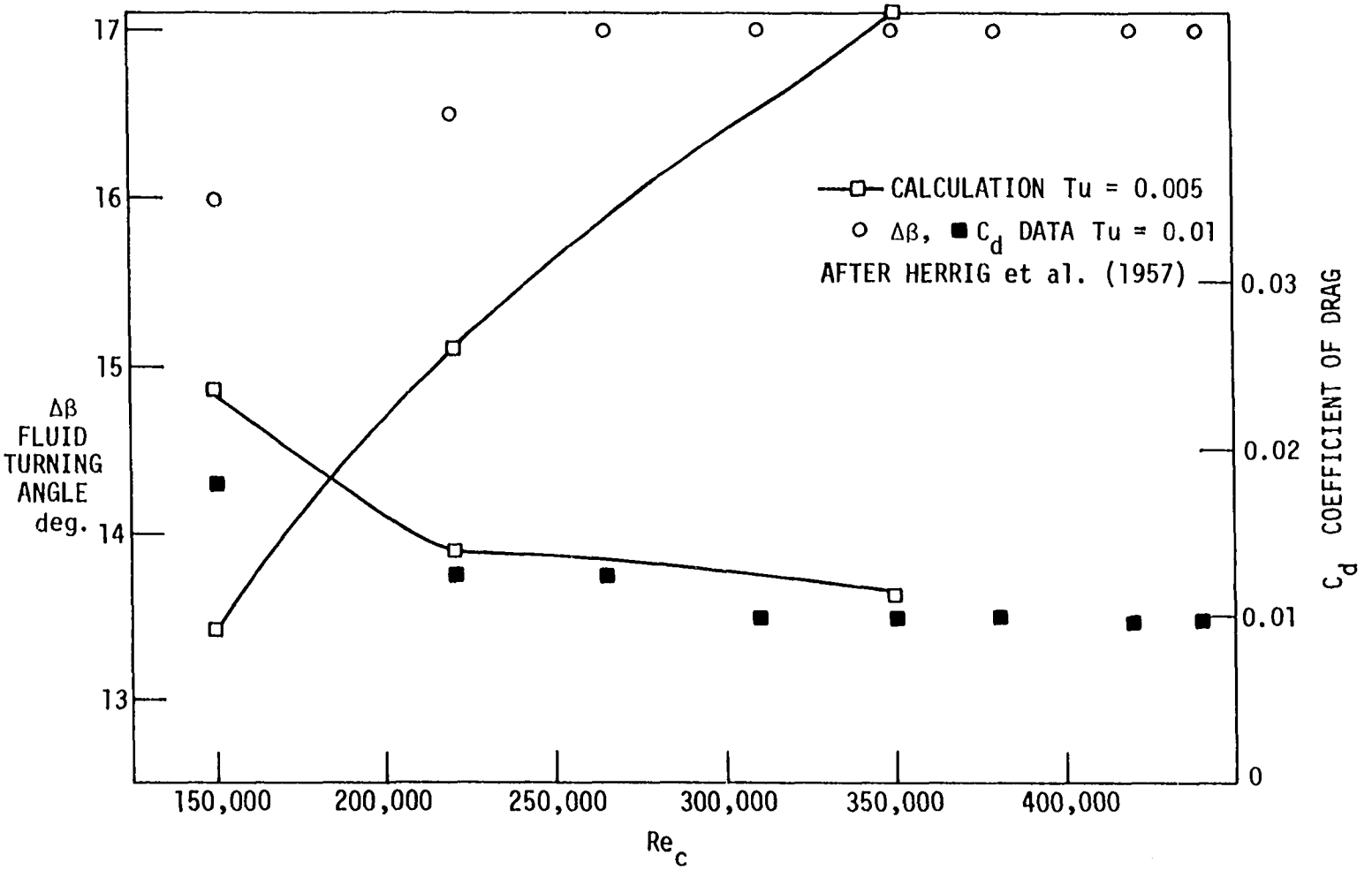

Figure 34. Calculated turning and loss compared with experimental data for a 65-(12)10 blade. α = 12, $M_i \approx .1$, σ = 1.0, γ = 45.7°, c = 124 mm.

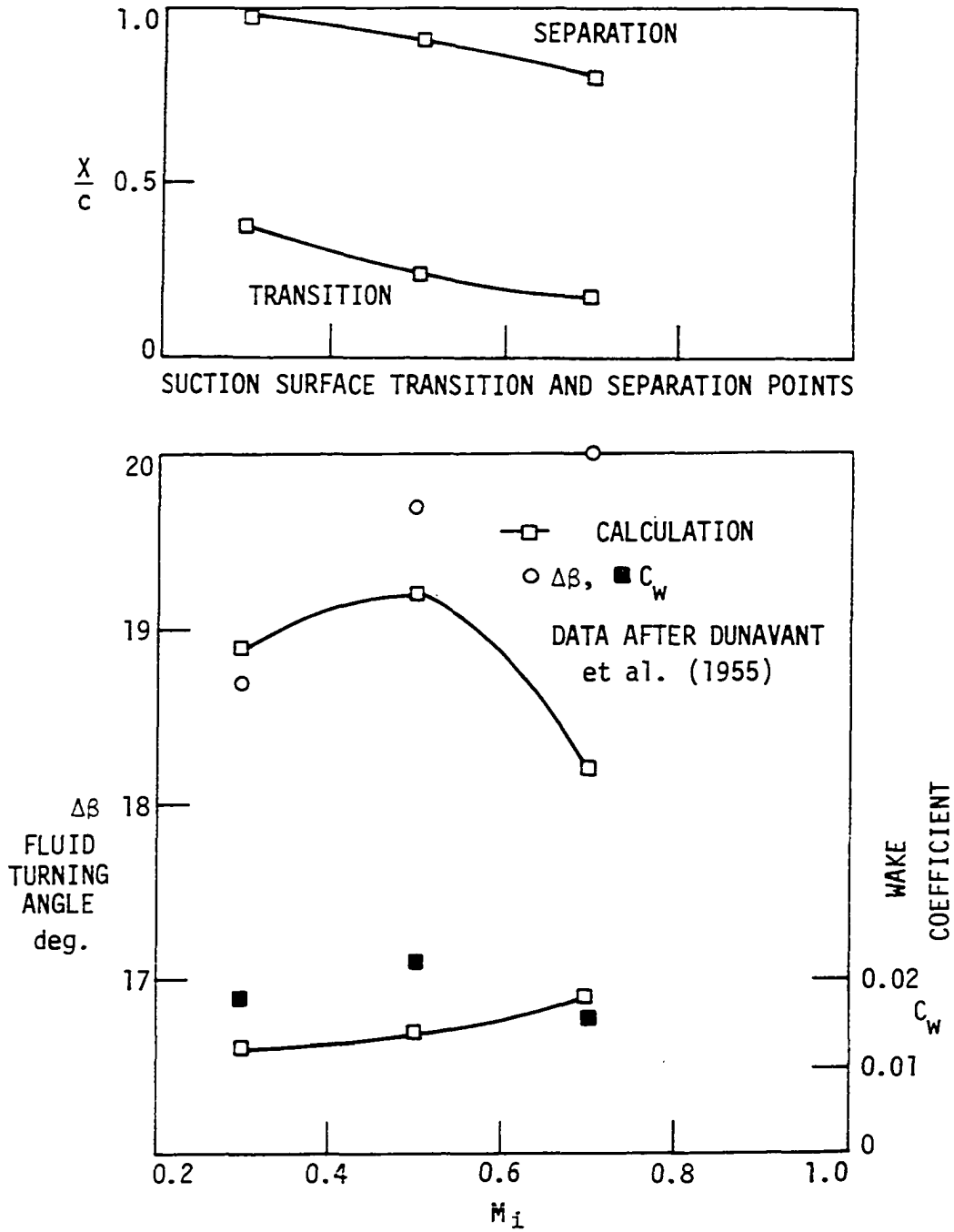

Figure 35. Calculated turning and loss compared with experimental data and calculated transition and separation points for a 65-(12)10 blade. $\alpha = 14.3$, $\sigma = 1.0$, $\gamma = 45.7^{\circ}$, $Re_c = 8.7 \times 10^5 - 2 \times 10^6$, $c = 124$.

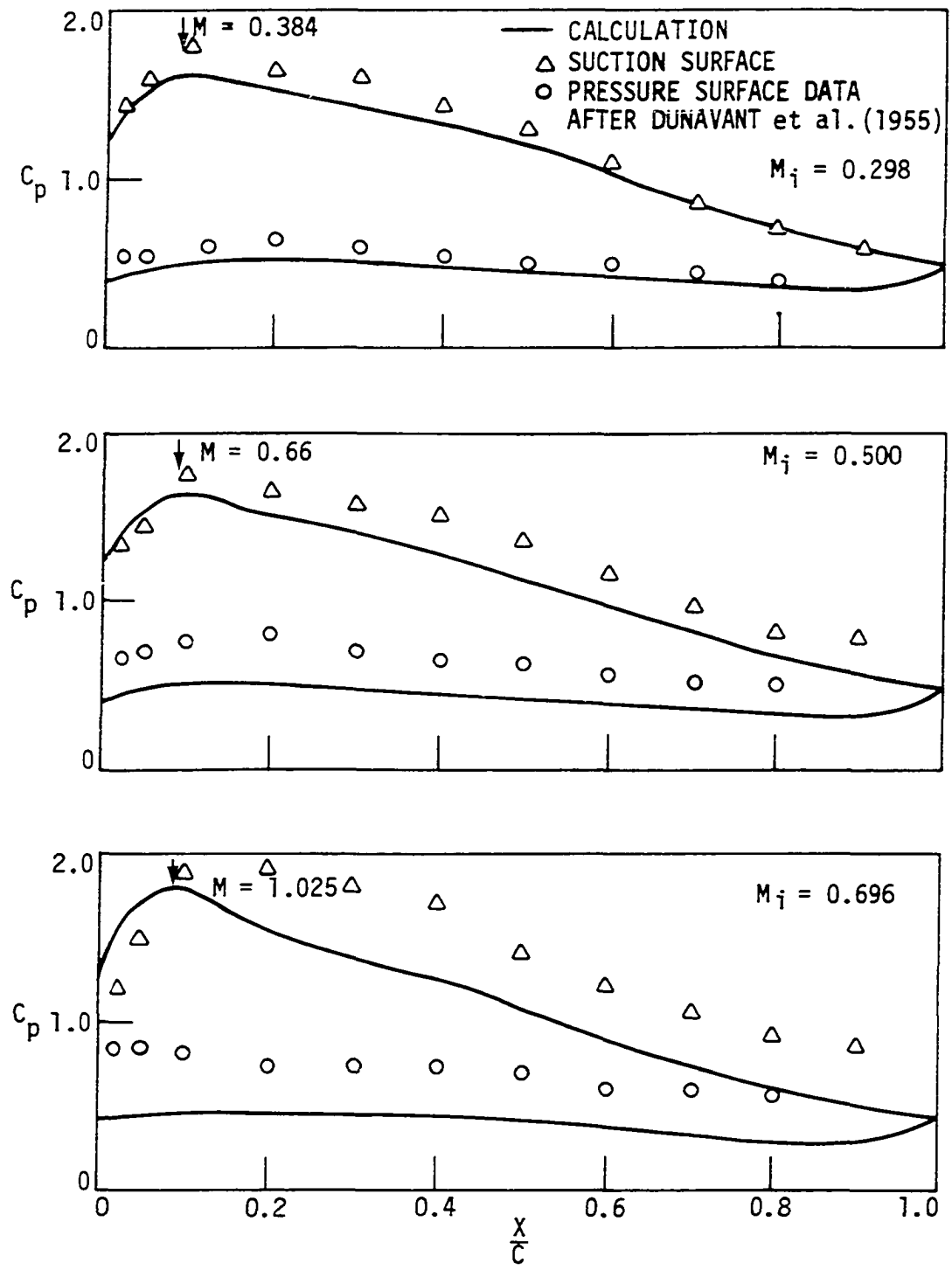

Figure 36. Calculated surface pressures compared with experimental data. 65-(12)10 blade α = 14.3, σ = 1.0, γ = 45.7°, $Re_c = 8.7 \times 10^5 - 2 \times 10^6$, c = 124.

forward as the Mach number is increased. The turning does match well at $M_i = 0.3$, but does not follow the trend of the experimental data at high Mach numbers. The loss, though near the correct level, does not match the experimental data. The surface pressures in Figure 36 show that at $M_i = 0.298$ the calculated pressures match the experimental pressures well, even near the trailing edge. At the higher Mach numbers there is a significant difference in the calculated and measured pressures, especially near the trailing edge, but the suction surface peak is almost duplicated in all three cases. The computation time for the three Mach number cases was 1.23 hours.

65-($12A_2I_{8b}$)10 Blade Cascade

The turning, loss, and transition and separation points plotted against the angle of attack for the the 65-($12A_2I_{8b}$)10 blade cascade are shown in Figure 37. Again as in the previous cases, the slope of the calculated $\Delta\beta$ is similar to the data but the levels are not the same and as in the 65-(12)10 case, $\Delta\beta$ does not decrease as does the data at high angles of attack nor does C_w increase at high angles of attack. The transition location moves forward as would be expected but no laminar separation is calculated. The turbulent separation line remains almost horizontal probably because of the shape of the suction surface pressure distribution near the trailing edge. The computation time for the five incidence cases was 2.06 hours.

The convergence of the calculations for the 65-($12A_2I_{8b}$)10 blade is displayed in Figure 38. Convergence is obtained in $\alpha = 12.5°$, $14.7°$,

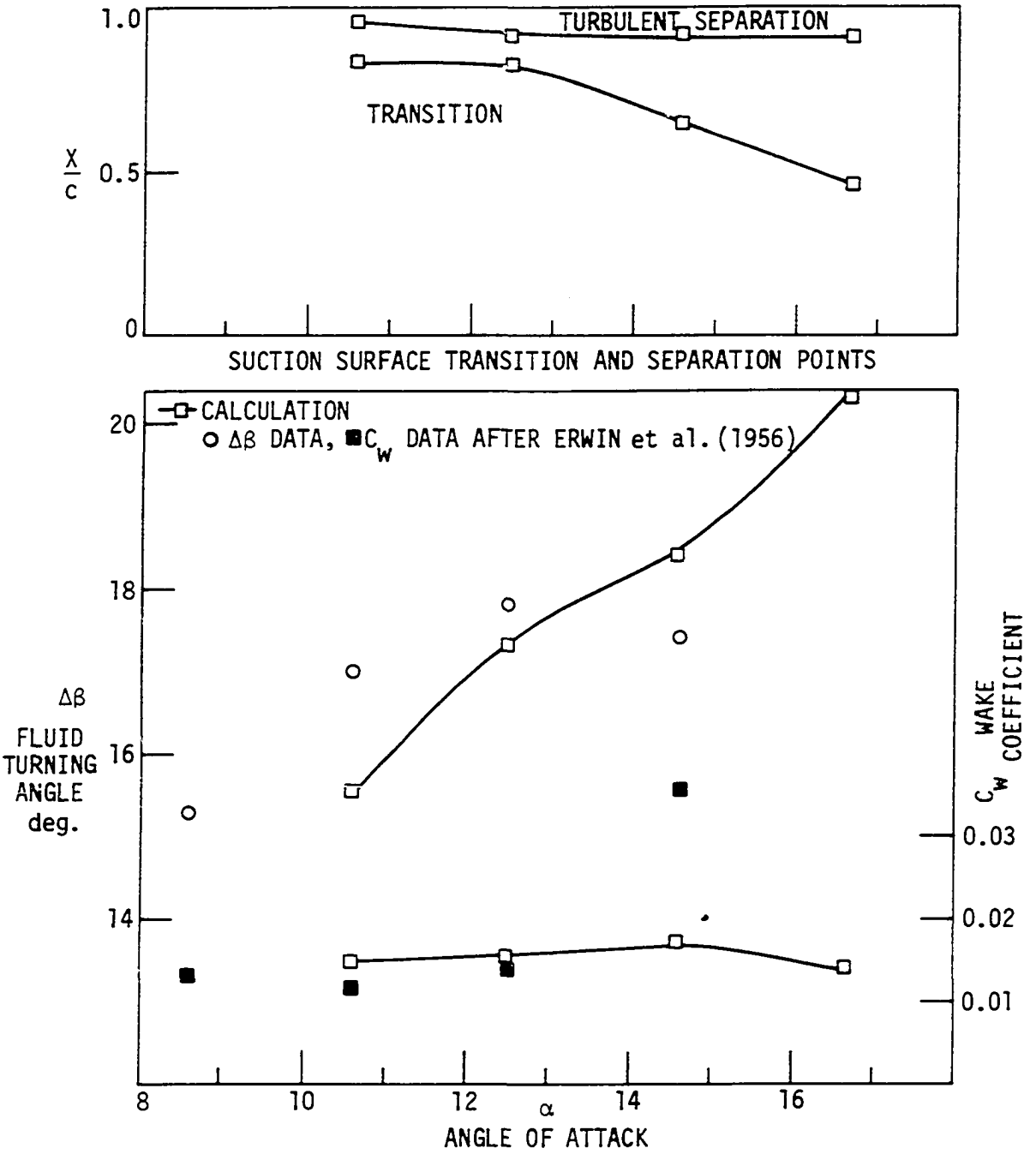

Figure 37. Calculated turning and loss compared with experimental data and calculated transition and separation points for a 65-($12A_2I_{8b}$)10 blade. $M_1 = 0.1$, $Re_c = 440{,}000$, $\gamma = 45.3^\circ$, $\sigma \cong 1.0$, $c = 124$ mm.

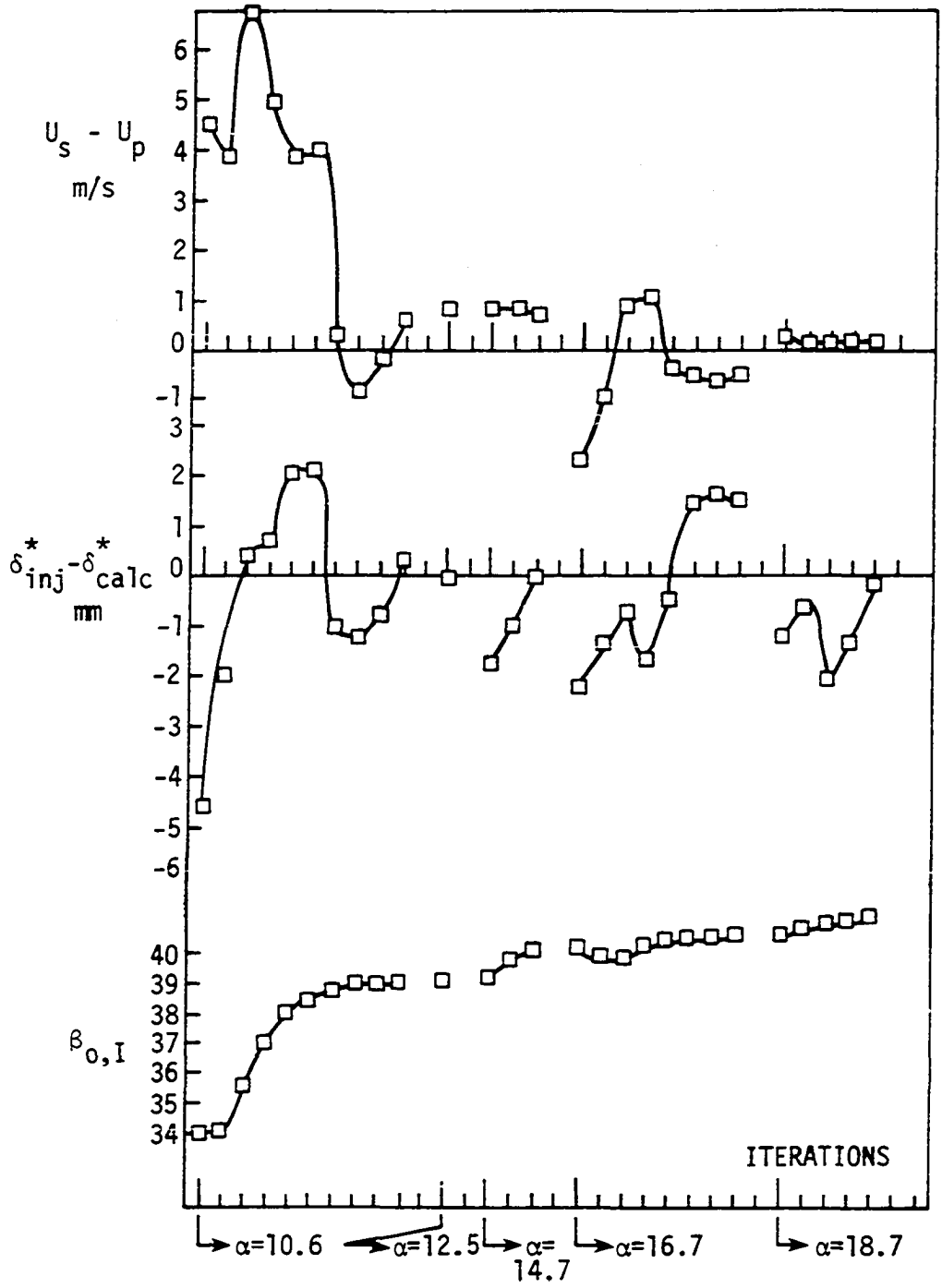

Figure 38. Convergence of the calculation for the 65-$(12A_2I_{8b})$10 blade cascade.

and 18.7° while a solution was being converged upon in α = 10.6° even though the iteration limit was exceeded. However, for α = 16.7°, there appears to be some difficulties in converging. Also, as seen before, $\beta_{o,I}$ in general increases as α increases.

Surface pressure calculations are compared with the available data at α = 10.6°, 12.5°, and 14.7°. Figures 39 and 40 exhibit good agreement of the calculated and measured surface pressures. The separation point remains almost constant probably because the pressure remains nearly constant on the suction surface and then increases very rapidly near the trailing edge almost insuring separation. Now at α = 14.7°, Figure 41 reveals that the calculation did not duplicate the suction surface velocity peak, and as a result there was no laminar separation near the leading edge and no large increases in the momentum thickness which should occur at high angles of attack.

The turning and loss for various inlet Reynolds numbers are shown in Figure 42. The exact turbulence level for this case is not known and Tu = 0.005 was used as input to the calculation. However, though the levels of $\Delta\beta$ and C_d are off somewhat, the right trend is shown and bursting is predicted at Re_c = 200,000 where the C_d data is growing rapidly. The computation time for the four Reynolds number cases was 1.28 hours.

For the high speed test cases, Figure 43 presents the turning, loss, and the transition and separation points. Although each of the three calculated cases converged, there seems to be little explanation as to why $\Delta\beta$ does not match at M_i = .306 while C_w does and why $\Delta\beta$ matches

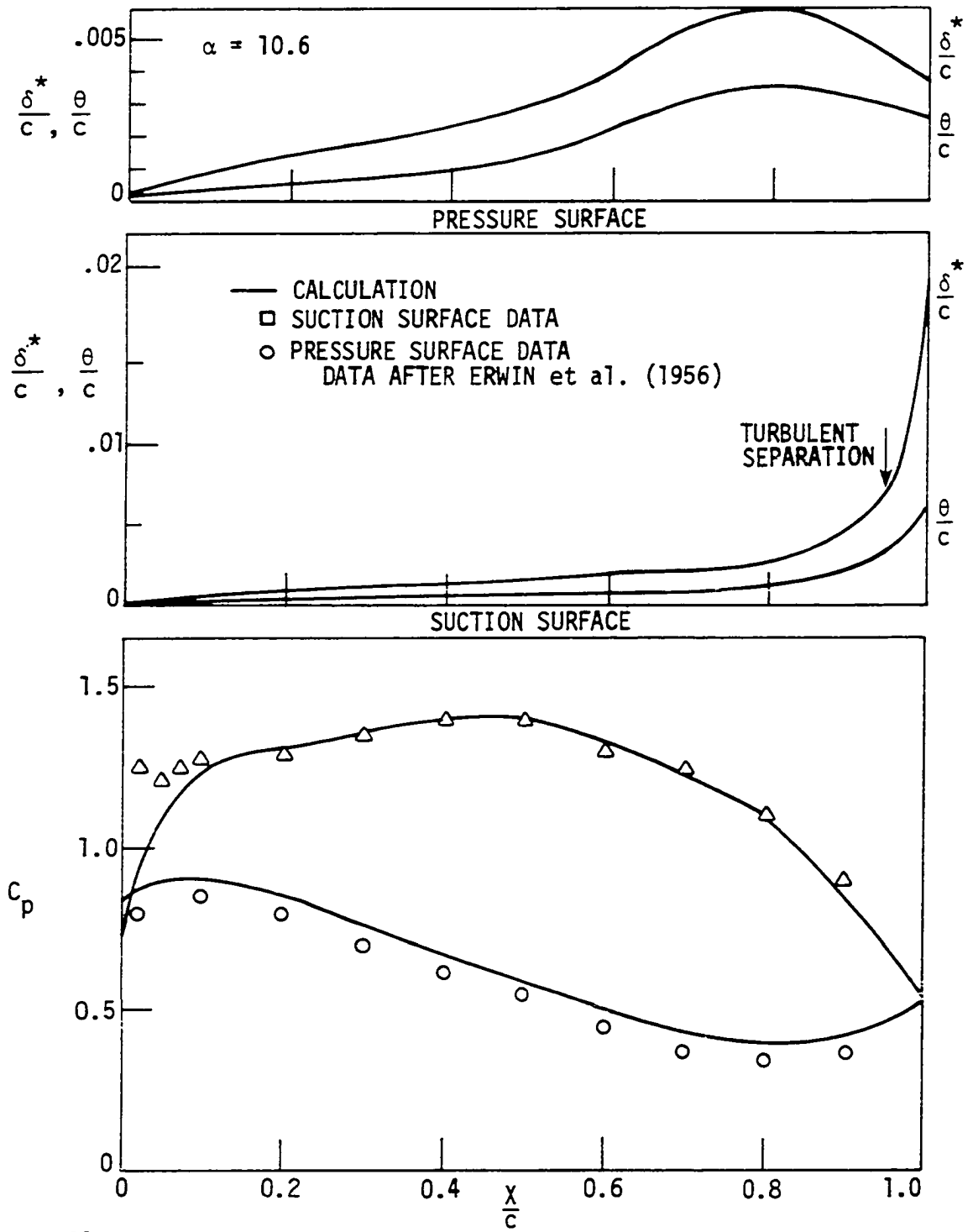

Figure 39. Calculated surface pressure compared with experimental data and calculated suction and pressure surface boundary layers. 65-($12A_2I_{8b}$) blade, M_i = 0.1, Re_c = 440,000, σ = 1.0, γ = 45.3 , c = 124 mm.

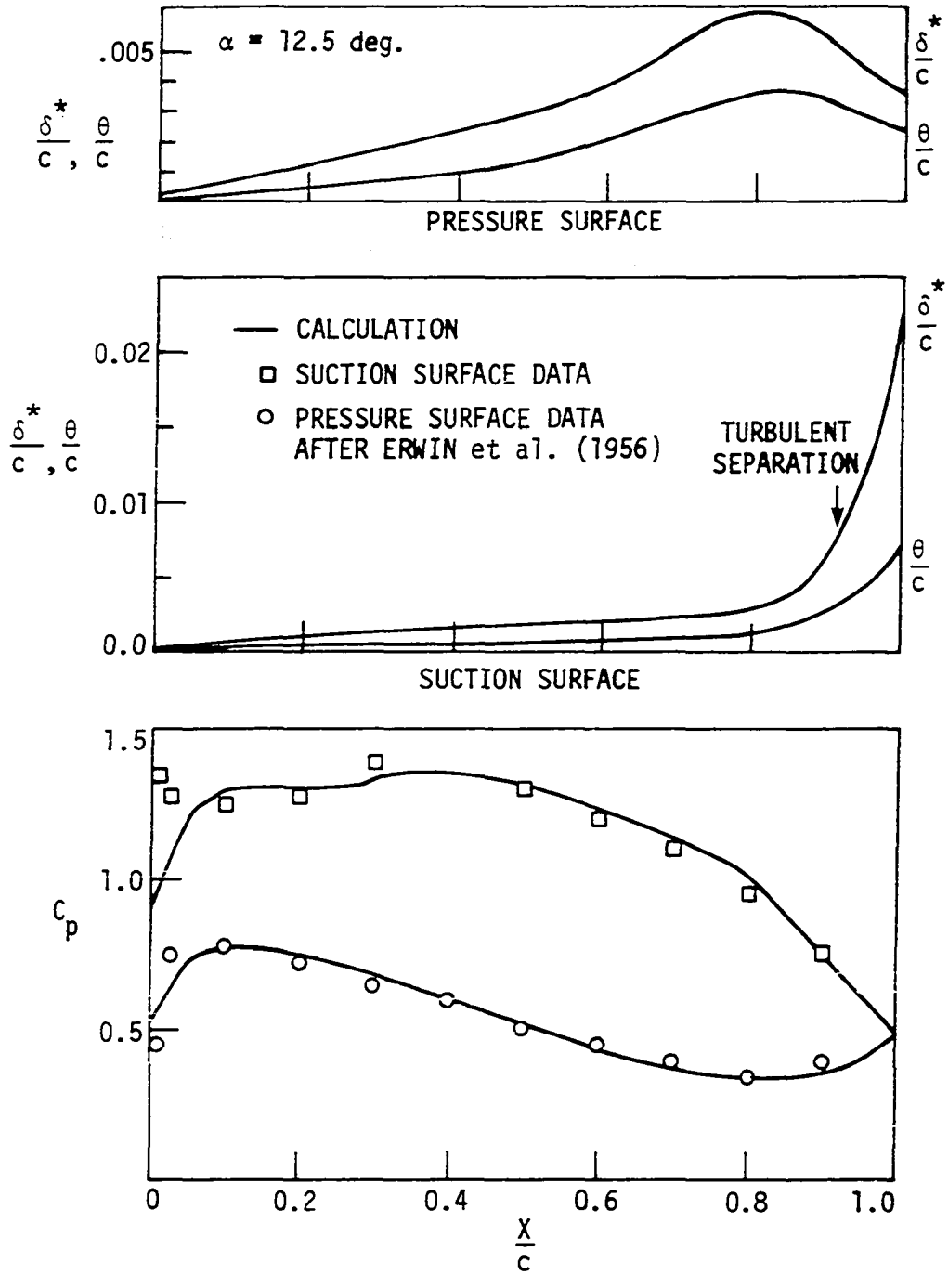

Figure 40. Calculated surface pressures compared with experimental data and calculated suction and pressure surface boundary layers. 65-($12A_2I_{8b}$)10 blade, M_i = 0.1, Re_c = 444,000, σ = 1.0, γ = 45.3°, **c** = 124 mm.

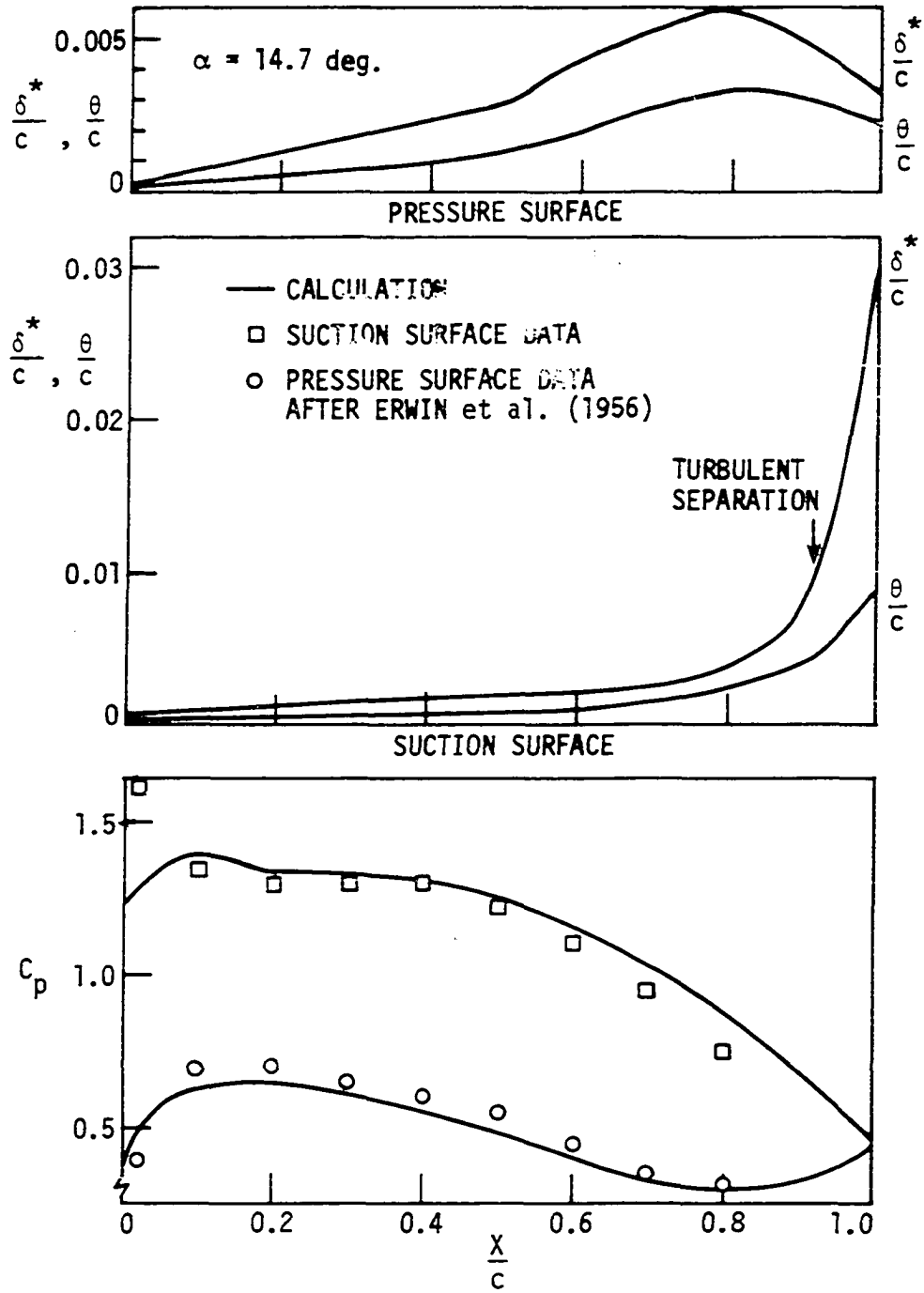

Figure 41. Calculated surface pressures compared with experimental data and calculated suction and pressure surface boundary layers. 65-($12A_2I_{8b}$)10 blade, M_i = 0.1, Re_c = 444,000, σ = 1.0, γ = 45.3°, c = 124 mm.

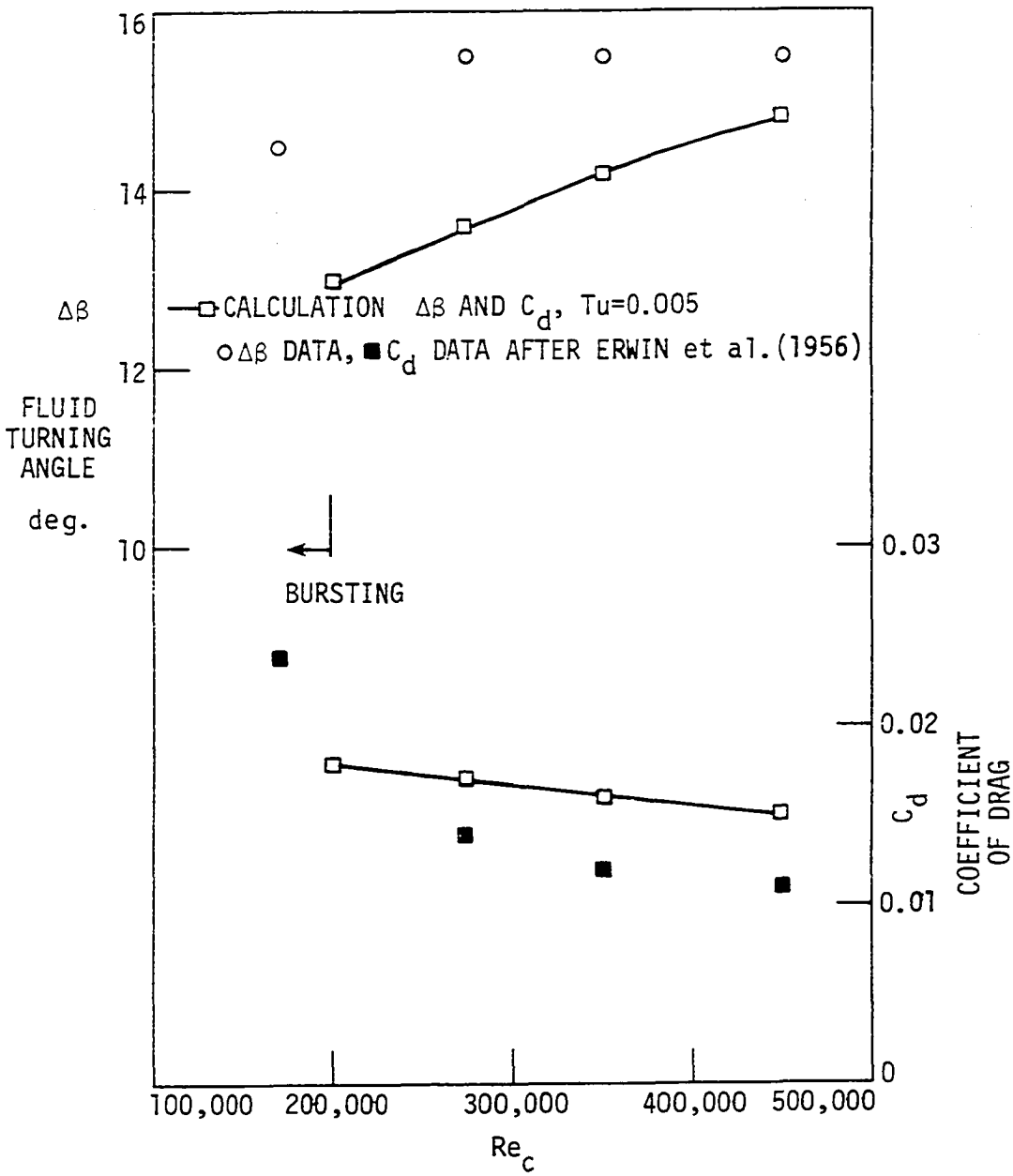

Figure 42. Calculated turning and loss compared with experimental data for a 65-$(12A_2I_{8b})$10 blade. $\alpha = 9.6$, $M_i = 0.1$, $Re_c = 440{,}000$, $\sigma = 1.0$, $\gamma = 45.3^\circ$, $c = 124$ mm.

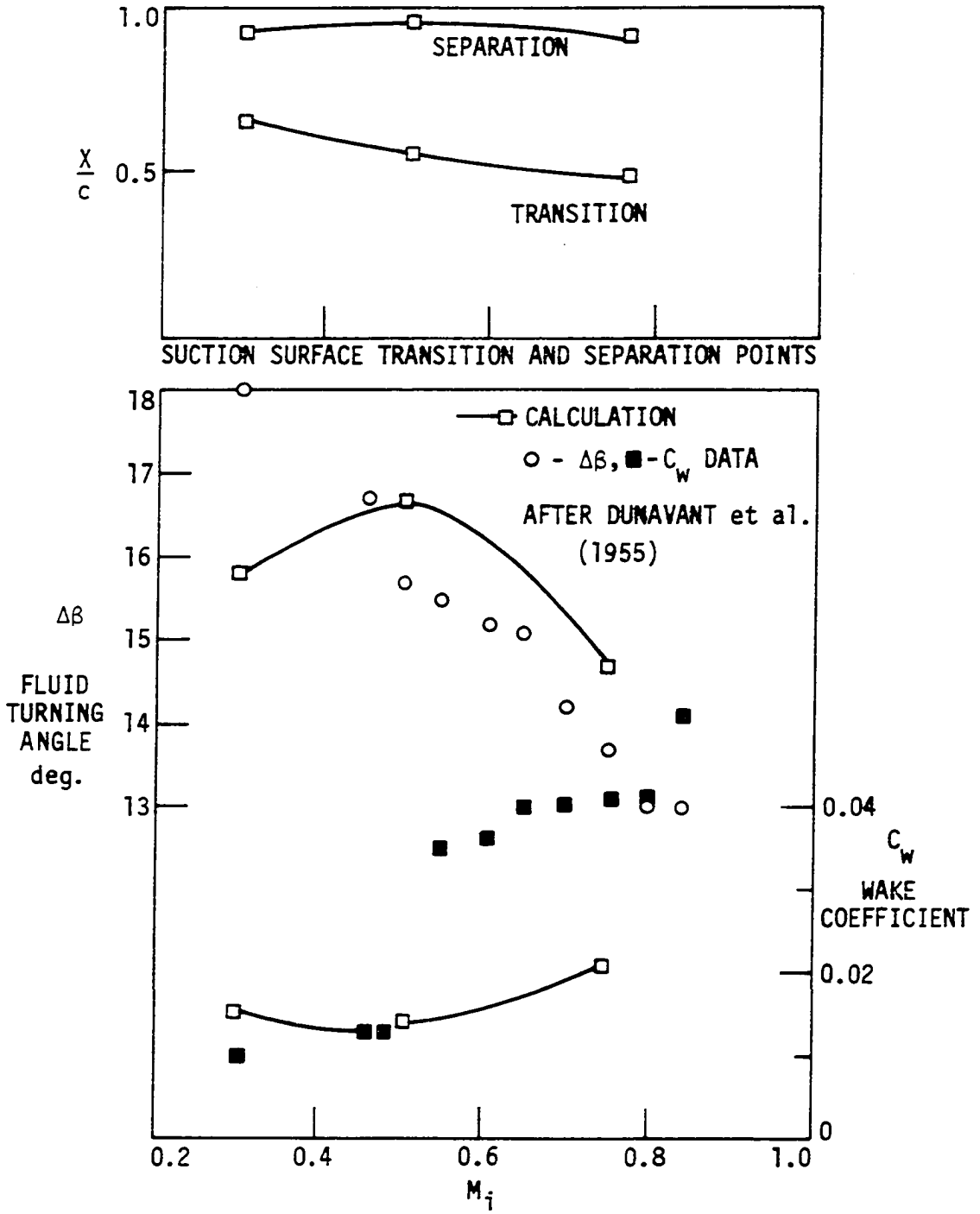

Figure 43. Calculated turning and loss compared with experimental data data and calculated transition and separation points for a 65-($12A_2I_{8b}$)10 blade. α = 11, γ = 45.3°, σ = 1.0, c = 124 mm.

at M_i = .755 while C_w does not. The corresponding surface pressure diagrams are given in Figure 44. At M_i = 0.306 the surface pressures seem to match fairly well. At higher inlet Mach numbers the surface pressures do not match as well and at M_i = 0.755 the transition of the boundary layer near X/c = 0.4 seems to have caused some oscillations in the suction surface velocity. The computation time for the three Mach number cases is 1.42 hours.

Matching Actual and Calculated Flow Fields

The object of the present research has been to model as closely as possible the real flow on a blade-to-blade axially symmetric surface. After looking at the previous comparisons of experimental and calculated data, it is assumed that some part or parts of the model are inadequate. When using an inviscid flow calculation with injection, as in the present model, one intends to predict a flow in the region where the flow is not dominated by viscous forces, that is the same as the experimental flow field in the same region. However, Figures 27 and 33 show that even though the proper amount of injection is applied (i.e., Figure 27 the displacement thicknesses are nearly the same and in Figure 33 the loss is nearly the same) the calculated surface pressures near the trailing edge are higher than the experimental values. Figure 45, a plot of constant pressures in terms of velocities, also shows that on the suction surface the measured pressure (in terms of velocity), U = 98, does not match the calculation for the same injection and outlet angle. In all three cases the measured surface pressure is lower than that calculated (the velocity

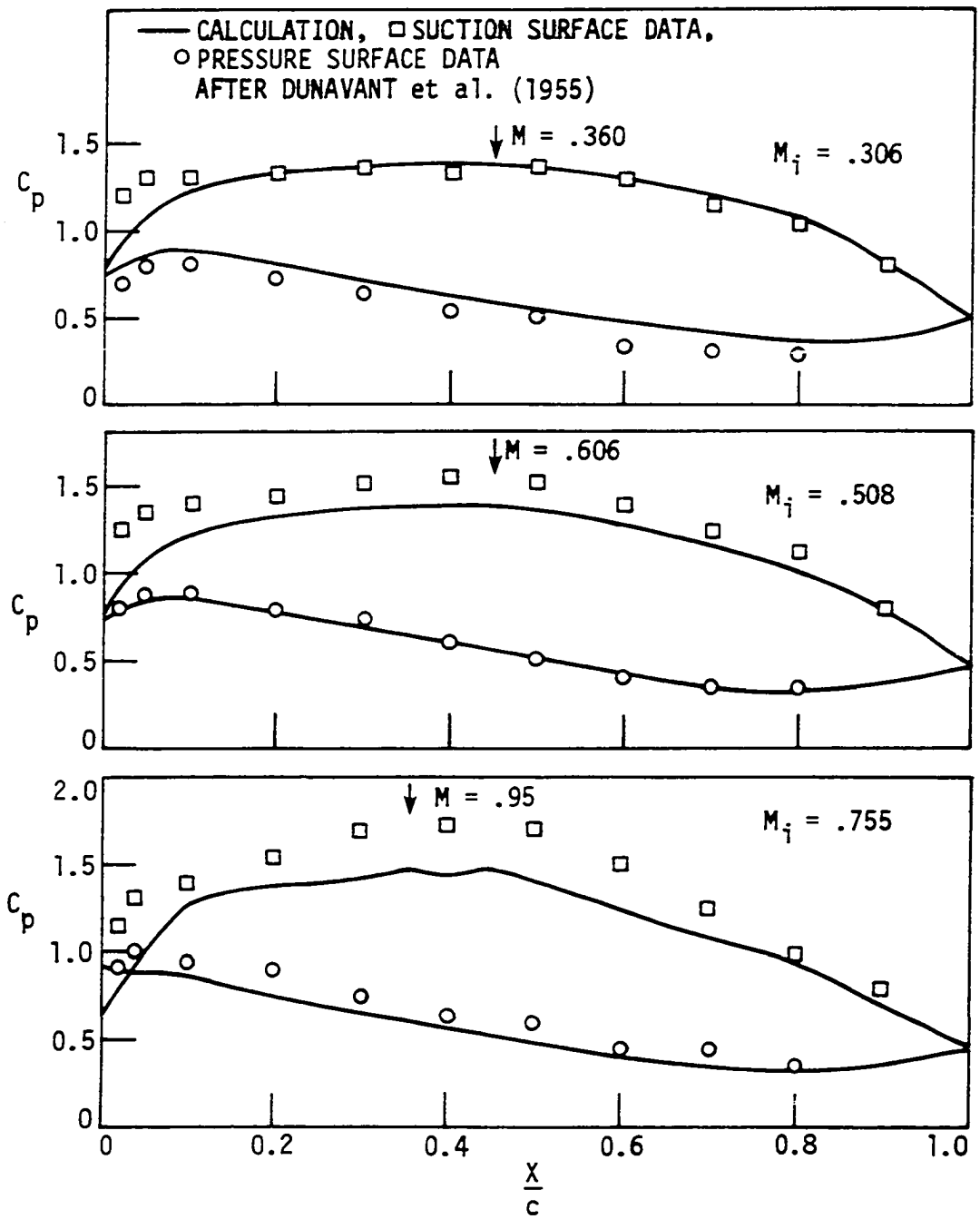

Figure 44. Calculated surface pressures compared with experimental data.
65-($12A_2I_{8b}$)10 blade, σ = 1.0, γ = 45.3°, c = 124 mm

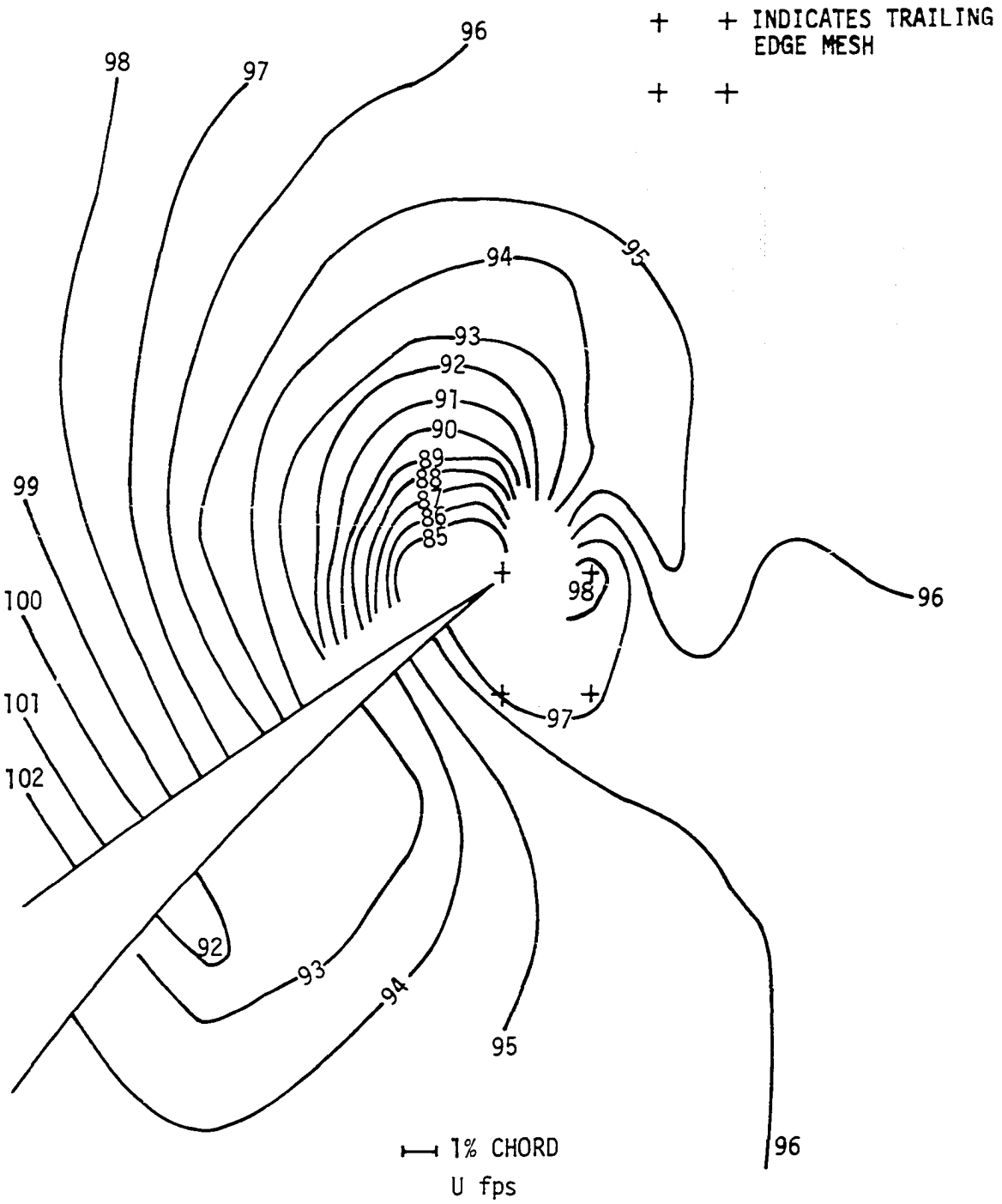

Figure 45. Constant velocity lines in the inviscid flow near the trailing edge of the 65-410 cascade. U_i = 113.4 fps, $\alpha = 9.3^{o}$, measured boundary layer displacement thickness and outlet angle used in the calculation.

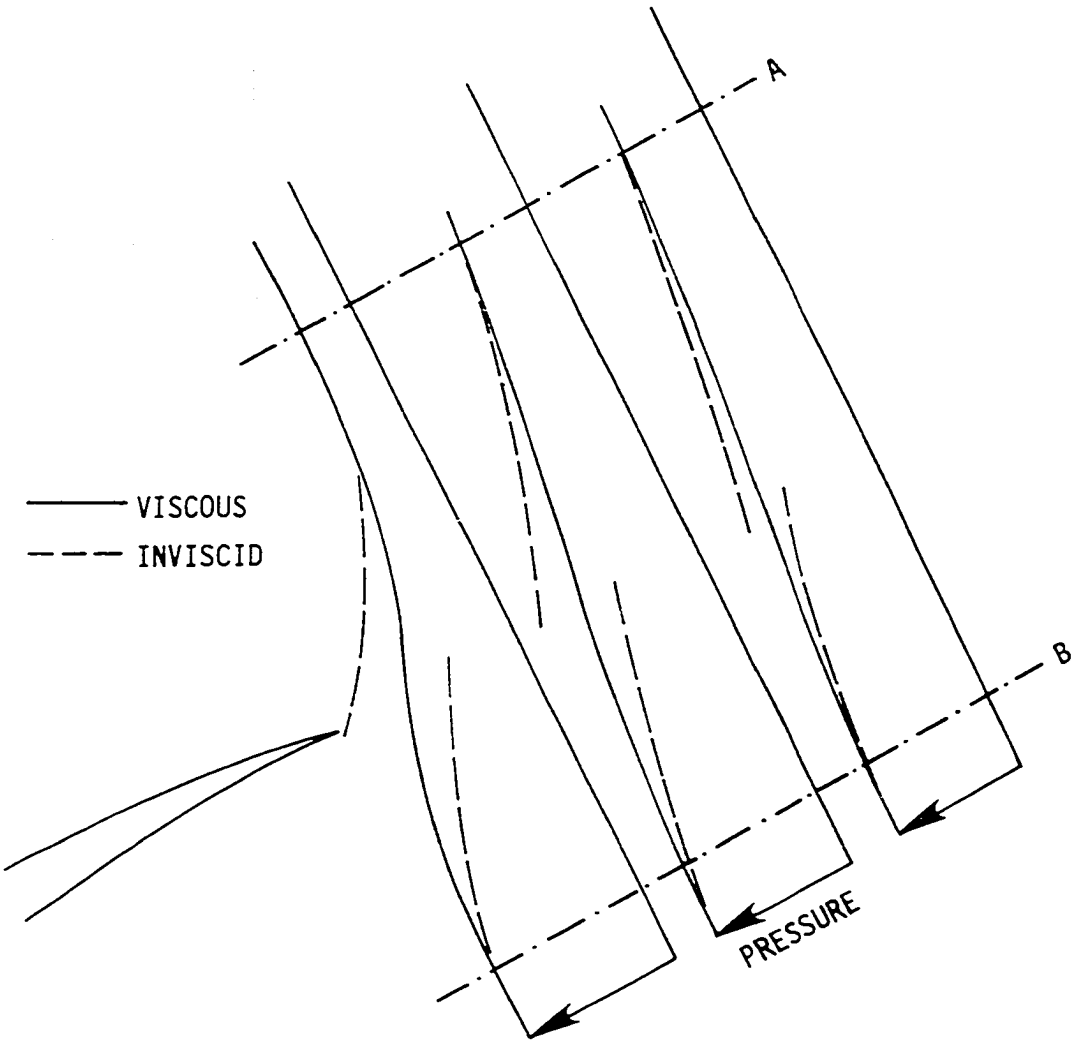

Figure 46. Difference between the actual viscous and the calculated pressure distribution in planes normal to the general streamline direction, showing an inviscid pressure jump.

was higher). This could possibly be a result of not calculating an inviscid flow field which is the same as the real flow field in the region not dominated by viscous forces. These two may not match because of the way the inviscid periodic boundary conditions downstream of the blade are set and the way in which the pressure is calculated through the boundary layer and wake.

In Figure 46 imagine that A and B are the boundaries between the viscous dominated and nondominated regions and that the solid line is the real static pressure through the viscous layer. Now, if the flow fields outside of A-B are matched, the static pressures of the real flow and the calculated flow are equal along A and B, the inviscid calculation within A-B does not necessarily have continuous pressure as does the real viscous flow. If the inviscid and the real viscous streamlines within A-B have somewhat the same shape (i.e., curvature) the normal pressure gradient which can be calculated from $\frac{\partial p}{\partial \eta} = \frac{\rho u^2}{r}$ will be larger for the inviscid flow than for the real flow as shown by the dashed line, because of higher velocities. This means that in general, there needs to be a pressure jump in the inviscid calculation along a line beginning at the trailing edge so that the real and the inviscid flow fields match in the region not dominated by viscous forces. It is also necessary that the displacement thickness in the viscous layer also be properly modeled in this region to produce a properly calculated flow field. Actually, the real viscous flow at the trailing edge is quite different from the inviscid flow calculated in the region between A and B. It appears essential that the inviscid flow be correctly calculated to obtain the correct pressures

at the edge of the viscous layer.

In the calculation of real blade-to-blade flow on an axially symmetric surface, the following facts should be considered. First, accurate calculations in the trailing edge region are essential to obtain proper levels of turning. Second, if an inviscid-viscous model is used, great care must be exercised in the application of the boundary conditions to the inviscid flow in the region of the trailing edge and downstream. Finally, to obtain the proper pressure change through the viscous layer it is necessary to calculate the viscous flow field in that region.

Boundary Layer Growth

Although the calculated turning of the present model did not match the experimental results very well, in the case of the 65-410 blade at high angle of attack and the 65-(12)10 blade at low Reynolds numbers there was a significant increase in the suction surface boundary layer displacement and momentum thicknesses and the loss and a decrease in turning. These give insight into the nature of the boundary layer as it grows on the suction surface and the effect it has on the turning. Figure 47a also shows the different boundary layers for the 65-(12)10 blade at 3 different Reynolds numbers. The momentum thicknesses are basically the same until $X/c \simeq 0.4$. However, after that point they begin to differ greatly. Figure 47b shows the growth of the momentum thickness on the 65-410 blade at three angles of attack compared with data. Notice that in both the calculation and the experimental data the size of the boundary layer differs considerably by $X/c = 0.2$. Figure 48 shows the boundary layer

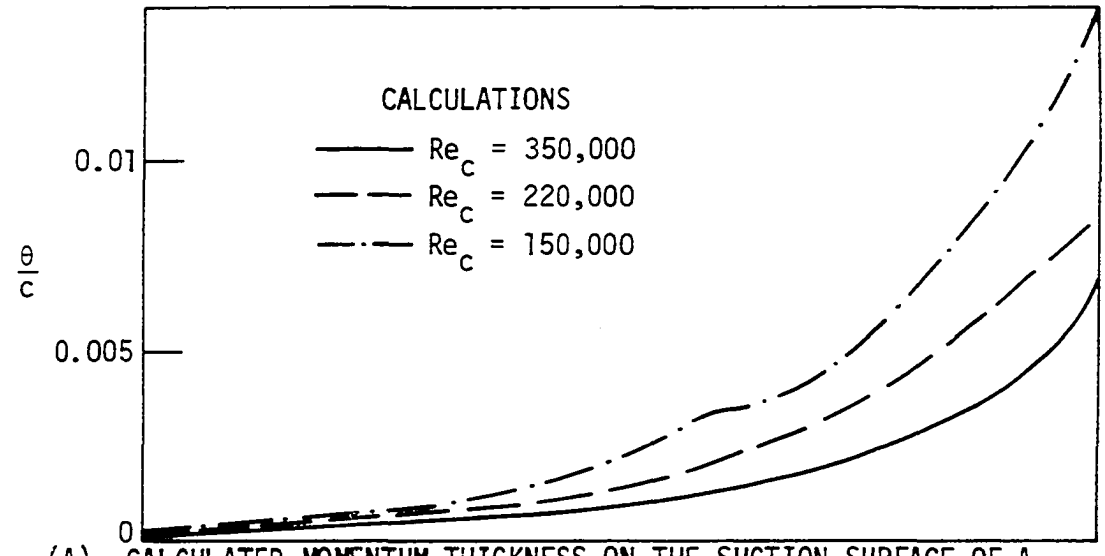

(A) CALCULATED MOMENTUM THICKNESS ON THE SUCTION SURFACE OF A 65-(12)10 CASCADE AT VARIOUS Re_c. $\alpha = 12$, $\sigma = 1.0$, $\gamma = 45.7$, $c = 127$ mm

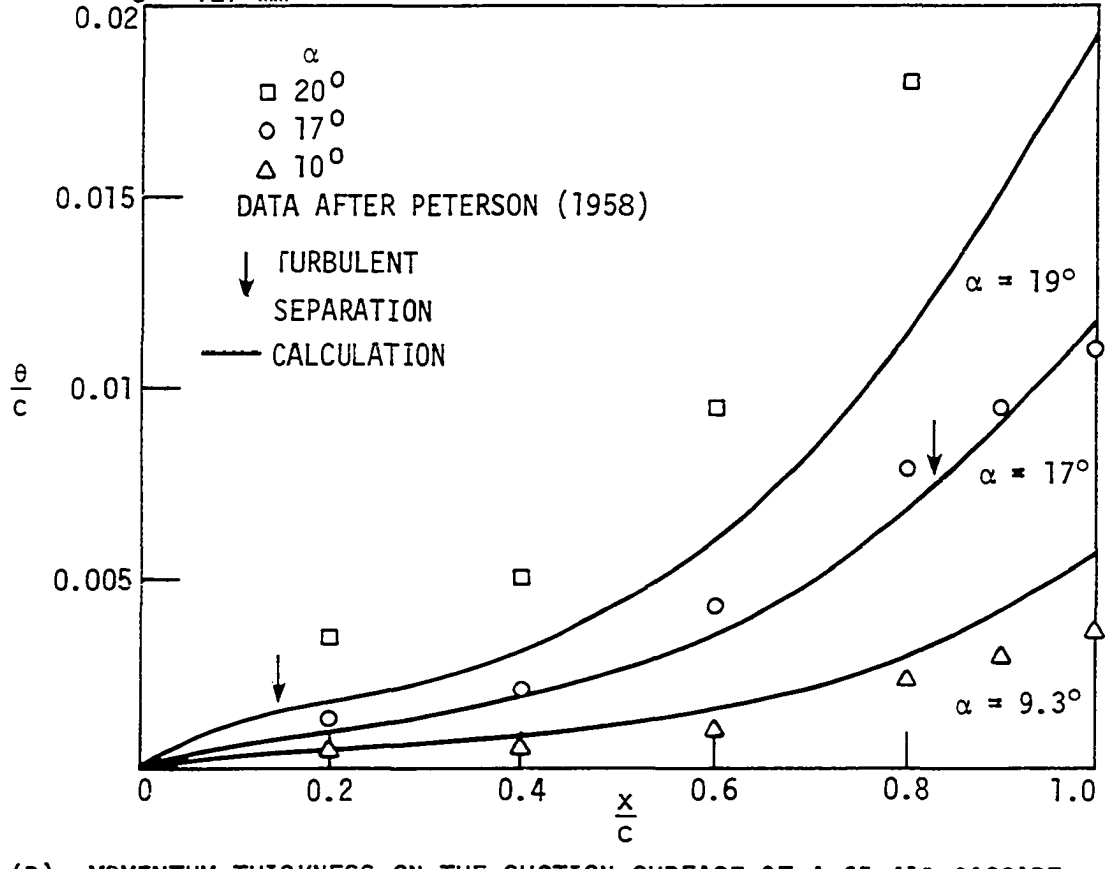

(B) MOMENTUM THICKNESS ON THE SUCTION SURFACE OF A 65-410 CASCADE AT VARIOUS α VALUES, CALCULATED AND EXPERIMENTAL.

Figure 47. Momentum thickness growth.

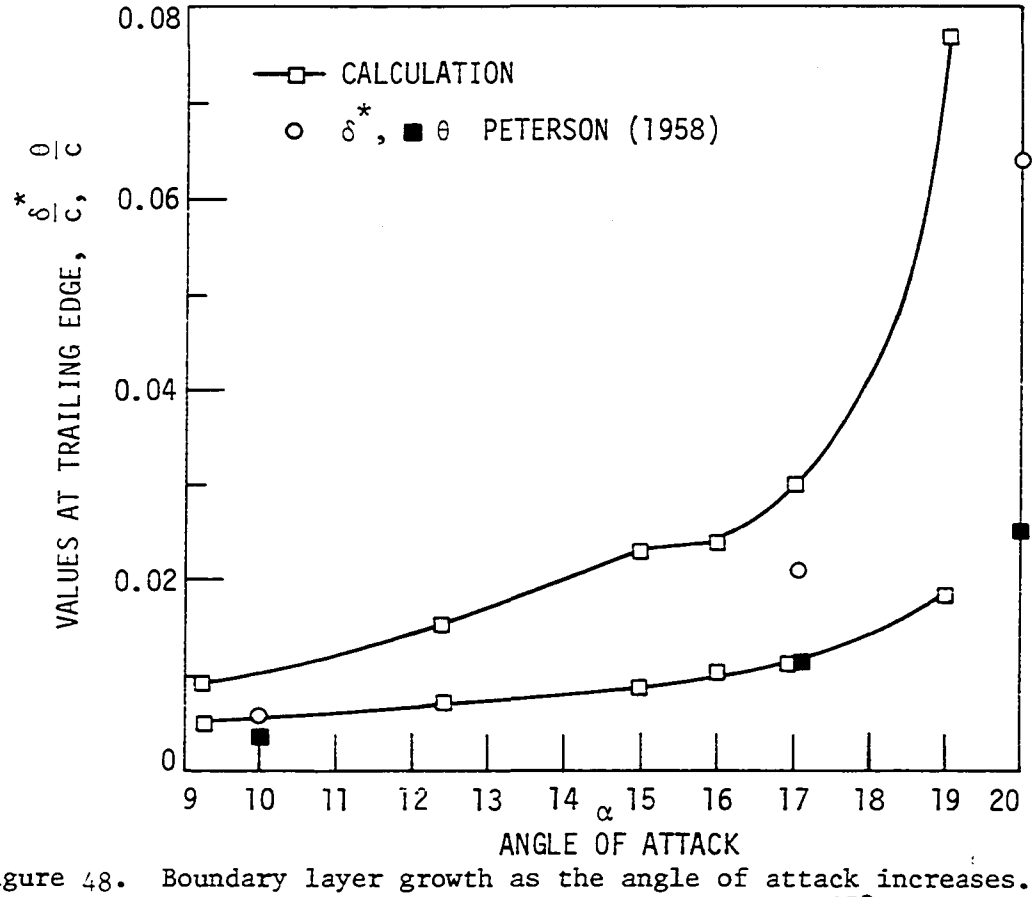

Figure 48. Boundary layer growth as the angle of attack increases. 65-410 blade, M_I = .1, Re_c = 245,000, $\gamma = 45^o$, σ = .78, c = 124 mm.

experimental data and calculations for the 65-410 blade plotted against the angle of attack. This shows that for a small change in incidence at high incidence there is a large change in the boundary layer.

From the data alone it would not be particularly obvious why this sudden growth of the boundary layer takes place. However, the present calculation scheme gives some insight into the cause of the sudden growth. In Figure 47b the difference between the momentum thicknesses at X/c = 0.2 of $\alpha = 9.3°$ and $\alpha = 17°$ is probably caused by the differences in the peak pressure coefficients on the suction surface. At $\alpha = 9.3°$, the maximum C_p is 1.57 while at $\alpha = 17°$ it is 2.9. At $\alpha = 17°$ the boundary layer still undergoes transition at X/c = 0.32 while at $\alpha = 19°$ laminar separation takes place at X/c = 0.03. The laminar separation causes a large increase in the momentum and displacement thicknesses across the separated region. This can be seen by observing the equations used to model the separated region, Equations 14, 15, 16, and 17. Using the ratio, $\overline{U}_{e_r}$, of the reattachment velocities and the separation velocity, $\overline{U}_{e_r} = U_{e_r}/U_{e_{sep}}$ as a measure of the suction surface velocity gradient near the leading edge, Figure 49 shows that as $\overline{U}_{e_r}$ decreases (i.e., the suction surface velocity gradient becomes steeper) θ_r/θ_{sep} grows rapidly.

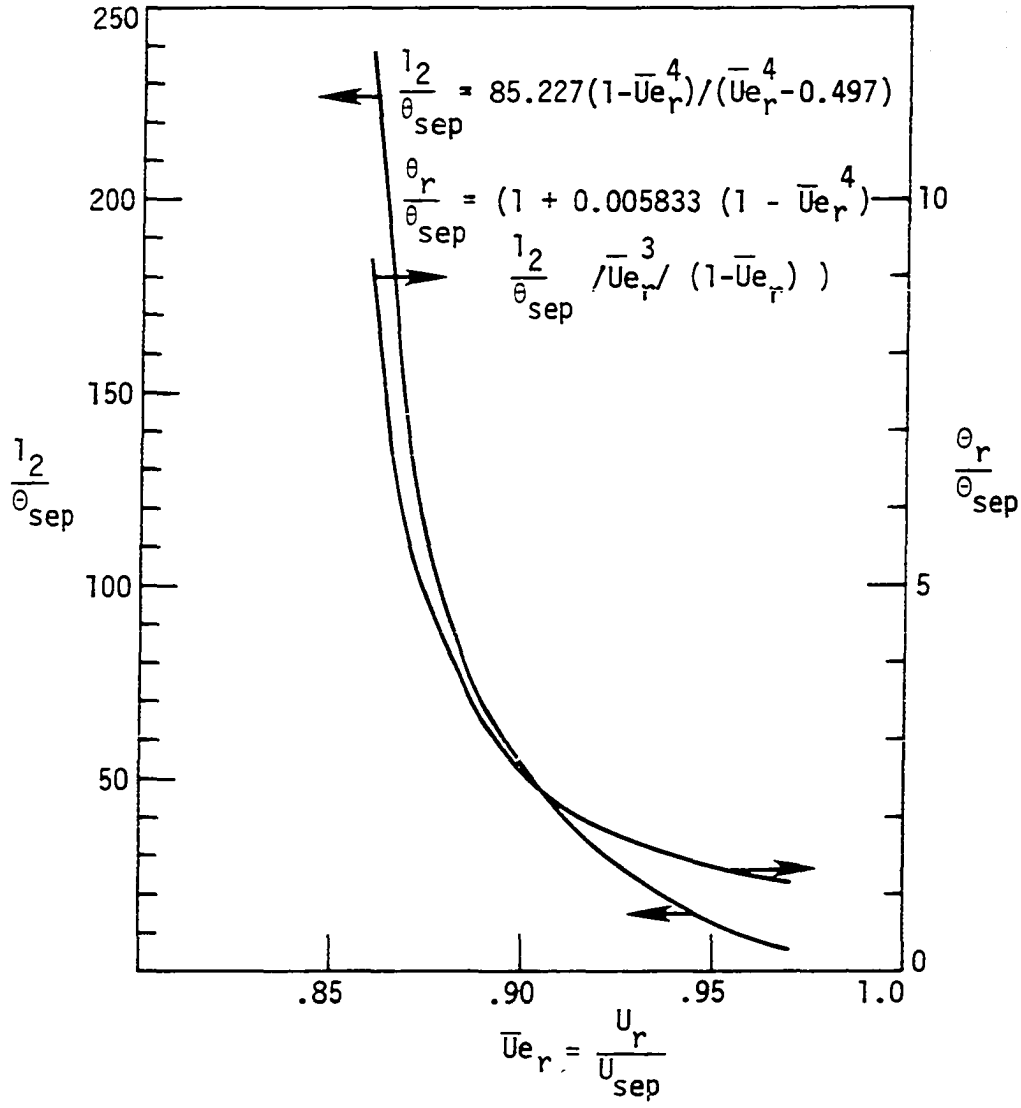

Figure 49. The increase in momentum thickness through a laminar separated region after equations from Roberts (1974).

Effect of the Suction Surface Boundary Layer

In the test cases where the boundary layer displayed the type of behavior as in Figure 47 and 48, the turning, $\Delta\beta$, showed a decrease (Figures 23 and 34). Knowing this and looking at the interaction equations, the beginnings of a relationship between the injected suction surface displacement thickness and the change in turning can be shown. Equations 23, 24, and 25, become Equations 27, 28, 29.

$$\Delta u_s = \frac{\partial U_s}{\partial \beta_{o,I}} \Delta\beta_{o,I} + \frac{\partial U_s}{\partial \delta^*_s} (\Delta\delta^*_{inj,s}) \tag{27}$$

$$\Delta u_p = \frac{\partial U_p}{\partial \beta_{o,I}} \Delta\beta_{o,I} \tag{28}$$

$$U_p + \Delta U_p = U_s + \Delta U_s \tag{29}$$

Let $U_s = U_p$.

Therefore,

$$\Delta U_p = \Delta U_s \tag{30}$$

Combining Equations 27, 28, and 30,

$$\frac{\partial U_p}{\partial \beta_{o,I}} \Delta\beta_{o,I} = \frac{\partial U_s}{\partial \beta_{o,I}} \Delta\beta_{o,I} + \frac{\partial U_s}{\partial \delta^*_s} (\Delta\delta^*_{inj,s}).$$

Solving for $\Delta\beta_{o,I}$ in terms of $\Delta\delta^*_{inj,s}$ and the derivatives, one obtains

$$\Delta\beta_{o,I} = \frac{\dfrac{\partial U_s}{\partial \delta^*_s}}{\dfrac{\partial U_p}{\partial \beta_{o,I}} - \dfrac{\partial U_s}{\partial \beta_{o,I}}} \Delta\delta^*_{inj,s} \quad . \tag{31}$$

From numerous calculations done by the author not mentioned in this work and in agreement with Dodge (1973), $\frac{\partial U_s}{\partial \beta_{o,I}}$ and $\frac{\partial U_p}{\partial \beta_{o,I}}$ are considered nearly constant. $\frac{\partial U_s}{\partial \delta^*_s}$ is also considered a constant though it will decrease as $\delta^*_{inj,s}$ increases. Therefore, the change in the inviscid outlet angle is nearly proportional to the change in suction surface displacement thickness. This is shown to be true in Figure 50. The calculated points, are chosen at intermediate calculations when U_s and U_p were approximately equal, though the boundary layer thicknesses may not yet be converged. The solid lines show the general trend of these points and the dashed lines show the slope in Equation 31, using values of the derivatives from the interacted calculations. For the 65-410 and the 65-(12)10 blades at $\delta^*_{inj,s}/c > 0.05$ there are points which do not correspond to the straight portion of the graph. Part of the decrease in slope might be attributed to the decrease in slope of $\frac{\partial U_s}{\partial \delta^*_s}$ and the rest of the decrease is probably caused by the way the surface pressure is obtained from the interior velocity field using different sets of four points as $\delta^*_{inj,s}$ grows.

The outlet angle, β_0, also increases because of mixing downstream of the trailing edge. Figure 51 shows the change in the outlet angle $\beta_o - \beta_{o,I}$ as a function of $(\delta^*_s - \delta_{te})/s$ where the points are calculated from typical values of δ^* and θ during the solutions for all three blade shapes.

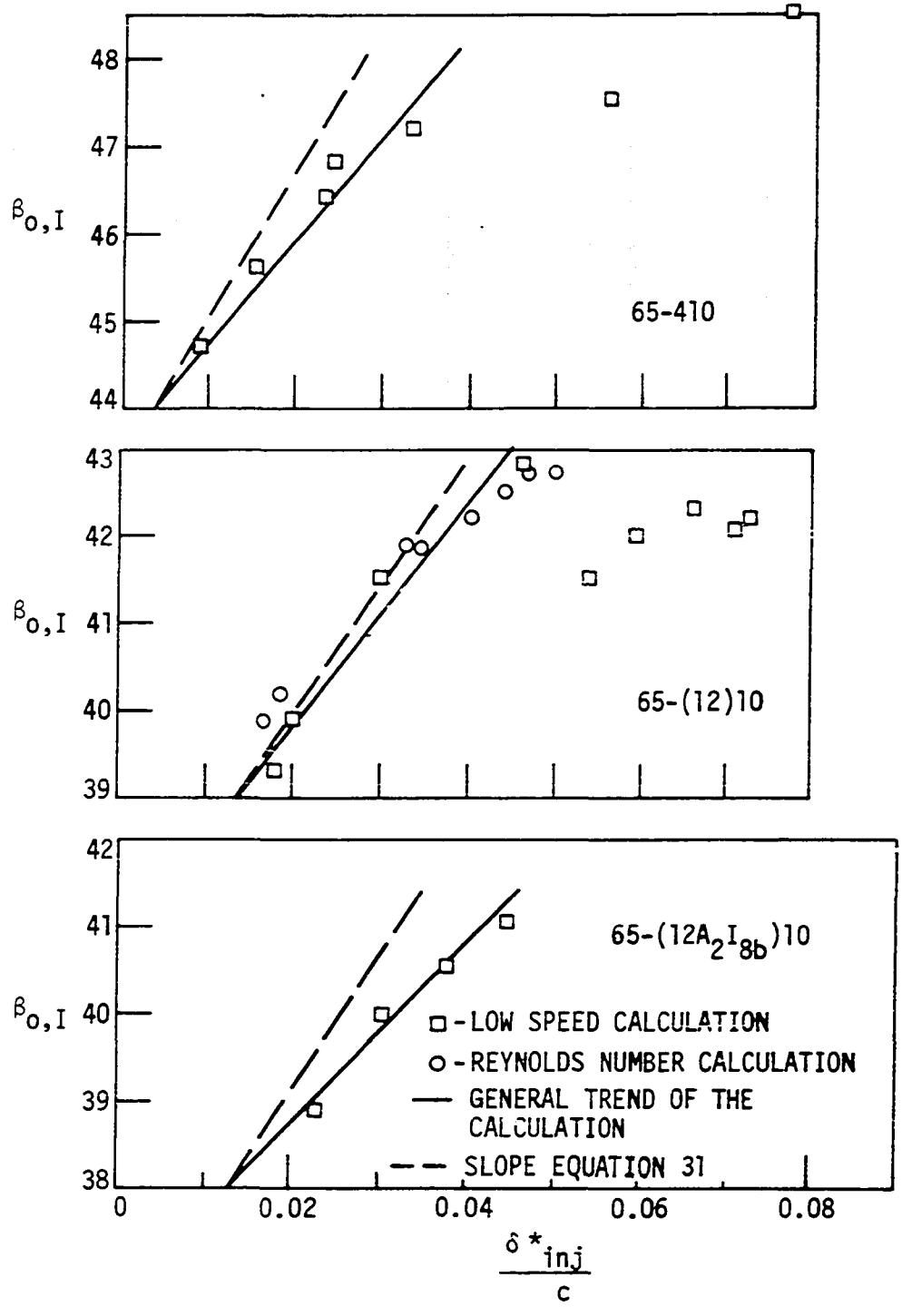

Figure 50. The calculated effect of various values of the injected suction surface boundary layer on the inviscid outlet angle when pressures are equal at the trailing edge.

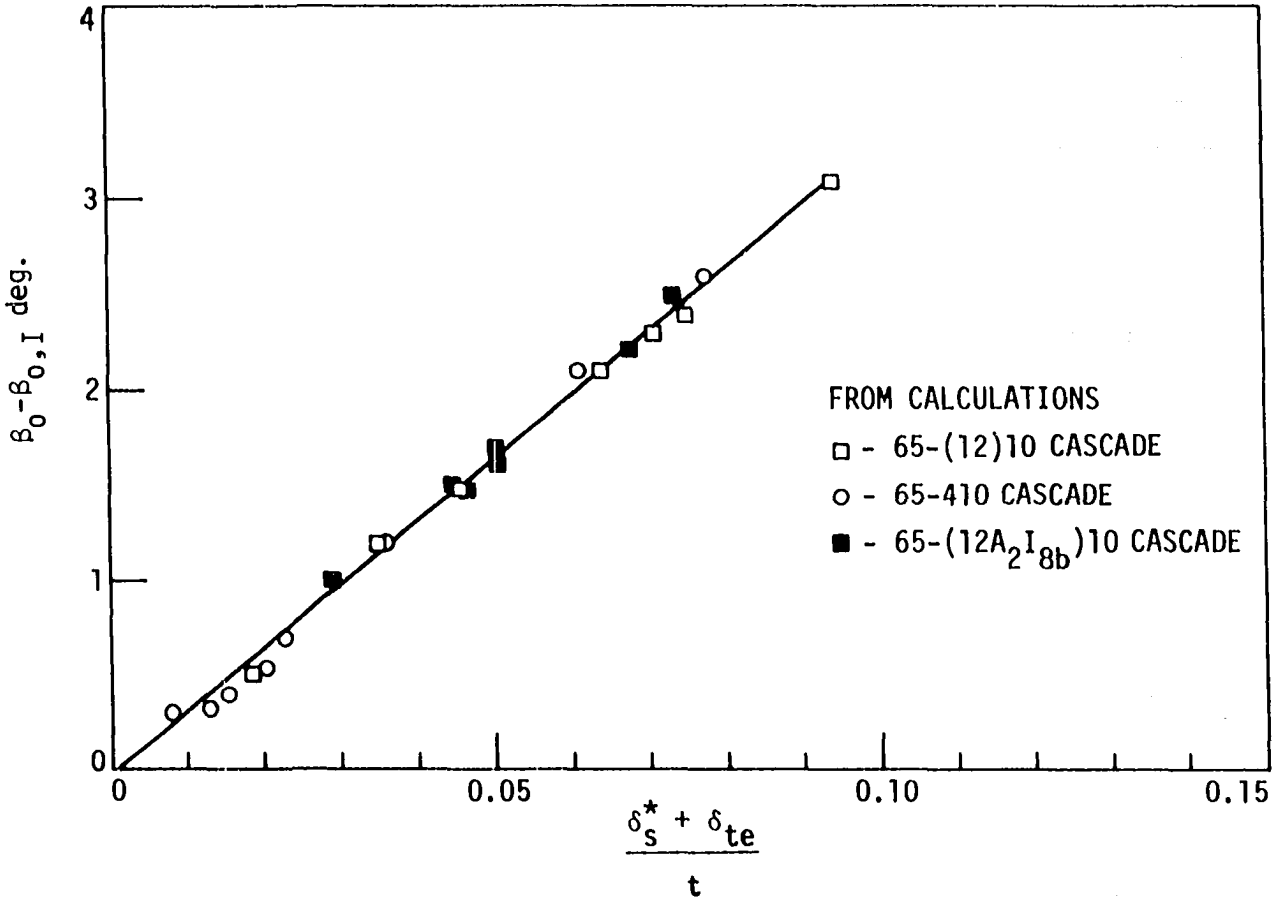

Figure 51. Increase in β_o downstream because of mixing.

Now, knowing to some extent, the way the two previously explained mechanisms increase the outlet angle, it is possible to calculate the outlet angle if the suction surface displacement thickness is known, using the form $\beta_o = m\delta_s^* + \beta_{o,\,intercept}$. In Figure 52 the turning is calculated from the outlet angle determined from the previous equation. The values of δ_s^* used are obtained by estimating H (H = 1.4 if C_w is small to H = 2.0 if C_w is large) and calculating θ from C_w by $\theta = \frac{C_w}{2} \frac{\cos^3\beta_o}{\cos^2\beta_i} c$. The slope m is obtained from the slopes of the graphs on Figures 50 and 51. Then using the value of β_o at the point marked by the arrow in Figure 52, $\beta_{o,intercept}$ is obtained. Then β_o and $\Delta\beta$ can be calculated and compared with the actual data as shown. Though $\Delta\beta$ is underestimated at the highest α's, the results show fairly good agreement.

In light of the evidence that there is some sort of relationship between β_o and δ_s^*, $\Delta\beta_o$ is plotted against $\frac{\theta}{t \cos \beta_o}$ from experimental data for all the three blade shapes used in this work, in Figure 53, where $\frac{\theta}{t \cos \beta}$ has calculated from C_w and $\Delta\beta_o$ is the increase in deviation from the minimum loss point to the higher loss points. To some extent, Figure 53 suggests that there may be a relationship between $\Delta\beta_o$ and δ_s^* similar to the solid line, which initially has a large slope that decreases as δ_s^* grows.

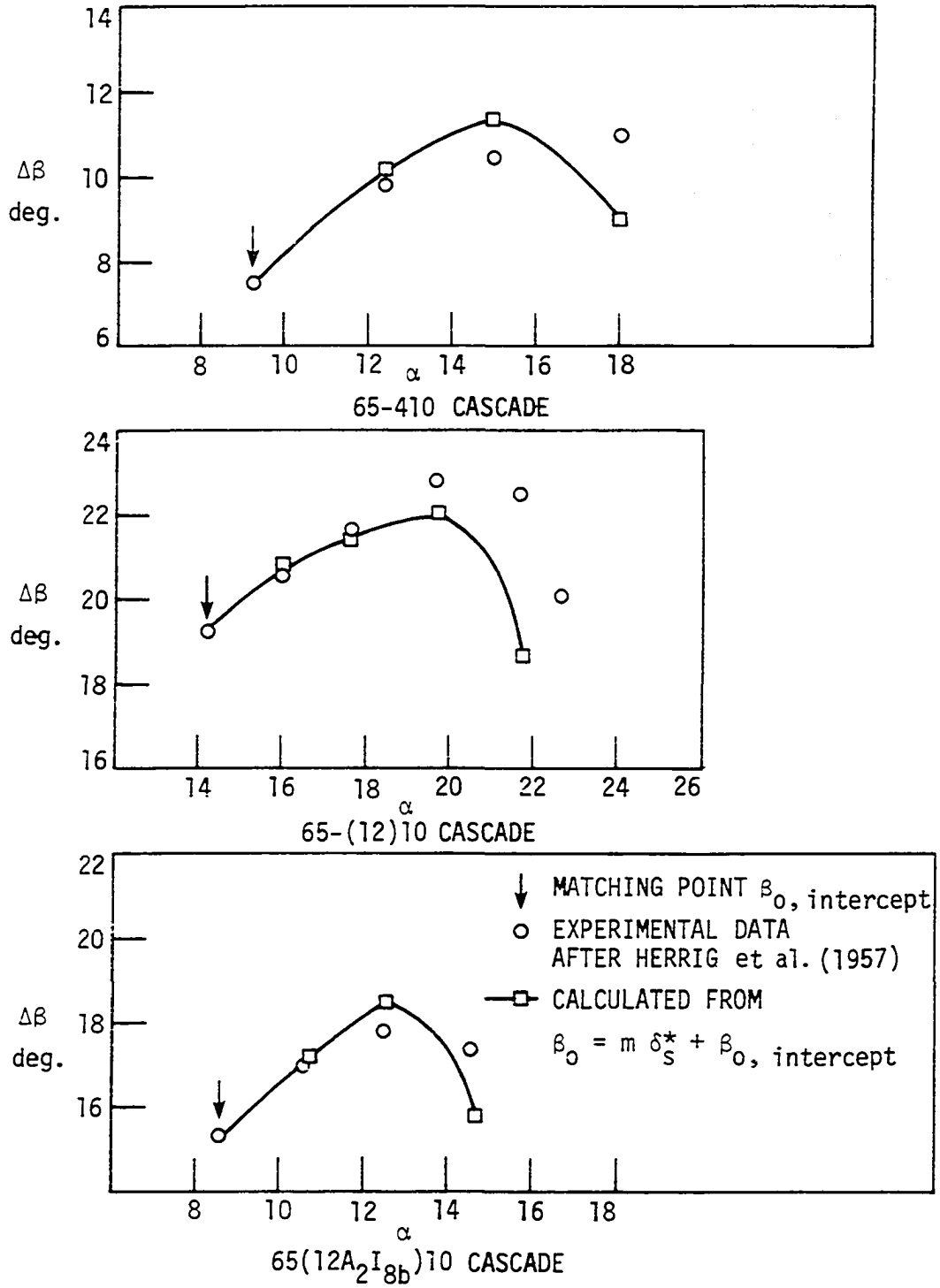

Figure 52. Comparison of $\Delta\beta$ using $\beta_o = m\,\delta_s^* + \beta_{o,\,\text{intercept}}$ and experimental data.

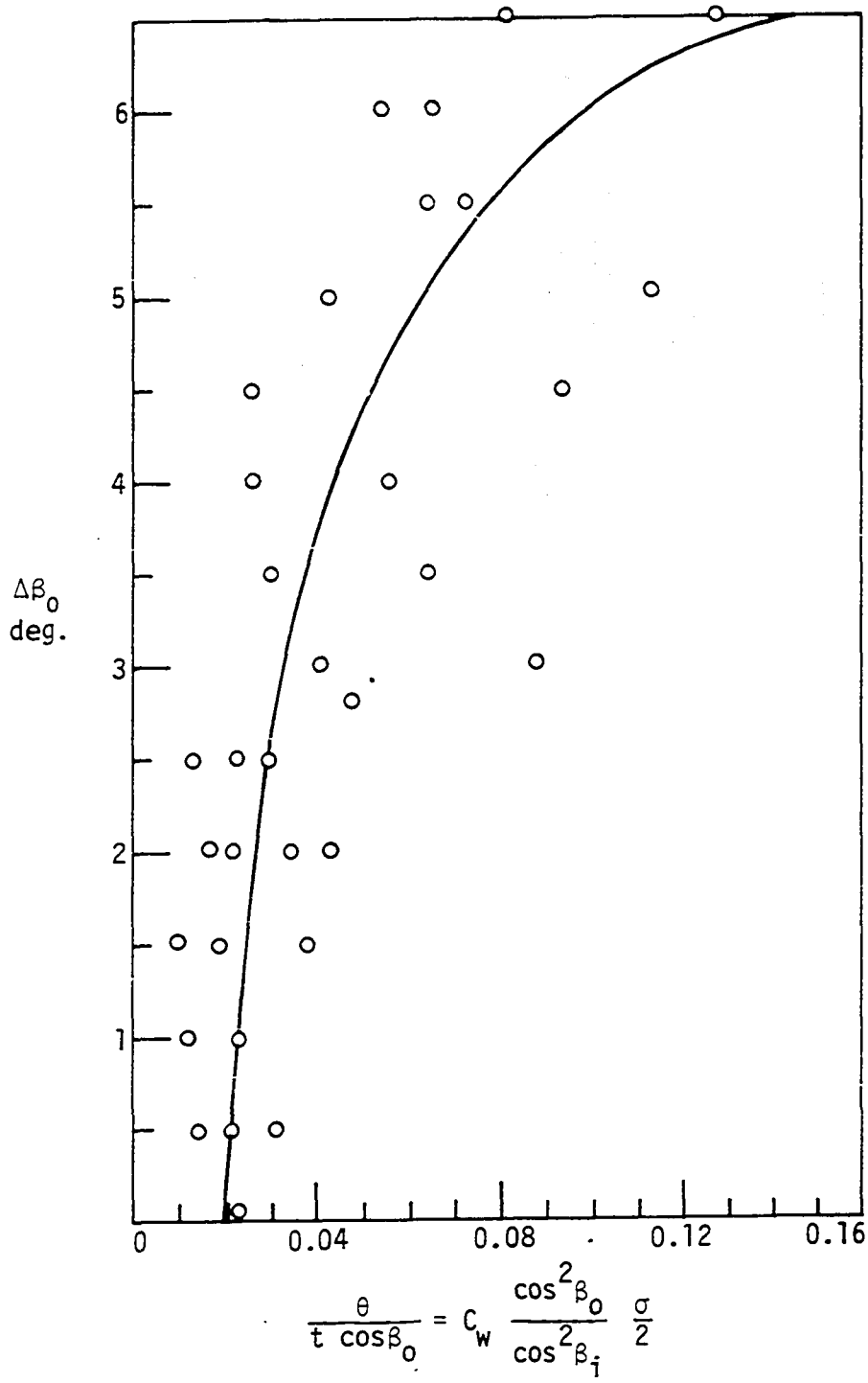

Figure 53. Correlation of experimental data to relate the change in the outlet angle with the momentum thickness. Data from Herrig et al. (1957).

CONCLUSIONS

The results of this work suggest that:

1. To calculate accurate cascade fluid outlet angles an inviscid solution is not adequate in itself. An inviscid calculation must be supplemented by at least an interacting viscous calculation.
2. The viscous calculation must provide for laminar, laminar separated, transitional, turbulent, and turbulent separated flows.
3. To model laminar separation, the leading edge velocity distribution (obtained from the inviscid solution) must be accurately calculated, particularly the magnitude of the peak velocity.
4. The static pressure distribution across the viscous layer in a direction normal to the streamlines is continuous but not necessarily constant. The modeling of the pressure difference across the viscous layer is necessary for the determination of the outlet flow angle.
5. To use an inviscid-viscous method to accurately determine fluid outlet angles, the calculated inviscid flow must match the actual flow outside of the viscous region. In general this requires a pressure jump in the inviscid flow across a line such as a wake centerline.
6. The combined inviscid-viscous interaction system developed here yields results for both turning and total pressure loss characteristics which are quantitatively consistent with the results

of selected experimental test cases. This suggests that the physical basis for the interactive system is correct and should justify further exploration of the use of the method. This exploration should include the acquisition of additional test case experimental data.

SUGGESTIONS FOR FURTHER RESEARCH

As the present work is being finished there is continued work in the area of cascade modeling. However, in view of the research just presented, work on cascade modeling would probably be most profitable if pursued in the following manner. First, measurements of static pressure and velocity (magnitude and direction) are needed in the trailing edge region. Second, measurements of the boundary layer growth along the blade are needed to find the cause of the rapid growth of the boundary layer at high incidence angles. Finally, when there is sufficient data available to help construct workable models of the flow (i.e., a model at the trailing edge to fix the outlet angle and a model of the boundary layer which accurately predicts the rapid increase in thickness at high incidence angles) then an entire cascade model should be attempted. Also, as data is available, effort should be spent investigating the relationship between the fluid turning angle and the size of the suction surface boundary layer displacement thickness.

BIBLIOGRAPHY

Albers, J., and J. Gregg. 1974. Computer program for calculating laminar, transitional, and turbulent boundary layers for a compressible axisymmetric flow. U.S. NACA TN D-7521.

Alpert, S. 1949. Design method for two-dimension channels for compressible flow with application to high solidity cascades. U.S. NACA TN 1931.

Bammert, K. 1965. Berechnung der Potential-and Druckverteilung beliebiger Schaufelgitter von Turbomaschine mit Konformen Abbildungen. Archiv für das Eisenhüttenwesen 36(2):75-86.

Bavitz, P. C. 1975. Analysis method for 2-D transonic viscous flows. U.S. NACA TN D-7718.

Betz, Albert. 1948. Konforme Abbildung. Springer-Verlag, Berlin, Germany, 357 pp.

Bindon, J., and A. Carmichael. 1971. Streamline curvature analysis of compressible and high Mach number cascade flows. Journal of Mechanical Engineering Science 13(5):344-357.

Bradshaw, P. and D. H. Ferriss. 1971. Calculation of boundary-layer development using the turbulent energy equation: compressible flow on adiabatic walls. Journal of Fluid Mechanics 46(1):83-110.

Briggs, W. B. 1952. Effect of Mach number on the flow and application of compressibility corrections in a two-dimensional subsonic-transonic compressor cascade having varied porous-wall suction at the blade tips. U.S. NACA TN 2649.

Briley, W. R. 1974. Numerical method for predicting three-dimensional steady viscous flow in ducts. Journal of Computational Physics 14:18-28.

Brune, G. W., P. E. Rubbert, and T. C. Nark, Jr. 1974. A new approach to inviscid flow/boundary layer matching. AIAA Paper 74-601.

Callaghan, J. G., and T. D. Beatty. 1972. A theoretical method for the analysis and design of multi-element airfoils. Journal of Aircraft 9(12):844-848.

Cantrell, H., and J. Fowler. 1959. The aerodynamic design of two dimensional turbine cascades for incompressible flow with a high speed computer. Journal of Basic Engineering, Transactions of the ASME 81:349-361.

Carter, J. E. and S. F. Wornom. 1975. Forward marching procedure for separated boundary-layer flows. AIAA Journal 13(8):1101-1103.

Cebeci, T., and A. M. O. Smith. 1968. A finite difference solution of the incompressible turbulent boundary-layer equations by an eddy-viscosity concept. Computation of Turbulent Boundary Layers. AFOSR-IFP--Stanford Conference 1:346-356.

Cumpsty, N. A., and M. R. Head. 1967. The calculation of three-dimensional turbulent boundary layers Part I: Flow over the rear of an infinite swept wing. Aeronautical Quarterly 18(1):55-84.

Dodge, P. 1973. The use of a finite difference technique to predict cascade, stator and rotor deviation angles and optimum angles of attack. Journal of Engineering for Power, Transactions of the ASME 95:185-190.

Dunavant, J. C., and J. C. Emery. 1958. Two dimensional cascade investigation at Mach numbers up to 1.0 of NACA 65-series blade sections at conditions typical of compressor tips. U.S. NACA RM L58A02.

Dunavant, J. C., J. C. Emery, H. C. Walch, and W. R. Westphal. 1955. High speed cascade tests of the NACA 65-$(12A_{10})$10 and NACA 65-$(12A_2I_{8b})$10 compressor blade sections. U.S. NACA RM L55I08.

Dvorak, F. A., and F. A. Woodward. 1975. Viscous potential interaction analysis method for multi-element infinite swept wings. Volume I. U.S. NACA CR 2476.

Emery, J. A., and J. C. Dunavant. 1957. Two-dimensional cascade tests of NACA 65-(Cl_0A_{10})10 blade sections at typical compressor hub conditions for speeds up to choking. U.S. NACA RM L57H05.

Erwin, J. R., M. Savage, and J. C. Emery. 1956. Two-dimensional low speed cascade investigation of NACA compressor blade sections having a systematic variation in mean-line loading. U.S. NACA TN 3817.

Felix, R. A., and J. C. Emery. 1957. A comparison of typical national gas turbine establishment and NACA axial-flow compressor blade sections in cascade at low-speed. U.S. NACA TN 3937.

Föttner, L. 1968. A semi-empirical approach of the transonic flow past cascades including shock and viscous effects. AGARD Conference Proceedings 34:11-1--11-18.

Föttner, L. 1972. Analytical approach for the loss and deflections behavior of cascades in transonic flow including axial mass flow variation. AGARDograph 164:121-139.

Frith, D. A. 1973. Inviscid flow through a cascade of thick, cambered airfoils. Journal of Engineering for Power, Transactions of the ASME 95:220-232.

Garabedian, B. R., and D. G. Korn. 1971. Analysis of transonic airfoils. Communications on Pure and Applied Mathematics 24(6):841-851.

Garrick, I. E. 1943. On the plane potential flow past a lattice of arbitrary airfoils. U.S. NACA Report 788.

Geller, W. 1968. Zur Berechnung der Ebenen Reibungsfreien Inkompressiblen Gitterströmung mit einem Modifizierten Martensenverfahren. DLR FB 68-77.

Geller, W. 1972. Incompressible flow through cascades with separation. AGARDograph 164:171-186.

Geller, W. 1976. Theoretische Untersuchung des Einflusses der Lang des Grenzschichtumschlagpunktes auf Umlenkung and Verluste der Schaufelgitterströmung. Zeitschrift für Flugwissenschaften 24(1): 13-16.

Goldstein, S. 1938. Modern developments in fluid dynamics. Volume I. The Clarendon Press, Oxford, England.

Hall, W. S., and B. Thwaites. 1963. On the calculation of cascade flows. Aeronautical Research Council Current Paper 806.

Hansen, E. C. 1976. A study of the methods for analysis of the flow field in cascades. NASA Grant NSG 3033-Blade Surface Boundary Layer and Wake Computation. Iowa State University. Engineering Research Institute. ISU-ERI-Ames-77065; TCRL-6.

Herrig, L. J., J. C. Emery, and J. R. Erwin. 1957. Systematic two-dimensional cascade tests of NACA 65-series compressor blades at low speeds. U.S. NACA TN 3916.

Herring, H. J., and G. L. Mellor. 1972. Computer program for calculating laminar and turbulent boundary layer development in compressible flow. U.S. NACA CR 2068.

Hess, J. L., and A. M. O. Smith. 1966. Calculation of potential flow about arbitrary bodies. Progress in the Aeronautical Sciences 8. Pp 1-138.

Horlock, J. H. 1970. Boundary layer problems in axial turbomachines. Pages 322-371 in Lang S. Dzung, ed. Flow research on blading. Elsevier Publishing Company, New York.

Horton, H. P. 1967. A semi-empirical theory for the growth and bursting of laminar separation bubbles. Aeronautical Research Council Current Paper 1073.

Howell, A. R. 1948. Theory of arbitrary aerofoils in cascades. Philosophical Magazine, Ser. 7, 39:913-927.

Imbach, H. 1964. Calculation of the compressible, frictionless subsonic flow through a plane blade cascade. The Brown Boveri Review 51(12):752-761.

Ispas, I. 1974. Berechnung der kompressible reibungsfrien Unterschallströmung durch Turbomaschinengitter mit Hilfe eines Differenzenverfahrens. Brennstoff-Warme-Kraft 26(10):435-441.

Jacob, K. 1969. Berechnung der abgelösten incompressiblen Strömung um Tragflügel-profile und Bestimmung des maximalen Auftriebs. Zeitschrift für Flugwissenschaften 17(7):221-230.

Jacob, K., and F. W. Riegels. 1963. Berechnung der Druckverteilung endlich dicker Profile onhe and mit Klappen and Vorflügeln. Zeitschrift für Flugwissenschaften 11(9):357-367.

Joukowsky, N. 1910. Uber die Konturen der Fragläches der Drachenflieger. Zeitschrift für Flugtechnik and Motorluftschiffahrt 1:281-284.

Katsanis, T. 1965. Use of arbitrary quasi-orthogonals for calculating flow distribution on a blade-to-blade surface in a turbomachine. U.S. NACA TN D-2809.

Katsanis, T. 1969. FORTRAN program for calculating transonic velocities on a blade-to-blade stream surface of a turbomachine. U.S. NACA TN D-5427.

Katsanis, T. and W. D. McNally. 1969. FORTRAN program for calculating velocities and streamlines on a blade-to-blade-stream surface of a tandem blade turbomachine. U.S. NACA TN D-5044.

Klineberg, J. M., and J. L. Steger. 1972. Flows with strong interaction between the viscous and inviscid regions. Calculation of Separated Flows at Subsonic and Transonic Speeds. Third International Conference on Numerical Methods in Fluid Dynamics, Paris.

Lieblein, S., and W. Roudebush. 1956. Theoretical loss relations for low-speed two-dimensional cascade flow. U.S. NACA TN 3662.

Lighthill, M. J. 1958. On displacement thickness. Journal of Fluid Mechanics 4:383-392.

Mani, R., and A. J. Acosta. 1968. Quasi two-dimensional flows through a cascade. Journal of Engineering for Power, Transactions of the ASME 90:119-128.

Marsh, H. 1968. A digital computer program for the through-flow fluid mechanics in an arbitrary turbomachine using a matrix method. Aeronautical Research Council Reports and Memoranda 3509.

Martensen, E. 1971. The calculation of the pressure distribution on a cascade of thick airfoils by means of Fredholm integral equations of the second kind. U.S. NASA TT F-702. Translated from Die Berechnung der Druckverteilung an Dicken Gitterprofile mit Hilfe von Fredholmschen Intergralgleichung Zweiter Art. Nr. 23. Mitteilungen aus dem Max-Planck-Institut für Strömungsforschung und der Aerodynamischen Versuchsanstalt, Göttingen. 1959.

McNally, W. D. 1970. FORTRAN program for calculating compressible laminar and turbulent boundary layers in arbitrary pressure gradients. U.S. NASA TN D-5681.

Mellor, G. L. 1959. An analysis of axial compressor cascade aerodynamics. Journal of Basic Engineering, Transactions of the ASME 81:362-386.

Miller, M. J. 1973. Some aspects of deviation angle estimation for axial-flow compressors. Ph.D. Thesis. Iowa State University.

Miller, M. J., and G. K. Serovy. 1975. Deviation angle estimation for axial-flow compressors using inviscid flow solutions. Journal of Engineering for Power, Transactions of the ASME 97:163-168.

Milsch, R. 1971. Systematische Untersuchung über den Einfluss der Rauhigkeit von Verdichterschaufeln auf den Gitterwirkunsgrad. Doktor-Ingenieur. Der Technischen Universität, Hannover. 118 pp.

Morgan, H. L. 1975. A computer program for the analysis of multielement airfoils in two-dimensional subsonic, viscous flow. Aerodynamic Analysis Requiring Advanced Computers. U.S. NASA SP-347. Part 2.

Nash, J. F. 1967. A practical calculation method for compressible turbulent boundary layers in two-dimensional and axisymmetric flows. Lockheed Georgia Research Memorandum ER-9428.

Novak, R. A. 1975. Some blade-to-blade solution techniques for turbomachinery. Lecture 31, ASME Turbomachinery Institute course on Fluid Dynamics of Turbomachinery. Iowa State University.

Oellers, H. J. 1971. Incompressible potential flow in a plane cascade stage. NASA TT F-13, 982.

Oliver, A. R. 1976. Viscous behavior near the trailing edge of a lifting aerofoil. The Institution of Engineers, Australia, National Conference Publication No. 76112.

Perl, W. 1947. Calculation of compressible flows past aerodynamic shapes by the use of streamline curvature. U.S. NACA TN 1328.

Peterson, C. R. 1958. Boundary layer on an airfoil in a cascade. Massachusetts Institute of Technology Gas Turbine Laboratory Report 49.

Pletcher, R. H. 1974. Prediction of transpired turbulent boundary layers. Journal of Heat Transfer Transactions of the ASME 96: 89-94.

Pollard, D., and J. H. Horlock. 1962. A theoretical investigation of the effect of change in axial velocity on the potential flow through a cascade of aerofoils. Aeronautical Research Council Current Paper 619.

Pollard, D. and J. Wordsworth. 1962. A comparison of two methods for predicting the potential flow around arbitrary airfoils in cascade. Aeronautical Research Council Current Paper 618.

Preston, J. H., and N. E. Sweeting. 1943. The experimental determination of the boundary layer and wake characteristics of a simple Joukowski aerofoil, with particular reference to the trailing edge region. Aeronautical Research Council Reports and Memoranda No. 1998.

Raj, R. and B. Lakshminarayana. 1973. Characteristics of the wake behind a cascade of airfoils. Journal of Fluid Mechanics 64(4): 707-730.

Reyhner, T. A., and I. Flügge-Lotz. 1968. Interaction of a shock wave with a laminar boundary layer. International Journal of Non-Linear Mechanics 3:173-179.

Roberts, W. B. 1973. A study of the effect of Reynolds number and laminar separation bubbles on the flow through axial compressor cascades. Ph.D. Thesis. U. Libre de Bruxelles, Institut d'Aéronautique, and von Karman Institute for Fluid Dynamics.

Roberts, W. B. 1975. Effect of Reynolds number and laminar separation on axial cascade performance. Journal of Engineering for Power, Transactions of the ASME 97:261-273.

Sanger, N. L. 1973. Two dimensional analytical and experimental performance comparison for a compressor stator section with D-factor of 0.47. U.S. NASA TN D-7425.

Schlichting, H. 1955. Berechnung der reibungslosen inkompressiblen Strömung für ein vorgegebenes ebenes Schaufelgitter. VDI Forschungsheft 447.

Schlichting, H. 1968. Boundary Layer Theory. 6th Edition. McGraw-Hill, New York. 738 pp.

Scholz, N. 1951. On the calculation of the potential flow around airfoils in cascades. Journal of Aeronautical Sciences 18:65-66.

Scholz, N. 1960. Ergänzungen zum Grenzschichtquadraturverfahren von E. Truckenbrodt. Ingenieur-Archiv 29:82-92.

Seyb, N. J. 1965. Determination of cascade performance with particular reference to the prediction of the boundary layer parameters. Aernoautical Research Council Report 27,214.

Shaalan, M., and J. Horlock. 1968. The effect of change in axial velocity on the potential flow in cascades. Aeronautical Research Council Reports and Memoranda 3647.

Smith, D. L., and D. H. Frost. 1970a. Calculation of the flow past turbomachine blades. Proceedings, The Institution of Mechanical Engineers 184(Part 3G-II):72-85.

Smith, D. L., and D. H. Frost. 1970b. Author's replies. Proceedings, The Institution of Mechanical Engineers 184(Part 3G-II):120.

Speidel, L. 1954. Berechnung der Strömungsverluste von ungestaffelten ebenen Schaufelgittern. Dissertation, T. H. Braunschweig, 1953. Ingenieur-Archiv 22:295-322.

Speidel, L. and N. Scholz. 1957. Untersuchungen über die Strömungsverluste in ebenen Schaufelgittern. VDI Forschungsheft 464:5-36.

Spence, D. A. 1954. Prediction of the characteristics of two-dimensional airfoils. Journal of Aeronautical Sciences 21(9): 557-620.

Stanitz, J., and G. Ellis. 1952. Two dimensional flow on general surfaces of revolution in turbomachines. U.S. NACA TN 2654.

Stark, U., and J. Starke. 1974. Theoretische und experimentelle untersuchungen über die quasi-Zweidimensionale inkompressible Strömung durch vorgegebene ebene Verdichtergitter. Forschung im Ingenieurwesen 40(6):172-186.

Steger, J. L., and H. Lomax. 1971. General relaxation methods applied to problems in transonic flow. Lecture Notes in Physics 8:193-197.

Stevens, W. A., S. H. Goradia, and J. A. Braden. 1971. Mathematical model for two-dimensional multi-component airfoils in viscous flow. U.S. NASA CR-1843.

Stewart, W. 1955. Analysis of two-dimensional compressible-flow loss characteristics downstream of turbomachinery blade rows in terms of basic boundary-layer characteristics. U.S. NACA TN 3515.

Theodorsen, T. 1932. Theory of wing sections of arbitrary shape. U.S. NACA Report 411.

Traupel, W. 1945. Die Berechnung der Strömung durch Schaufelgitter. Sulzer Techn. Rundschau 1:25-42.

Truckenbrodt, E. 1952. Ein Quadraturverfahren zur Berechnung der laminaren und turbulenten Reibungsschicht bei ebener und rotationsymmetrischer Strömung. Ingenieur-Archiv 20:211-228.

Van den Braembussche, R. A. 1973. Calculation of compressible subsonic flow in cascades with varying blade height. Journal of Engineering for Power, Transactions of the ASME 95:345-351.

Walz, A. 1966. Strömungs - und Temperaturgrenzschichten. Karlsruhe Braun. 297 pp.

Wattendorf, F. L. 1935. A study of the effects of curvature on fully developed turbulent flow. Proceedings of the Royal Society of London, Series A, 148:565-598.

Weinig, F. 1935. Die Strömung um die Schaufeln von Turbomaschinen. J. A. Barth, Leipzig.

White, F. 1974. Viscous fluid flow. McGraw-Hill Book Company, New York. 725 pp.

Wilkinson, D. H. 1968. A numerical solution of the analysis and design problems for the flow past one or more aerofoils or cascades. Aeronautical Research Council Reports and Memoranda 3545.

Wilkinson, D. H. 1972. Calculation of blade-to-blade flow in a turbomachine by streamline curvature. Aeronautical Research Council Reports and Memoranda 3704.

Wu, C.-H., and C. A. Brown. 1951. Method of analysis for compressible flow past arbitrary turbomachine blades on general surface of revolution. U.S. NACA TN 2407.

ACKNOWLEDGMENTS

I would like to thank Professors Kenneth G. McConnell, Theodore H. Okiishi, Richard H. Pletcher, George K. Serovy, and Donald F. Young who served on my graduate committee and provided me with a good foundation for the present work in the courses they taught.

A special thanks goes to George Serovy for his encouragement, guidance and patience throughout the entire project and to Peter Sockol for his many helpful suggestions during the project.

This work was financially supported by a grant from the National Aeronautics and Space Administration. Appreciation is expressed for this support and the use of the facilities at the Lewis Research Center. Thanks are also extended to those researchers at Lewis who took their time to provide assistance in this work.

Finally, gratitude is expressed to the one without whom this project would not have been, Jesus Christ. Before I met Christ, during the summer of 1973, I was dead by reason of my sin. When I met Him and trusted Him as my Savior, He made me alive having paid for all my sins by His death on the cross. At that point He changed the course of my life from mere existence to fellowship with the Creator of the universe. Jesus Christ is the One Who has empowered me to do this work. He is the Lord of lords and the King of kings.

APPENDIX A: MASS ADDITION BECAUSE OF THE TRAILING EDGE THICKNESS

From the geometry in Figure 54,

$$(\delta_{te})_s = r_s(1 + \sin \beta_{o,I})$$

$$(\delta_{te})_p = r_p(1 - \sin \beta_{o,I}).$$

Knowing $l = \dfrac{U_{ave} \cos \beta_{o,I} \rho b t_{modified}}{w}$,

$$\frac{U_{ave} \rho b}{w} = \frac{1}{t_{modified} \cos \beta_{o,I}} .$$

$t_{modified}$ is the pitch minus the trailing edge thickness blockage in the θ direction, $t_{modified} = t - \dfrac{(\delta_{te})_s}{\cos \beta_{o,I}} - \dfrac{(\delta_{te})_p}{\cos \beta_{o,I}}$. The mass addition on the suction surface is

$$\Delta\psi_s = \frac{\dfrac{(\delta_{te})_s}{\cos \beta_{o,I}}}{\left(t - \dfrac{(\delta_{te})_s}{\cos \beta_{o,I}} - \dfrac{(\delta_{te})_p}{\cos \beta_{o,I}}\right)}$$

The mass addition on the pressure surface is

$$\Delta\psi_p = \frac{\dfrac{(\delta_{te})_p}{\cos \beta_{o,I}}}{\left(t - \dfrac{(\delta_{te})_s}{\cos \beta_{o,I}} - \dfrac{(\delta_{te})_p}{\cos \beta_{o,I}}\right)} .$$

Therefore at the trailing edge on the suction surface

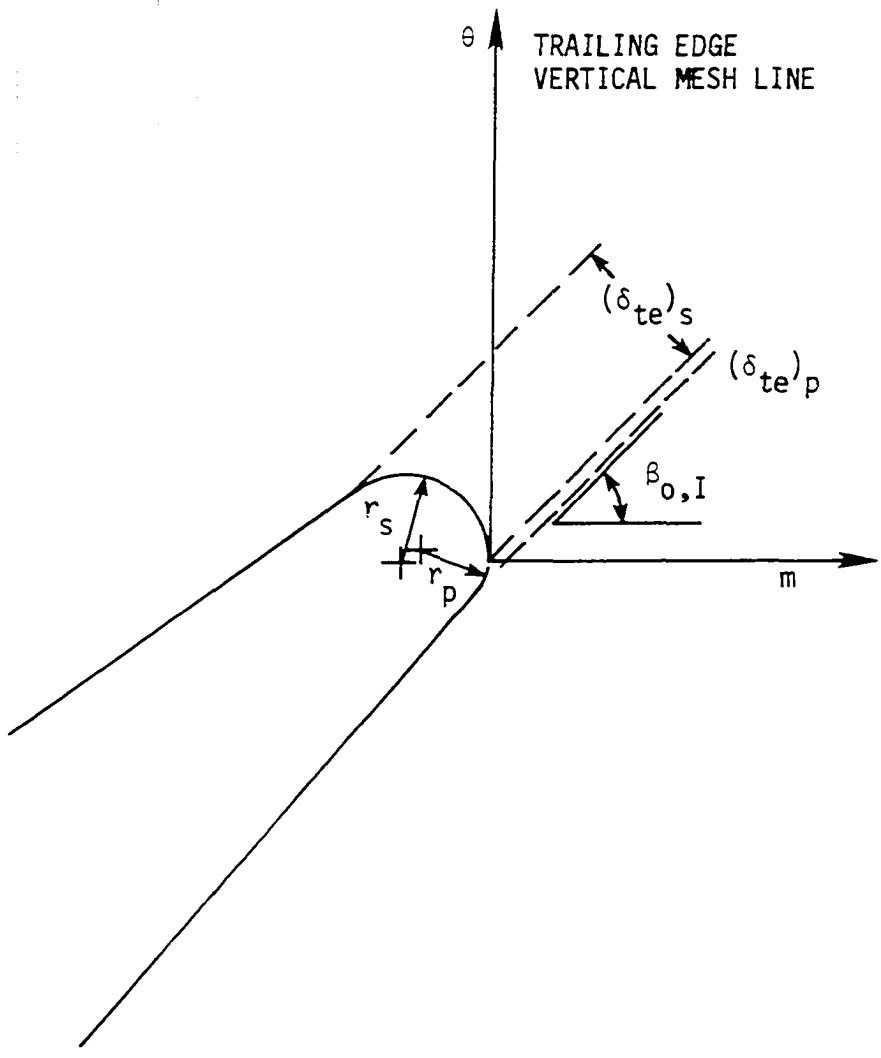

Figure 54. Geometry of the trailing edge radii.

$$\psi = 0 - \frac{u\rho b\delta^*}{w})_{te} - \Delta\psi_s$$

and on the pressure surface

$\psi = 1 + \frac{u\rho b\delta^*}{w})_{te} + \Delta\psi_p$, where $\frac{u\rho b\delta^*}{w}$ is the change in boundary conditions because of the injected boundary layer displacement thickness.

APPENDIX B: CALCULATION BEYOND THE FAILURE OF THE BOUNDARY LAYER METHOD

In a separated region, after the boundary layer calculation procedure has failed at s_{fail}, the momentum and displacement thicknesses are calculated as follows.

The Von Karman integral equation in a separated region, $\tau_w = 0$, is $U^2 \frac{d\theta}{ds} + (2+H)\theta U \frac{dU}{ds} = 0$, which also is

$$\frac{d\theta}{ds} = - \frac{(2+H)\theta}{U} \frac{dU}{ds} .$$

Then using finite differences,

$$\frac{\theta_2-\theta_1}{s_2-s_1} = - \left(2 + \frac{H_2+H_1}{2}\right) \frac{2}{U_2+U_1} \frac{\theta_2+\theta_1}{2} \frac{U_2-U_1}{s_2-s_1}$$

$$\theta_2-\theta_1 = -\left[\left(2 + \frac{H_2+H_1}{2}\right) \frac{U_2-U_1}{U_2+U_1} (\theta_2+\theta_1)\right].$$

Let

$$\left(2 + \frac{H_2+H_1}{2}\right)\left(\frac{U_2-U_1}{U_2+U_1}\right) = B \quad .$$

$$\theta_2-\theta_1 = -B(\theta_2+\theta_1)$$

$$\theta_2(1+B) = \theta_1(1-B)$$

$$\theta_2 = \theta_1\left(\frac{1-B}{1+B}\right)$$

H is estimated by setting $H_{te} = H_{fail} + 1$ and linearly interpolating at s between s_{fail} an s_{te}. Then knowing H, $\theta_2 = \theta_1\left(\frac{1-B}{1+B}\right)$, where

$B = (2 + \frac{H_2+H_1}{2})(\frac{U_2-U_1}{U_2+U_1})$, is integrated at the s steps beginning from the last boundary layer calculation station to the trailing edge. The displacement thickness is obtained from $\delta^* = H_2\theta_2$.

APPENDIX C: CALCULATION OF VISCOUS SURFACE VELOCITIES

Assume, that for the purposes which follow, a velocity profile of the following type is adequate,

$$\frac{u}{U_e} = \left(\frac{y}{\delta}\right)^n.$$

Then

$$\delta^* = \int_0^\delta \left(1 - \frac{u}{U_e}\right) dy$$

$$\delta^* = \delta \int_0^1 \left(1 - \left(\frac{y}{\delta}\right)^n\right) d\left(\frac{y}{\delta}\right)$$

$$\delta^* = \delta\left[1 - \frac{1}{n+1}\right] = \delta\left(\frac{n}{n+1}\right),$$

$$\theta = \int_0^\delta \frac{u}{U_e}\left(1 - \frac{u}{U_e}\right) dy$$

$$\theta = \delta \int_0^1 \left(\left(\frac{y}{\delta}\right)^n - \left(\frac{y}{\delta}\right)^{2n}\right) d\left(\frac{y}{\delta}\right)$$

$$\theta = \delta\left[\frac{1}{n+1} - \frac{1}{2n+1}\right] = \frac{n}{(n+1)(2n+1)},$$

$$H = \frac{\delta^*}{\theta} = 2n+1 \text{ and } \delta = \delta^*\left(\frac{H+1}{H-1}\right).$$

The velocity at point B in Figure 17 is extrapolated from the flow solution points according to Figure 55. First, linear interpolations are made between the value of the velocity at points 2 and 3 to obtain 6 and 1 and 4 to obtain 5. Then the values at 5 and 6 are linearly extrapolated to B and the edge velocity is found.

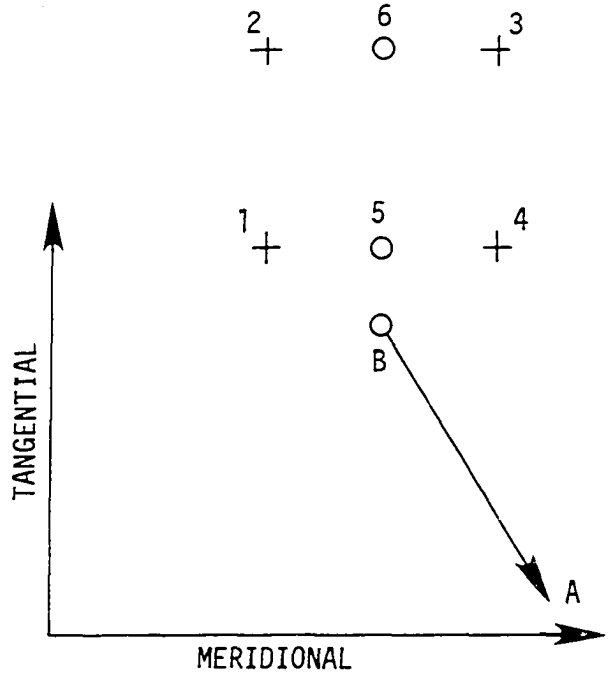

Figure 55. The mesh points used to obtain the pressures at point B and point A. Also see Figure 17.

The curvature of the streamline at B is calculated as follows knowing that

$$\rho u^2 \kappa = \frac{\partial p}{\partial \eta} .$$

For compressible flow

$$\rho = \rho^o \left(1 - \frac{U_e^2}{2c_p T^o}\right)^{\frac{1}{k-1}}$$

$$p = p^o \left(1 - \frac{U_e^2}{2c_p T^o}\right)^{\frac{k}{k-1}}$$

$$R = c_p (k-1)/k.$$

Therefore $\kappa = \frac{1}{\rho U_e^2} \frac{\partial p}{\partial n}$ becomes

$$\kappa = \frac{1}{\rho U_e^2}\left[p^o \left(\frac{k}{k-1}\right)\left(1 - \frac{U_e^2}{2c_p T^o}\right)^{\frac{1}{k-1}}\left(- \frac{U_e}{c_p T^o} \frac{\partial U_e}{\partial \eta}\right)\right]$$

$$\kappa = - \frac{p^o U_e}{T^o \rho U_e^2} \frac{k}{c_p (k-1)} \left(1 - \frac{U_e^2}{2c_p T^o}\right)^{\frac{1}{k-1}} \frac{\partial U_e}{\partial \eta}$$

$$\kappa = - \frac{p^o}{T^o R \rho^o} \frac{1}{U_e} \frac{\partial U_e}{\partial \eta}$$

$$\kappa = - \frac{1}{U_e} \frac{\partial U_e}{\partial \eta} . \qquad (32)$$

The pressure across the viscous layer is calculated from

$\kappa \rho u^2 = \frac{\partial p}{\partial \eta}$ as follows,

$$\int_{p_s}^{p_e} dp = \int_0^{\delta} \kappa \rho u^2 dy$$

$$p_e - p_s = \kappa \rho U_e^2 \int_0^{\delta} \left(\frac{y}{\delta}\right)^{2n} dy$$

$$p_e - p_s = \frac{\kappa \rho U_e^2 \delta}{2n+1} = \frac{\kappa \rho U_e^2 \delta}{H}$$

$$\frac{p_s}{p^o} = \frac{p_e}{p^o} - \frac{\kappa \rho U_e^2 \delta}{p^o H}$$

Substituting

$$\left(1 - \frac{U_s^2}{2c_p T^o}\right)^{\frac{k}{k-1}} = \left(1 - \frac{U_e^2}{2c_p T^o}\right)^{\frac{k}{k-1}} - \frac{\kappa \rho U_e^2 \delta}{H p^o}$$

$$1 - \frac{U_s^2}{2c_p T^o} = \left(\left(1 - \frac{U_e^2}{2c_p T^o}\right)^{\frac{k}{k-1}} - \frac{\kappa \rho U_e^2 \delta}{H p^o}\right)^{\frac{k-1}{k}} = B$$

$$\frac{U_s^2}{2c_p T^o} = 1 - B$$

$$U_s = \sqrt{2c_p T^o (1-B)}$$

$$U_s = \sqrt{2c_p T^o \left(1 - \left(\left(1 - \frac{U_e^2}{2c_p T^o}\right)^{\frac{k}{k-1}} - \frac{\kappa \rho U_e^2 \delta}{H p^o}\right)^{\frac{k-1}{k}}\right)}. \qquad (33)$$

Then the value of κ is obtained from Equation 32 using the average derivatives in the meridional and tangential directions from the value at the four mesh points in Figure 55 and U_s, the viscous surface velocity, which corresponds to the viscous surface pressure can be calculated from Equation 33.

APPENDIX D: CALCULATION OF THE WAKE FLOW

Spence (1954) gives $\frac{U_e-U_c}{U_e} = \frac{0.1265}{(.025 + \frac{s}{c})^{1/2}}$ for airfoils, but the data of Raj and Lakshminarayana (1973) suggest the correlation $\frac{U_e-U_c}{U_e} = \frac{1.03}{(1.46 + \frac{s}{\theta_{te}})^{1/2}}$. If the velocity distribution through the wake is given by a cosine curve then $H = 1/(1-.75(\frac{U_e-U_c}{U_e}))$. Therefore

$$H_s = 1/(1-.7725/\sqrt{1.46 + s/\theta_{te}})$$

and 1.46 can be replaced by a constant d, which is evaluated when $H_s = H_{te}$ and $s = 0$, $d = (.7725*H_{te}/(H_{te}-1))^2$.

Figure 56 shows a control volume beginning at the trailing edge plane and extending downstream. Conservation of mass within that control volume, assuming the upper and lower boundaries are period gives,

$$(t-\delta^*_{te}/\cos\beta_o)U_{te}\cos\beta_o = (t-\delta^*_{ds}/\cos\beta_o)U_{ds}\cos\beta_o.$$

Differentiating with respect to s it becomes,

$$0 = -\frac{d\delta^*}{ds}\frac{U_{ds}\cos\beta_o}{\cos\beta_o} + (t-\delta^*/\cos\beta_o)\frac{dU_{ds}}{ds}\cos\beta_o$$

and

$$\frac{d\delta^*_{ds}}{ds}\frac{1}{(t\cos\beta_o-\delta^*_{ds})} = \frac{dU_{ds}}{ds}\frac{1}{U_{ds}}.$$

In the wake $\tau_w = 0$ and the Von Karman integral equation becomes

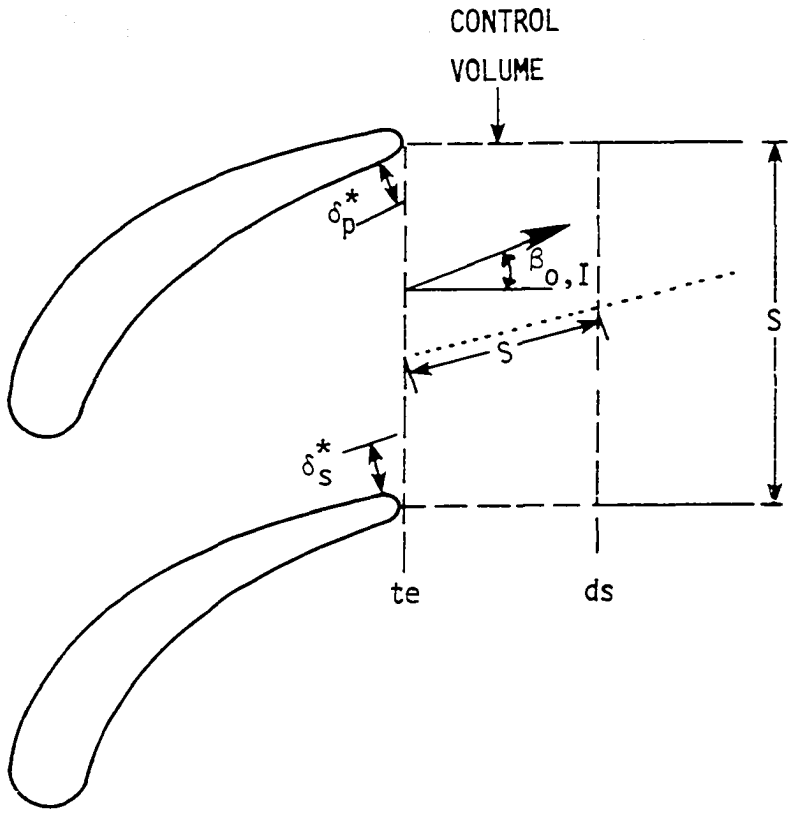

Figure 56. Control volume for the wake calculations

$$\frac{d\theta}{ds} = -\frac{(2+H)\theta}{U}\frac{dU}{ds}$$

substituting $\frac{1}{U_{ds}}\frac{dU_{ds}}{ds}$ for $\frac{1}{U}\frac{dU}{ds}$ and recognizing that all values of θ, δ^*, and H are at the downstream plane.

$$\frac{d\theta}{ds} = \frac{-(2+H)\theta}{(t\cos\beta_o-\delta^*)}\frac{d\delta^*}{ds}$$

$$\frac{d\theta}{ds} = \frac{-(2+H)\theta}{(t\cos\beta_o-\delta^*)}\left(H\frac{d\theta}{ds} + \theta\frac{dH}{ds}\right)$$

Let

$$B_1 = \frac{(2+H)}{(t\cos\beta_o-\delta^*)} \quad .$$

$$\frac{d\theta}{ds} = -B_1\left(H\frac{d\theta}{ds} + \theta\frac{dH}{ds}\right)$$

$$\frac{d\theta}{ds}(1+B_1H) = -B_1\theta\frac{dH}{ds}$$

$$\frac{d\theta}{ds} = \frac{-B_1\theta}{(1+B_1H)}\frac{dH}{ds}$$

$$\frac{d\theta}{ds} = \frac{-\theta}{(1/B_1+H)}\frac{dH}{ds}$$

$$\frac{d\theta}{ds} = \frac{-\theta}{(H+(t\cos\beta_o-\delta^*)/((2+H)\theta))}\frac{dH}{ds}$$

Using finite differences,

$$\frac{\theta_2-\theta_1}{s_2-s_1} = -\frac{\theta_1+\theta_2}{2}\left(\frac{H_2-H_1}{\frac{t\cos\beta_o}{(2+H_{ave})\theta_1}-\frac{H_{ave}}{(2+H_{ave})}+H_{ave}}\right)\frac{1}{s_2-s_1}$$

if

$$B_2 = \frac{H_2-H_1}{\frac{t\cos\beta_o}{(2+H_{ave})\theta_1}-\frac{H_{ave}}{(2+H_{ave})}+H_{ave}}$$

$$\theta_2-\theta_1 = -\frac{\theta_1+\theta_1}{2}(B_2)$$

$$\theta_2(1+B_2/2) = \theta_1(1-B_2/2)$$

$$\theta_2 = \theta_1(1-B_2/2)/(1+B_2/2).$$

Therefore, knowing H_{te},

$$d = (.7725*H_{te}/(H_{te}-1))^2$$

$$H_s = 1/(1-.7725/\sqrt{d+s/\theta_{te}})$$

$$\theta_2 = \theta_1(1-B_2/2)/(1+B_2/2)$$

where

$$B_2 = \frac{H_2-H_1}{\frac{t\cos\beta_o}{(2+H_{ave})\theta_1}-\frac{H_{ave}}{(2+H_{ave})}+H_{ave}}$$

$$H_{ave} = \frac{H_2+H_1}{2}.$$